MONOLITHICALLY INTEGRATED IN-TEXTILE PATCH FOR WIRELESS EPIDERMAL BIOSENSING

XIAOHAO MA

PhD

The Hong Kong Polytechnic University

2026

The Hong Kong Polytechnic University

Department of Applied Biology and Chemical Technology

Monolithically Integrated In-textile Patch for Wireless Epidermal Biosensing

Xiaohao Ma

A thesis submitted in partial fulfilment of the requirements for the degree of Doctor of Philosophy

June 2025

CERTIFICATE OF ORIGINALITY

I hereby declare that this thesis is my work and that, to the best of my knowledge and belief, it reproduces no material previously published or written, nor material that has been accepted for the award of any other degree or diploma, except where due acknowledgement has been made in the text.

_____(Signed)

Xiaohao Ma (Name of Student)

ABSTRACT

Recent advancements in wearable bioelectronics underscore the demand for multifunctional, breathable systems capable of continuous and non-invasive health monitoring. It is highly challenging to develop epidermal biosensing devices with desirable permeability, biocompatibility, and the ability to track both physiological and pathogenic markers simultaneously. This thesis presents several in-textile systems for wireless and real-time biosensing, combining sweat analysis and wound microbial detection into a permeable bioelectronic platform. By utilizing textile-compatible fabrication processes, the biosensing systems can be seamlessly integrated into textiles, providing the attributes of wearing comfort, durability, and conformability to skin deformations during daily activities.

First, a novel photolithography approach designed explicitly for textiles enables uniform and precise metal patterning directly within porous fabric architectures. This method achieves sub-100 μm resolution on yarns, circumventing challenges posed by textile pore dimensions and capillary-driven diffusion within yarn structures. The resulting metal patterns exhibit exceptional mechanical resilience (withstanding 10,000 bending cycles) and laundering durability (20 washes) with minimal change in conductivity. Furthermore, this technique facilitates controllable metal permeation throughout the textile scaffold, significantly enhancing performance and enabling the dual-sided integration of miniaturized electronic devices, while maintaining essential fabric permeability and stability.

Second, a fully integrated fabric wristband incorporating multifunctional modules demonstrates wireless sweat biosensing capabilities. Utilizing precisely patterned conductive elements within the textile structure, coupled with robust interconnection encapsulation, achieves electrical performance, mechanical durability, and liquid resistance comparable to conventional flexible electronics. Critically, the preserved porous nature of the fabric substrate provides exceptional wearing comfort, evidenced by air permeability (79 mm s^{-1}) and moisture vapor transmission rate (270 g m^{-2} day^{-1}) significantly exceeding those of standard medical adhesives. This integrated platform

successfully monitored sweat potassium levels (0.3-40 mM range) with sustained stability, highlighting its suitability for fitness tracking and point-of-care diagnostics. Expanding on this, a multiplexed textile-based sensing system was realized, incorporating signal-conditioned wireless data transmission (Bluetooth Low Energy) for simultaneous detection of pH, sodium (Na^+), potassium (K^+), glucose, and lactate. On-body validation during physical activity showed excellent concordance ($R^2 > 0.99$) with standard reference measurements for potassium. This approach overcomes key hurdles in device-skin interface stability and user comfort, offering a scalable manufacturing route for non-invasive health monitoring platforms.

Finally, a wound monitoring patch was constructed using aptamer sensor arrays integrated onto a breathable textile substrate. This platform facilitates the continuous, multiplexed detection of key wound exudate biomarkers, including pH, the bacterial infection indicator TNF-α, the fungal marker β-1,3-glucan, and the inflammation-associated cytokine IL-6. This fabrication method ensures high-resolution patterning while maintaining essential textile properties: moisture vapor transmission exceeding 290 g m^{-2} day^{-1} and mechanical flexibility. Microbial identification leverages TNF-α for bacterial presence and β-1,3-glucan for fungal detection. Validation yielded a relative standard deviation (RSD) of 21% for mouse TNF-α quantification, demonstrating the viability of this integrated textile-based sensing platform for non-clinical wound management applications.

In conclusion, this thesis first demonstrated a popular and promising in-textile photolithography method for fabricating metal patterning (Cu, Ni and Ag) on fabric structures. Then it introduced an in-textile wristband that offers exceptional flexibility, permeability, biocompatibility, and waterproof properties. Subsequently, a multiplexed system involving five sensors (pH, K^+, Na^+, glucose, and lactate) was developed to produce complex signal processing and transmission with high mechanical stability and superior conductivity. Finally, a monolithic wound patch was proposed to identify microbial infections, such as bacteria and fungi, showcasing its potential for daily wound monitoring and early warning. It is envisioned that this thesis will provide practical and

universal solutions for the development of monolithically integrated in-textile bioelectronics.

LIST OF PUBLICATIONS

Published papers:

1. Xiaohao Ma, Pengwei Wang, Liting Huang, Ruochen Ding, Kemeng Zhou, Yuqing Shi, Fan Chen, Qiuna Zhuang, Qiyao Huang, Yuanjing Lin* and Zijian Zheng*, A Monolithically integrated in-textile wristband for wireless epidermal biosensing, Science Advances, 2023, 9, eadj2763 (published)

2. Pengwei Wang, Xiaohao Ma, Zhiqiang Lin, Fan Chen, Zijian Chen, Hong Hu, Hailong Xu, Xinyi Zhang, Yuqing Shi, Qiyao Huang*, Yuanjing Lin*and Zijian Zheng*, Well-defined in-textile photolithography towards permeable textile electronics, Nature Communications, 2024, 15, 887 (published)

3. Mingli Huang, Xiaohao Ma, Zongze Wu#, Jirong Li, Yuqing Shi, Teng Yang, Jiarun Xu, Shuhan Wang, Kongpeng Lv* and Yuanjing Lin*, Ammonium sensing patch with ultrawide linear range and eliminated interference for universal body fluids analysis, Nano-Micro Lett, 2025, 17, 92 (published)

4. Yuqing Shi, Kemeng Zhou, Xiaohao Ma, Liting Huang, Xinmeng Hu, Pengwei Wang, Yaokang Zhang, Fan Chen, Mingli Huang, Jianzhen Wu, Xin He, Qiyao Huang, Zijian Zheng*, Yuanjing Lin*, Washable textile biosensors enabled by nanostructured oxides with fast ion diffusion, Device, 2024, 2, 100503 (published)

5. Kemeng Zhou, Ruochen Ding, Wenhao Ye, Jitao Huang, Zihan Zhou, Liting Huang, Xiaohao Ma, Zhiyong Fan, Yuanjing Lin*, A fully printable and integrated system with long-term stability for versatile and multimodal perspiration tracking, 2025, 25, 35 (published)

ACKNOWLEDGEMENTS

Foremost, I would like to express my deepest gratitude to my supervisors, Prof. Zijian Zheng and Yuanjing Lin, for the invaluable opportunity to pursue my Ph.D. within their research groups. Their profound expertise and rigorous approach to scientific inquiry have been immensely inspirational and formative. Their patient mentorship and consistent encouragement were fundamental to my progress.

I am profoundly grateful to all members of Prof. Zheng's and Prof. Lin's research groups. Their collective efforts created an outstanding laboratory environment and fostered a dynamic, collaborative culture. I extend particular thanks to Prof. Qiyao Huang, Dr. Fan Chen, Dr. Pengwei Wang, Dr. Ng Miya, Dr. Xian Song, Dr. Jiehua Cai, Dr. Leni Zhong, Dr. Qiuna Zhuang, Dr. Youchao Qi, Dr. Jingjing Fu, Dr. Yufei Zhang, Dr. Yanpeng Guo, Ms. Yuqing Shi, Ms. Liting Huang, Ms. Kemeng Zhou, Ms. Xinyi Zhang, Mr. Le Chen, Mr. Junjie Su, Mr. Xiaolong Zeng, Mr. Ruiheng Peng, Mr. Jiaheng Liang, and Mr. Ruochen Ding for their dedicated training, essential assistance, insightful discussions, and constructive suggestions throughout my research. I also sincerely appreciate the contributions of all technicians and collaborators actively involved in this project. I would like to extend my appreciation to the technical and support staff at the School of Fashion and Textiles, the Department of Applied Biology and Chemical Technology, and the School of Microelectronics for their invaluable assistance with sample characterization and analysis. Financial backing from the Southern University of Science and Technology and the Hong Kong Polytechnic University is gratefully acknowledged.

Lastly, my heartfelt thanks go to my family and wife for their constant love and encouragement, which have sustained me unfailingly throughout this journey.

TABLE OF CONTENTS

MONOLITHICALLY INTEGRATED IN-TEXTILE PATCH FOR WIRELESS EPIDERMAL BIOSENSING 1

ABSTRACT 4

ACKNOWLEDGEMENTS 8

TABLE OF CONTENTS 9

LIST OF FIGURES 14

LIST OF TABLES 27

CHAPTER 1: INTRODUCTION 29

1.1 Background and Challenges 29

1.2 Research Objectives 31

1.3 Research Originality 31

1.4 Outline of the Thesis 33

CHAPTER 2: LITERATURE REVIEW 35

2.1 Technology for Epidermal Sensing 35

2.1.1 Sweat monitoring 35

2.1.2 Wound monitoring 39

2.1.3 Electrochemical biosensors for selective and epidermal sensing 44

2.2 Advances in Textile-Based Electronics 51

2.2.1 Textile-based electronics in epidermal sensing 51

2.2.2 Fabrication method of textile-based electronics 54

2.2.3 Towards integrated textile-based sensing systems 56

CHAPTER 3: METHODOLOGY 61

3.1 Materials 61

3.2 Fabrication of Monolithically Integrated Systems 62

3.2.1 Fabrication of metallic textile 62

3.2.2 Fabrication of metallic pattern on textile 63

3.2.3 Fabrication of sensor electrodes 64

3.2.4 Fabrication of the hybrid in-textile wristband 66

3.2.5 On-body and real-time epidermal analysis with wireless bioelectronics 67

3.3 Characterization 67

CHAPTER 4: IN-TEXTILE PHOTOLITHOGRAPHY FOR FABRICATING METAL PATTERNS WITHIN TEXTILES 69

4.1 Introduction 69

4.2 Experiment 71

4.2.1 Fabrication of metallic cloth 72

4.2.2 Fabrication of metallic electrodes and interconnects on textile 72

4.2.3 Fabrication of micro-supercapacitors 73

4.2.4 Characterization 74

4.3 Results and Discussion 74

4.3.1 In-textile photolithography of conductive metal patterns in textiles 75

4.3.2 Permeable, robust and sub-100 μm conductive metal patterns in textiles 79

4.3.3 High-performance bioelectronics enabled by Cu patterns in textiles 87

4.4 Conclusions 90

CHAPTER 5: IN-TEXTILE SYSTEMS FOR MULTIPLEXED SWEAT BIOSENSING 91

5.1 Introduction 91

5.2 Experiment 93

5.2.1 Fabrication of K^+ sensor electrode 93

5.2.2 Fabrication of biosensor array for sweat monitoring 94

5.2.3 Assembly of the integrated in-textile sensing system 95

5.2.4 Characterization 96

5.3 Results and Discussion 97

5.3.1 Design and fabrication of integrated textile-based potassium monitoring system 97

5.3.2 Characterization of the monolithically integrated in-textile wristband 102

5.3.3 Wireless, on-body and real-time application with the integrated in-textile wristband 104

5.3.4 Fully integrated biosensing headband for multiplexed sweat monitoring 111

5.4 Conclusion 119

CHAPTER 6: IN-TEXTILE PATCH FOR WIRELESS WOUND BACTERIAL AND FUNGAL SENSING 121

6.1 Introduction 121

6.2 Experiments 123

6.2.1 Fabrication of textile aptamer-based sensor array 123

6.2.2 Assembly of in-textile patch 124

6.2.3 Characterization of textile wound sensors 125

6.2.4 Biocompatibility evaluation of wound biosensors. 125

6.2.5 Wound chronic infection modeling 126

6.3 Results and Discussion 127

6.3.1 Design and fabrication of the in-textile patch for wireless wound biosensing 127

6.3.2 Design and characterization of the wound biosensors 132

6.3.3 Biocompatibility evaluation of the wound biosensors 134

6.3.4 In situ wound monitoring in mouse models 138

6.4 Conclusions 142

Chapter 7: CONCLUSIONS AND SUGGESTIONS FOR FUTURE RESEARCH 144

7.1 Conclusions 144

7.2 Suggestions for Future Research 146

REFERENCES 149

LIST OF FIGURES

Figure 2. 1 The development for "smart" textile bioelectronics(*77*). 35

Figure 2. 2 Introduction of secreted sweat (*78*). 36

Figure 2. 3 Schematic diagram of sweat collection method (*87*). 37

Figure 2. 4 Different process stages from sweat sampling (*74*)..... 38

Figure 2. 5 The evolution of bandages since 2000 B.C. (*41*)..... 39

Figure 2. 6 a Wearable bioelectronics for sensing wounds and giving therapy when needed (regularly detecting, evaluating wounds, and monitoring in real-time). **b** Chronic wound healing consists of 4 phases. **c** The chemical composition of the wound sites(*39*). 40

Figure 2. 7 Delaying healing factor and therapeutic drugs for non-healing chronic wounds (*103*)..... 41

Figure 2. 8 Recent advances integrate these sensors with wireless systems (e.g., smartphone-linked dressings) for closed-loop therapy, such as on-demand drug release triggered by abnormal biomarker levels(*98*)..... 42

Figure 2. 9 Flexible wound sensing systems. **a** Wearable sensors for detecting different ions and temperature in wound sites. **b** An integrated electrochemical bioelectronic for inflammatory biomarkers. **c** Smart bandage for pH and temperature detection and drug delivery for treatment. **d** Sensor module for multiparameter wound detection(*98*)..... 43

Figure 2. 10 Different sweat sensing methods for electrochemical sensors. **a** Amperometry: glucose, lactate. **b** Potentiometry: H^+, Na^+, K^+, Ca^{2+}. **c** Differential pulse voltammetry: electroactive drug molecules(*109*)..... 44

Figure 2. 11 The principle of all-solid-state electrochemical sensors for single ion detection. 45

Figure 2. 12 Construction of working electrode and reference electrode based on textile. 46

Figure 2. 13 The textile sensors based on fabric or fibers(*112-115*). 47

Figure 2. 14 Schematic of the TNF-α aptamer sensor (*126*)..... 50

Figure 2. 15 The principle of MB-labelled aptamer sensor(*125-131*). 51

Figure 2. 16 Different transmitting methods for wireless textile electrochemical sensing system(*5, 67, 76, 132*). 51

Figure 2. 17 Schematic illustration of some communication possibilities for wearable point-of-care textile systems and the comparison for these communications possibilities (i.e., 4G/5G, Bluetooth, Wi-Fi, RFID). 52

Figure 2. 18 Different substrates for fabricating textile-based electronics. **a** Images of the microelectronics system. **b** Sensor networks based on NFC. **c** Image of electronic devices on a single microfiber. **d** Schematic diagram of textile electrochemical sensor system based on liquid metal(*138-141*)..... 54

Figure 2. 19 Textile-based electronics employ diverse fabrication techniques to enable wearable functionality. **a** A body area network utilizing metamaterials embedded in textiles for enhanced signal transmission **b** Digital embroidery,

where liquid metal fibers—comprising Galinstan-filled perfluoroalkoxy alkane (PFA) tubing—are stitched into fabrics to create conductive pathways. **c** Production of flexible textile circuits through layered printing and lamination processes. **d** Wearable microgrid system, with modular components strategically placed on a shirt for optimal performance and user comfort(*64, 67, 142, 143*)..... 55

Figure 2. 20 Connectors and joining technologies for electronic textiles. **a** Stitched connection. **b** Soldering and welding. **c** Crimping. **d** Adhesives and **e** connectors(*144*). 56

Figure 2. 21 Schematic illustrations of PAMD (*147*). 57

Figure 2. 22 Schematic illustration of "grafting-from" and "grafting-to" strategies developed for grafting the interfacial functional polymer in PAMD and the corresponding representative materials in use. (*147*). 60

Figure 3. 1 Schematic diagram of the PAMD process. 63

Figure 3. 2 The fabrication of double-sided photolithography for textile sensing systems. 64

Figure 3. 3 Structure of the electrodes of 2 types of wound sensors. **a** pH sensor. **b** Aptamer sensor..... 65

Figure 3. 4 Schematic diagram of signal-conditioning (potentiometric and amperometric) and wireless circuit. (Bluetooth, ADC part). 66

Figure 4. 1 Schematic illustration of in-textile photolithography. 76

Figure 4. 2 SEM images of Cu patterned PET fabrics. **a-b** SEM image of the photoresist-coated Cu-PET textile after the developing process. **c-d** Images showing the boundary of the Cu in PET fabrics after the etching process. ... 77

Figure 4. 3 Implementation of in-textile photolithography for creating metallic circuit architectures on fabric substrates. **a** Macroscopic view of a copper-based printed circuit board (PCB) design patterned onto polyester textile. **b&c** High-resolution scanning electron microscopy reveals the precise interface between deposited copper traces and textile fibers in both planar and cross-sectional orientations. **d&e** The technique's material versatility is evidenced by silver PCB patterns on polyester and nickel interdigitated electrodes with varying feature sizes. **f** Adaptation of this approach to glass-fiber textiles. .. 78

Figure 4. 4 SEM images of Cu lines in different textiles. **a** Cu pattern on glass-fiber textile. **b** Ni pattern on non-woven textile. 79

Figure 4. 5 Cu patterns on $Polyester_{0.94}$ made by different patterning methods. **a** Metal-textile boundary by in-textile photolithography. **b** Metal-textile boundary by an on-textile patterning method. 80

Figure 4. 6 SEM photos of Cu PET textile. **a** Sensor electrode. **b** Etched Cu cloth. 80

Figure 4. 7 A systematic evaluation of copper-coated textiles reveals distinct performance differences between in-textile photolithography and on-textile patterning methods. **a** Water vapor and air permeability of the textiles coated with Cu fabricated with different patterning methods. **b** Resistance changes

(R/R_0) of the Cu patterns fabricated with different patterning methods. **c** Linear resistance of the Cu patterns fabricated with different patterning methods... 81

Figure 4. 8 a Schematic illustration of the single-sided UV light exposure in photolithography. **b** Schematic illustration of the double-sided UV light exposure. 82

Figure 4. 9 a SEM photos of well-defined metal patterns in different PET textiles. **b** Linear resistance of the Cu PET patterns with different cover factors. 83

Figure 4. 10 Cu patterns Characterization with different widths. **a-c** Images showing the Cu patterns with different linewidths patterned in $Polyester_{0.90}$ textile, $Polyester_{0.94}$ textile, and $Polyester_{0.98}$ textile. (0.90, 0.94, and 0.98 are the cover factors of the polyester textiles). **d** Air and moisture permeability of the different PET textiles. 83

Figure 4. 11 Characterization of well-defined and conductive metal patterns in textiles. **a** Optical image (left), cross-sectional schematic diagram (top right), and SEM image (bottom right) of the Cu pattern fabricated by the in-textile photolithography method. **b** Optical image (left), cross-sectional schematic diagram (top right), and SEM image (bottom right) of the Cu pattern fabricated by on-textile patterning method (screen printing). **c** Comparison of water vapor and air permeability of the fabrics coated with Cu made by the in-textile photolithography method and the on-textile patterning method. Error bars represent the s.d. of the mean from three fabrics coated with Cu. **d** Comparison of resistance changes (R/R0) of the Cu patterns made by the in-textile photolithography method and on-textile patterning method. Inset is the digital image showing the flexibility of the Cu patterns made by two methods. **e** Linear

resistance of the Cu patterns as a function of the patterning resolution. Error bars represent the s.d. of the mean from three Cu patterns. 84

Figure 4. 12. High-performance supercapacitor enabled by in-textile lithography. **a** Mechanical testing revealed minimal alteration in tensile properties between pristine and metallized polyester fabrics. **b** Electrical durability assessments demonstrated stable conductivity of copper traces during extended bending (10,000 cycles, 4.4 mm radius), with linewidth-dependent resistance variations. **c** Washability tests showed gold-deposited interconnects exhibited superior stability (<20% resistance change after 20 cycles) compared to non-treated counterparts. **d** The metallized textiles also endured severe mechanical deformation, showing <15% resistance variation after 180 crumpling cycles. **e** Resistance upon 20 washing cycles. **f** Electrochemical characterization of nickel interdigital electrodes revealed linewidth-dependent capacitive behavior when coated with MnO_2 active material. 87

Figure 4. 13 a Electrochemical analysis revealed that the areal capacitance of micro-supercapacitors exhibited a clear dependence on electrode linewidth, with finer features demonstrating enhanced charge storage capacity. **b** Structural characterization through XRD confirmed the successful integration of MnO_2 with nickel interdigital electrodes, showing characteristic diffraction peaks of the composite material. **c-d** Microscopic evaluation via SEM revealed a homogeneous MnO_2 coating with porous morphology, providing high surface area for electrochemical reactions. **e** The practical application of this technology was demonstrated through a fully functional, double-sided temperature monitoring patch featuring precision-patterned copper circuits on polyester fabric. 89

Figure 5. 1 Schematic illustration of the wristband for real-time and wireless sweat K^+ monitoring..... 98

Figure 5. 2 The physical implementation and operational concept of the monolithic textile wristband. **a** A compact flexible patch (2.5 × 8 cm) demonstrating successful integration of electronic components with textile substrates. **b** A systematic architecture diagram outlining the signal pathway from electrochemical sensing to wireless data transmission 98

Figure 5. 3 a Schematic of an analog signal processing chain featuring impedance matching (voltage follower), programmable gain amplification, and active noise suppression (2nd-order low-pass filter), integrated with a 12-bit ADC and BLE transceiver for wireless connectivity. **b** A compact single-layer implementation on copper-metallized textile demonstrating successful miniaturization of conventional circuit elements onto flexible fabric substrates 100

Figure 5. 4 The fabrication process employed a precisely designed photomask. **a** A single-layer interconnect architecture with 1 mm trace widths. **B** High-resolution patterns printed on A4-format transparent substrates for accurate UV light projection during photoresist exposure. 100

Figure 5. 5 Fabrication and Characterization of Flexible Textile-Based Sensors. **a** The manufacturing process of the textile wristband begins with a versatile polyester (PET) substrate, which demonstrates exceptional flexibility when folded. **b** Metallization and patterning were achieved through a modified photolithographic process, with the resulting conductive traces exhibiting sharp, well-defined edges under polarizing microscopy. **c** The final textile-integrated circuits maintain the fabric's inherent properties while enabling

electronic functionality. **d** The flexible electrochemical sensor, comprising both working and reference electrodes directly patterned onto the textile. . 102

Figure 5. 6 The monolithically fabricated wristband demonstrated robust electrical performance through comprehensive testing. **a** Copper interconnect patterned directly onto the textile substrate. **b** Excellent conductivity in the flexible sensing platform. **c** Long-term stability testing revealed minimal resistance variation (<5% change) in the conductive traces over 90 days. **d** Electrochemical evaluation using artificial sweat showing a reliable potentiometric response from the potassium ion sensor, with signal processing modules accurately amplifying the open-circuit potential. 103

Figure 5. 7 The textile-based wearable device underwent comprehensive characterization to assess its functional properties. **a** The system maintained excellent breathability, as demonstrated through comparative permeability testing between unmodified PET fabric and the fully integrated sensor platform. **b** Quantitative measurements revealed outstanding air and moisture transport capabilities..... 104

Figure 5. 8 Scanning electron microscopy revealed distinct morphological characteristics at each fabrication stage **a** Pristine PET fiber displayed characteristic smooth surfaces with well-defined woven architecture. **b** PAMD-treated samples showed conformal copper coatings preserving the underlying textile structure. **c** Electrodeposited gold formed dendritic nanostructures uniformly distributed across copper-plated fibers. **d** Higher magnification imaging demonstrated three-dimensional gold growth originating from individual fiber surfaces..... 105

Figure 5. 9 The textile-based potassium sensor demonstrated robust analytical performance across multiple evaluation metrics. **a** Open-circuit potential measurements with excellent repeatability with <5% variation between consecutive measurements. **b** The system detection limitation. **c** Inter-device reproducibility testing across three sensor units showed <8% relative standard deviation in sensitivity. **d** The valinomycin-based membrane provided exceptional selectivity against common interferents. **e** Mechanical testing revealed stable operation through 120 bending cycles. **f** The sensor maintaining 92% of initial sensitivity after 30 days of storage. 106

Figure 5. 10 Demonstration of microfluidic channels. **a** The wearable platform incorporated engineered microfluidic channels fabricated through a layered assembly process. **b** Functional validation using artificial sweat demonstrated reliable liquid handling at physiologically relevant flow rates. **c** Illustration of the function of microfluidic channels. 107

Figure 5. 11 Bending characterization of the interconnect glued with Ecoflex. **a** Resistance changes over 3000 bending cycles. **b** The setup for bending and insulation test. **c** SEM photo after bending 3000 cycles. 109

Figure 5. 12 The monolithically integrated wristband demonstrating practical functionality during on-body trials. **a&b** Monitoring sweat potassium dynamics during exercise through synchronized operation of its textile-based sensors, microfluidics, and wireless electronics. **c** Mobile App for real-time K^+ monitoring. **d** Continuous data acquisition during endurance running revealed characteristic potassium fluctuation patterns correlating with exercise intensity. **e** Method validation against ICP-MS showed strong correlation across the physiological concentration range..... 110

Figure 5. 13 Characterization of the Au@Cu interconnects. **a** Resistance of the samples with different Au deposition times and $FeCl_3$ etching times. **b** SEM image of the Au@Cu-textile boundary. **c** Micro-structure of the Au coating. **d** SEM image of the Ecoflex encapsulation coating on interconnect regions. **e** Cross-sectional SEM image of the Ecoflex encapsulation coating on interconnect regions. f Resistance change of the Au@Cu pattern and the Ecoflex-coated Au@Cu pattern. 111

Figure 5. 14 Characterization of Ag/AgCl/PVB reference electrode. **a** Image of the metal-textile boundary by photolithography. **b** Image of the metal-textile boundary by screen printing. Cross-sectional SEM image of **c** metal-textile boundary by photolithography and **d** metal-textile boundary by screen printing. 112

Figure 5. 15 SEM images of sweat sensors. **a** PANI coating for the pH sensor. **b** Cross-section of the PANI. **c** SEM image of the PANI coating. **d** PEDOT: PSS coating for Na^+/K^+ sensors. **e** Cross-sectional image of the PEDOT: PSS. **f** Ion-selective membrane of the Na^+ sensors. **g** PB coating for Glucose/lactate sensors. **h** Cross-sectional image of the PB. **i** Enzyme membrane of the glucose sensors. 113

Figure 5. 16 The fabricated wearable array successfully integrated five distinct biosensors on a single textile platform. **a** Digital image of 5 different biosensors. **b-f** Systematic evaluation revealed optimized performance for each analyte. 114

Figure 5. 17 Long-term stability or drift for **a** pH sensor, **b** K^+ sensor, **c** Na^+ sensor, **d** glucose sensor and **e** lactate sensor. 115

Figure 5. 18 The selectivity for **a** pH sensor, **b** K^+ sensor, **c** Na^+ sensor, **d** glucose sensor and **e** lactate sensor. 116

Figure 5. 19 Biocompatibility of the sensor electrodes, polyester (PET) film, PDMS film, and commercial medical tape. 117

Figure 5. 20. Tensile properties of the original commercial polyester fabric and the one after in-textile photolithography. 117

Figure 5. 21 The wearable system incorporates a multiplexed sensor array seamlessly integrated into a textile headband. **a** Digital image of continuous sweat analysis system during physical activity with multiplexed sensing arrays. **b** The device operated through a streamlined signal acquisition and processing pipeline, where electrochemical sensors detect target biomarkers, and onboard electronics wirelessly transmit data to a paired mobile application. **c** Field testing demonstrated reliable functionality during exercise. 118

Figure 5. 22 On-body analysis of the patch for real-time sweat sensing. **a** Mobile application for 5 different biomarkers sensing. **b** Real-time sweat concentration during stationary cycling. 119

Figure 6. 1 Schematic of an advanced wound monitoring system designed for venous ulcer applications. **a** Illustration of a microenvironment of venous ulcers. **b** Illustration of biomarker-sensing textile dressing that conforms to wound beds for real-time infection surveillance. 128

Figure 6. 2 a Logical flow of the systematic design. **b** Photograph of the textile wound patch and its sensor arrays (2.5×2.5 cm). 129

Figure 6. 3 a Schematic diagram of signal conditioning and wireless circuit. **b** One-layer circuit design. 129

Figure 6. 4 Fabrication and characterization of as-fabricated conductive metal patterns and WIPEs platform **a** Scalable fabrication of over 120 patches of in-textile electrode/interconnects patterns in a 15 × 50 cm size. **b** Optical image of different layers functionalization during sensor fabrication. **c** SEM image showing the sharp boundary of the Cu pattern in a PET textile. **d** Waterproofness test of the LED matrix connected by an in-textile circuit with Ecoflex encapsulation. **e** The air and moisture permeability of different textile-based layers compared with non-permeable substrates. **f** In-textile Cu interconnects of the as-fabricated substrate of the WIPEs platform. 130

Figure 6. 5 **a** Resistances of in-textile Cu interconnects over a shelf life of one month. **b** The current readout of the WIPEs platform validated with a commercial electrochemical station. **c** A radar map of critical performances comparison. 131

Figure 6. 6 Fabrication process of the biosensor array in PET textile. 132

Figure 6. 7 Performance evaluation of as-fabricated sensor arrays. **a** The simple principal illustration of MB-labeled aptamer sensors. **b** The optimization of SWV method scanning (step pulse voltage). **c** The CV scanning of the bare Au textile in 0.5 M H_2SO_4. **d** Sensitivity of the potential responses of pH sensor. **e-h** The Sensitivity of the textile aptamer sensors. **i-m** SWV scans of the TNF-α, mouse TNF-α, IL-6 and fungi glucan sensors with different analyte concentrations. 133

Figure 6. 8 a-d The reproducibility of the corresponding three sensors. **e-h** Selectivity of the TNF-α, mouse TNF-α, IL-6 and fungal glucan sensors. **i-m** Long-term stability. 134

Figure 6. 9 a The cell survival rate of textile interconnects encapsulated with different insulation materials. **b** Live and dead cells in the blank control group, as well as in the experimental groups of epoxy glue and Ecoflex interconnects, were stained with AM/PI. 135

Figure 6. 10 The comprehensive evaluation encompassed both in vitro and in vivo analyses for biocompatibility. **a** Hemocompatibility testing of individual sensor layers. **b** In vitro cytotoxicity assessment via live/dead staining. **c** Longitudinal in vivo monitoring with unaltered murine body weight trajectories (±5% of control values) over 15 days post-subcutaneous implantation. **d** Histopathological examination of perimuscular tissue interfaces through H&E staining of Ecoflex-encapsulated sensor implantation sites. 137

Figure 6. 11 a The photograph of the wound area changes over time achieved in mice with different wound management platforms. The wound areas were covered with PI thin film, 3M medical tape and the as-prepared in-textile biosensing bandage. **b** The wound area changes over 2 weeks. 6.3.4 In situ wound monitoring in mouse models 138

Figure 6. 12 In situ wound monitoring on microbial infection in a mouse model. **a** Wound infection and monitoring study design. **b** Image of C. albicans cultivation from day 0 to 6. **c** Images of a freely moving mouse with biosensor arrays and WIPEs platform mounted on the skin wound. **d** H&E and Masson images of the wound muscle tissues on day 3 with bacteria and fungi infection. 139

Figure 6. 13 a Daily wound assessment with WIPEs on TNF-α concentration for 3 different mice. The inset of (a) are images of the wound changes in the wound area from days 0 to 6 when infected while day 4 is just for therapy. **b** Ex-situ TNF-α verification of wound exudate when infected by bacteria for 3 different mice (ELISA). **c** Daily assessment with WIPEs on fungi glucan concentration for 3 different mice. The inset of (c) are images of the wound changes in wound area from days 0 to 6 when infected while day 4 is just for therapy. **d** Ex-situ fungi verification of wound exudate when infected by fungi for 3 different mice (Absorbency). 140

Figure 6. 14 The daily assessment of pH levels with the WIPEs platform with validation. **a** Infected by bacteria (accuracy: 98.9%). **b** Infected by fungi (accuracy: 96.8%). 141

LIST OF TABLES

Table 2.1 Various potentiometric sensors have been applied for ammonium detection in the last ten years..... 46

Table 4.1 Comparison of the patterning resolution and electrical conductivity of conductive patterns developed by different patterning technologies reported in the literature. of textile..... 80

Table 6.1 Comparison of the air permeability and patch area of current wound sensing system reported in the literature..... 132

LIST OF ABBREVIATIONS

Polyester	PET
Carbon nanotubes	CNTs
polyaniline	PANI
poly(3,4-ethylenedioxythiophene):poly(styrene sulfonate)	PEDOT: PSS
Copper	Cu
Gold	Au
Nickel	Ni
Near field communication	NFC
Radio frequency identification devices	RFID
Polymer-assisted metal deposition	PAMD
Ion-selective electrode	ISE
Internet of Medical Things	IoMT
Microcontroller units	MCU
Analog digital converter	ADC

CHAPTER 1: INTRODUCTION

1.1 Background and Challenges

Recent breakthroughs in portable and wearable bioelectronics have substantially broadened their utility in personalized physiological tracking(*1-9*). These systems enable the non-invasive acquisition of health-relevant biomarkers through continuous, real-time data transmission to user interfaces(*10-12*). Sweat, serving as a valuable biomarker that includes electrolytes, metabolites, and disease indicators (e.g., elevated salt levels in cystic fibrosis), enables non-invasive monitoring of hydration status, muscle fatigue, and metabolic conditions(*13-18*). Meanwhile, chronic wound monitoring addresses a critical clinical gap: approximately 2% of the global population suffers from non-healing wounds, imposing an economic burden of $28–96.8 billion annually(*19-26*). Conventional monitoring methods, relying on invasive sampling or intermittent clinical assessments, lack the temporal resolution required for real-time physiological tracking(*27-35*). Although flexible electrochemical sensors have advanced multiplexed detection of ions, metabolites, and cytokines, fundamental limitations persist: sweat collection methodologies remain susceptible to sample degradation, while wound management systems lack integrated feedback mechanisms for therapeutic intervention(*36-38*).

Textile-integrated bioelectronics offer distinct advantages for epidermal sensing applications due to their inherent biocompatibility, mechanical conformability, and gas permeability(*39-44*). The direct incorporation of sensing elements into textile substrates enables prolonged skin contact without compromising wearer comfort. Conductive nanomaterials facilitate signal transduction through ion-to-electron conversion, enabling potentiometric detection with near-theoretical sensitivity(*45-53*). Innovations include microfluidic architectures for autonomous biofluid guidance, multiplexed sensing platforms for simultaneous parameter quantification, and theragnostic systems that combine biomarker detection with controlled drug

release(*54-59*). These developments establish textiles as functional substrates for the integration of next-generation diagnostics and therapeutics.

Recent advancements in materials science and microelectronics have positioned textiles as ideal substrates for wearable bioelectronics, leveraging their inherent breathability, biocompatibility, and conformal skin interface for continuous physiological monitoring(*60-63*). Conventional textile-based approaches, such as screen-printed conductive composites, often suffer from interfacial delamination due to mechanical property mismatches with the textile matrices(*64-66*). Digital embroidery enables robust electronic integration without compromising textile flexibility(*67-69*). Its utility in miniaturized systems is constrained by component spacing requirements (e.g., 1.77 mm for SOIC packages) and limitations on interconnect density.

Meanwhile, hybrid textile biological systems face significant hurdles. Sweat collection remains problematic: traditional methods (e.g., patches, microcatheters) suffer from sample evaporation and contamination, while novel microfluidic designs struggle with miniaturization and cost. Wound sensors must monitor complex biomarkers (e.g., TNF-α, ROS) across various healing stages, requiring multi-parameter integration that current technologies achieve only with costly micro-nano fabrication (*70*). Additionally, practical barriers like limited NFC transmission range (3–5 cm) and battery life restrict real-world usability. Developing useful and versatile epidermal bioelectronics for permeable integrated sensing systems represents an urgent priority, promising significantly improved comfort and wearability for long-term monitoring applications.

1.2 Research Objectives

In response to the challenges discussed above, this study focuses on developing a hybrid in-textile system for sweat and wound biosensing, utilizing photolithography-assisted PAMD. The detailed objectives are listed below:

1. Development of a hybrid textile-based patch for sweat sensing

a) Fabrication of electrochemical textile sensors, including fabrication of Cu PET cloth and sensor arrays.

b) Fabrication of a textile-based bioelectronic starting from simulation to optimization via Bluetooth

c) On-body analysis of wireless display, including real-time demonstration based on artificial sweat, and comparison of ex-situ calibration data with the on-body data

2. Development of a hybrid integrated in-textile patch for in-situ wound monitoring

a) Fabrication of electrochemical textile sensors for in-situ wound site monitoring

b) Design and fabrication of a wireless wound sensing system, starting from simulation to optimization

c) Biocompatibility in the mouse model and in situ study on wound exudates with chronic non-healing wounds

1.3 Research Originality

The rapid evolution of wearable bioelectronics has unlocked transformative potential for personalized health monitoring, yet existing systems often struggle to balance functionality, durability, and user comfort. This research introduces three monolithic in-textile platforms that address critical gaps in sweat analysis and the management of chronic wounds. Chronic wounds, which impose a global economic burden of $28–$ 96.8 billion annually, require real-time, multiplexed monitoring to detect infections

and track healing progress. Simultaneously, sweat, as a biofluid rich in electrolytes, metabolites and immune molecules, has remained underutilized due to limitations in sensor stability and textile breathability. This work bridges these challenges with a permeable, wireless wristband capable of continuous monitoring of sweat biomarkers and a textile-based wound patch that detects bacterial (TNF-α) and fungal (β-1,3-glucan) biomarkers alongside physiological metrics, such as pH and IL-6. By integrating sweat and wound sensing into textile-compatible platforms, the research provides a comprehensive solution for fitness tracking, disease management, and proactive wound care, marking a significant departure from conventional single-parameter devices.

Another cornerstone of this work is the development of a popular double-sided photolithography method, which overcomes longstanding barriers in fabricating high-resolution electronics on porous textiles. Traditional methods, such as screen printing or embroidery, suffer from poor resolution (>500 μm), mechanical fragility, and incompatibility with dense interconnects. By leveraging polymer-assisted metal deposition (PAMD), this research achieves sub-100 μm precision while mitigating capillary-driven ink diffusion in yarn structures. The resulting conductive traces exhibit metal-like conductivity (2×10^7 S m^{-1}) and exceptional durability, enduring 10,000 bending cycles and 20 washes with minimal conductivity loss (<5%). This innovation enables the integration of double-sided electronics without compromising breathability, as demonstrated by a multiplexed sweat sensor array (pH, K^+, Na^+, glucose, lactate) with embedded signal processing. The method's scalability and compatibility with industrial textile manufacturing processes position it as a transformative tool for next-generation wearable electronics.

Central to the system success is its monolithic design, which seamlessly integrates sensors, interconnects, and wireless components into a single textile layer. Unlike rigid or bulky wearables, the wristband and wound patch prioritize user comfort, exceeding medical tapes by an order of magnitude. The PAMD-fabricated circuits are encapsulated to ensure waterproofness while preserving textile porosity, a critical feature for prolonged wear. The wound patch further incorporates miniaturized chips that conform to dynamic skin surfaces, enabling reliable biomarker detection during

movement. This holistic design eliminates external hardware, merging clinic-grade functionality with everyday wearability—a balance rarely achieved in existing epidermal biosensors. The research also pioneers aptamer-based pathogen detection on textiles, addressing a gap in the monitoring of microbial infections. By functionalizing textiles with aptamers, the wound patch achieves multiplexed detection of TNF-α with relative standard deviations of 21%. This multi-pathogen detection capability, combined with cytokine tracking, enables a transition from reactive to predictive wound care, offering a paradigm shift in the management of chronic wounds.

Finally, the work prioritizes scalability, employing fabrication techniques like PAMD and photolithography that align with scalable textile production. The system's manufacturing process utilizes standard equipment, thereby reducing costs, while the platform washability and mechanical robustness meet consumer expectations for everyday use. These features accelerate adoption across fitness, healthcare, and military applications, where real-time monitoring and durability are essential. By harmonizing high-performance biosensing with user-centric design, this research redefines the standards for wearable bioelectronics, providing a scalable blueprint for seamlessly integrating electronics into textiles. The innovations presented here not only advance technical capabilities but also pave the way for practical, mass-market solutions that enhance personalized health monitoring and chronic disease management worldwide.

1.4 Outline of the Thesis

The thesis logic is organized as follows:

Chapter 1 provides a brief introduction to the general background of the research project topic and its associated challenges. The research objectives, as well as the significance and values, are also included.

Chapter 2 provides a comprehensive review of sweat and wound textile sensing systems, covering their background, sensing principles, fabrication methods, and integration techniques.

Chapter 3 provides a detailed introduction to the experimental methodology, including materials, design, fabrication processes, and characterization procedures.

Chapter 4 outlines a novel in-textile patterning strategy combining PAMD and double-sided photolithography. This technique generates robust, precisely defined, and uniquely three-dimensionally interconnected metallic architectures directly within textiles.

Chapter 5 initially describes a monolithic textile-integrated wristband (fabricated using PAMD) for the real-time wireless sensing of potassium ions (K^+) in sweat. The chapter then details the realization of a permeable, metallic cloth-based textile system that supports multiplexed electrochemical sensing, signal processing, and wireless data transmission with high durability.

Chapter 6 investigates a textile-integrated sensing platform for real-time wound monitoring and diagnostic assessment of infection status, including specific recognition of bacterial and fungal presence.

CHAPTER 2: LITERATURE REVIEW

In this chapter, we first discussed the background, significance, and detection method of sweat sensing and wound monitoring. Then, we introduced the advances of textile-based bioelectronics for electrochemical biomarker monitoring. Lastly, we discussed the connection and integration method for current textile-based bioelectronics.

2.1 Technology for Epidermal Sensing

Flexible and wearable electrochemical sensing systems have garnered considerable attention recently(*17, 18, 71-74*). Studies exist on flexible biosensors using portable detectors fabricated on polymeric substrates, such as PI, PET, SEBS elastomer, and PTFE(*7, 10, 75, 76*). Following the initial concept of the 1990s, which involved embedding electronics within clothing, this approach transitioned into healthcare. Progress in nanoelectronics and materials science has since driven developments in diagnostic tools, therapeutic devices, and energy systems(77), with core innovations occurring in sensing, actuation, and power generation components, as illustrated in Figure 2.1.

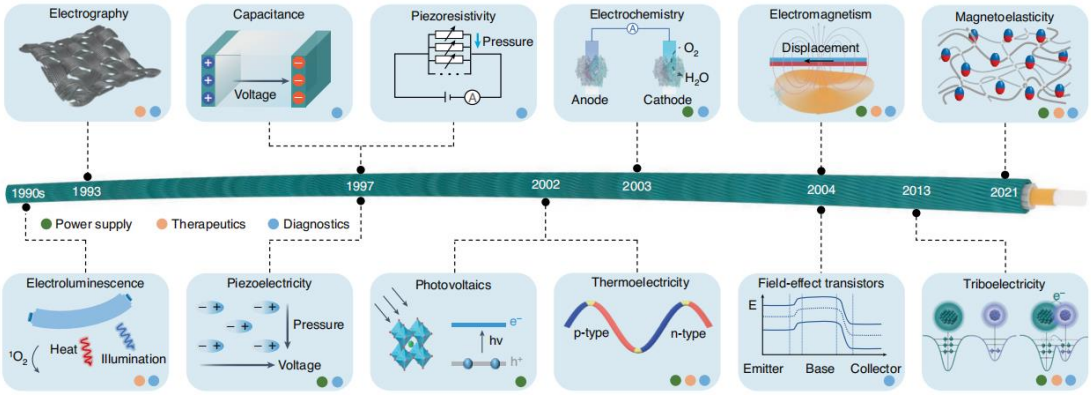

Figure 2. 1 The development for "smart" textile bioelectronics(*77*).

2.1.1 Sweat monitoring

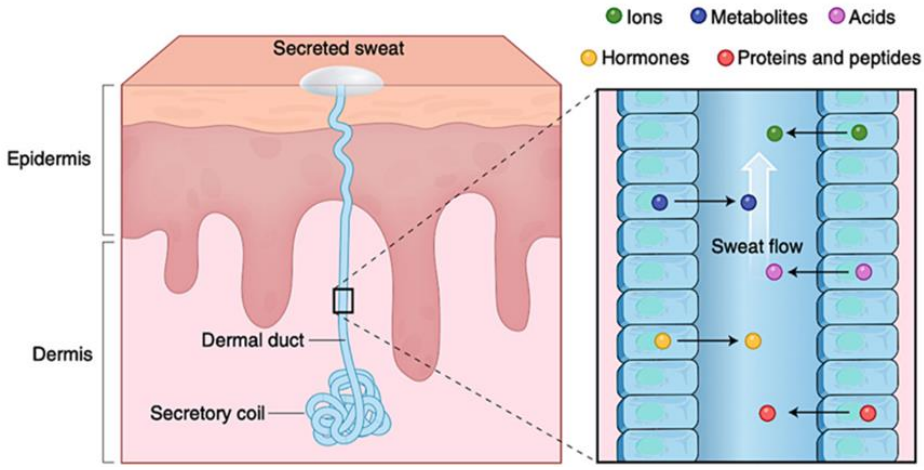

Figure 2. 2 Introduction of secreted sweat (*78*).

Sweat can be secreted by sweat glands, which include a variety of information related to the human body (Figure 2.2). By analyzing the biochemical indicators in sweat, individuals can gain a better understanding of their body's health status, including monitoring human movement, water loss, and muscle fatigue (*79-81*). In addition, sweat can also reflect certain diseases, such as a high salt concentration in sweat, which may be associated with cystic fibrosis(*82, 83*). Sweat offers distinct advantages over saliva and tears for non-invasive health monitoring due to its richer profile of chemical biomarkers. Consequently, sweat analysis has emerged as a significant focus in personalized medicine research, particularly for bodily fluid diagnostics(*84-86*). Market projections (2021 China In Vitro Diagnostics Outlook) indicate sustained global expansion in this sector, with an estimated ~5% compound annual growth rate pushing the in vitro diagnostics market to $79.2 billion this year. While emerging technologies, such as wearables and biosensors, coupled with intensifying cross-disciplinary research, signal future industry growth, their integration into medical, industrial, and consumer applications has progressed more slowly than anticipated. A significant limiting factor is the challenge of effective sweat collection: the obtained volumes are typically minute compared to other biofluids, prone to contamination from residual sweat, and the physiology of eccrine glands inherently alters the concentration of specific analytes relative to blood plasma levels.

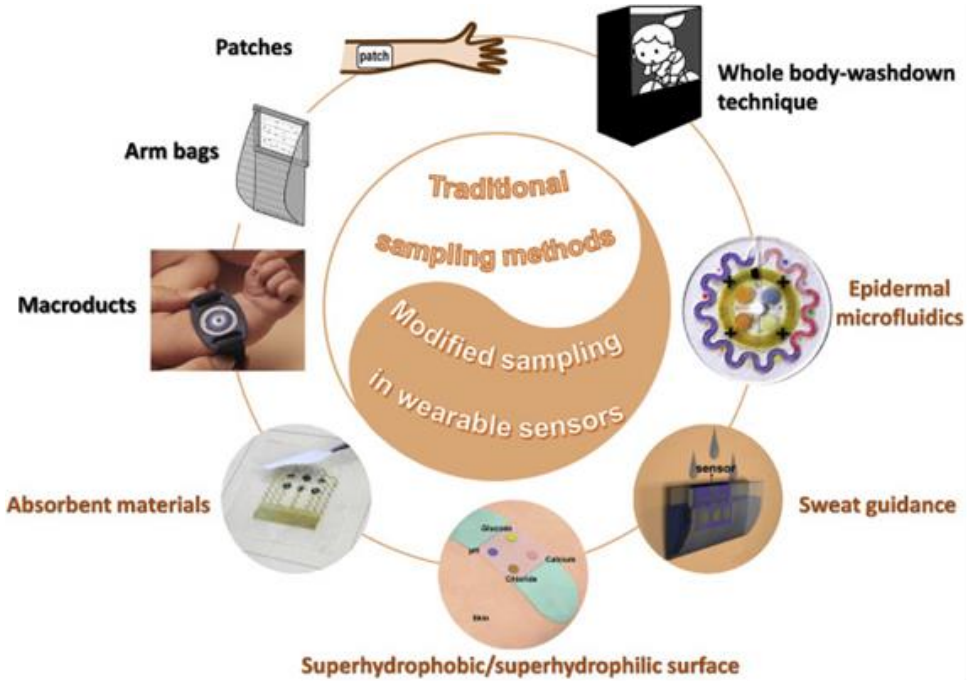

Figure 2. 3 Schematic diagram of sweat collection method (*87*).

Wearable sweat sensors have garnered significant research attention in recent years. Sweat analysis typically comprises four sequential stages: collection, extraction, storage, and detection. Research confirms that the composition of sweat is predominantly determined by the anatomical location and glandular origin of the secreted sweat (*88*). The accuracy of sweat electrolyte and metabolite concentrations varies with different sampling steps(*89, 90*). Figure 2.3 depicts four conventional sweat collection approaches: whole-body washing, localized patch collection, polymer bags/films, and microcatheter insertion(*91, 92*). These methods often suffer from decoupling from downstream analysis, which can lead to sample evaporation, degradation, or contamination. Moreover, they are generally incompatible with the demands of dynamic, real-time monitoring. Consequently, ongoing research focuses on innovating and refining sampling strategies. Integration with emerging wearable sensors and skin-conformable devices aims to achieve autonomous, continuous, and real-time monitoring of diverse health biomarkers via wearable platforms (e.g., garments, wristbands, patches)(*93-95*).

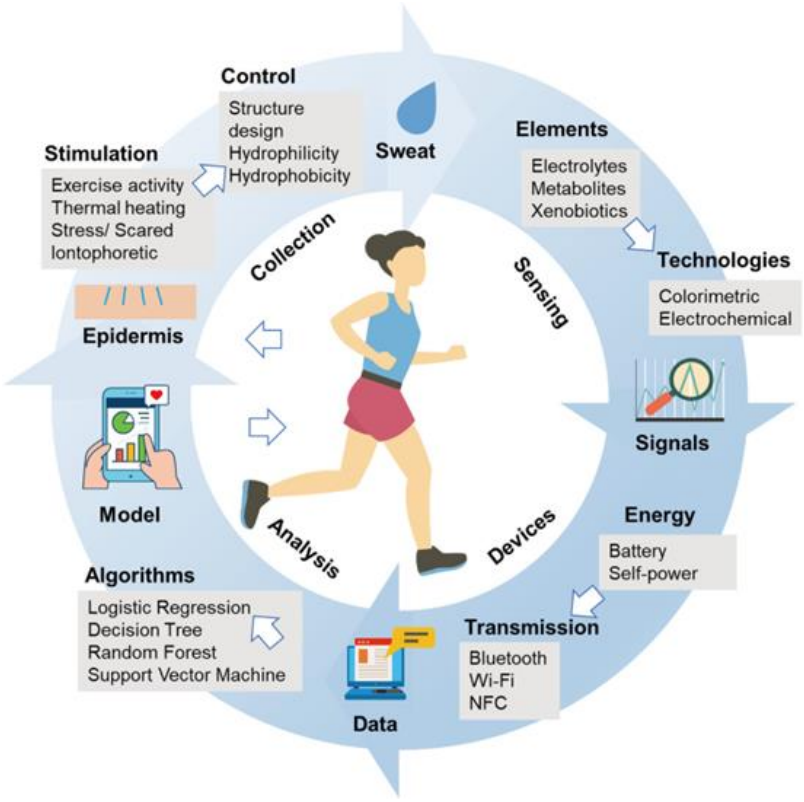

Figure 2. 4 Different process stages from sweat sampling (*74*).

Figure 2.4 outlines the process of sweat monitoring, including sweat secretion, collection, sensing, transmission, and analysis. Throughout the process, researchers have focused on identifying what can be detected in sweat, achieving accurate monitoring with limited sample volumes. For example, sweat is collected in various practical ways, and analyzing these different electrochemical signals remains a popular area of research. Algorithms play a versatile role in signal processing for software, while reducing similarity is essential for upholding academic integrity. In practice, integrating innovative algorithm applications with standardized academic writing ensures both technical value and original contribution. When troubleshooting software issues, hardware problems often come into view. For instance, various transmission methods and power supply options were utilized for bioelectronics, which will be introduced in the next section.

2.1.2 Wound monitoring

Chronic non-healing wounds fail to follow the typical stages of healing in a structured and timely manner, frequently becoming trapped in prolonged inflammation(*19*). Globally, approximately 2% of people suffer from chronic wounds, which often lead to severe outcomes such as limb loss or reduced life expectancy(*96*). The distinctions between acute and chronic wounds are substantial, with chronic wounds imposing a significant financial strain on healthcare systems, costing between $28 billion and $96.8 billion annually in treatment expenses(*97*). Conventional management of chronic wounds involves specialized medicated dressings tailored to the wound specific condition. However, these dressings cannot provide immediate data on wound status or progression, resulting in a lack of dynamic feedback and slower recovery. Current wound assessment methods are confined to lab-based analyses, with no practical, wearable solutions for continuous, on-site, and non-invasive monitoring.

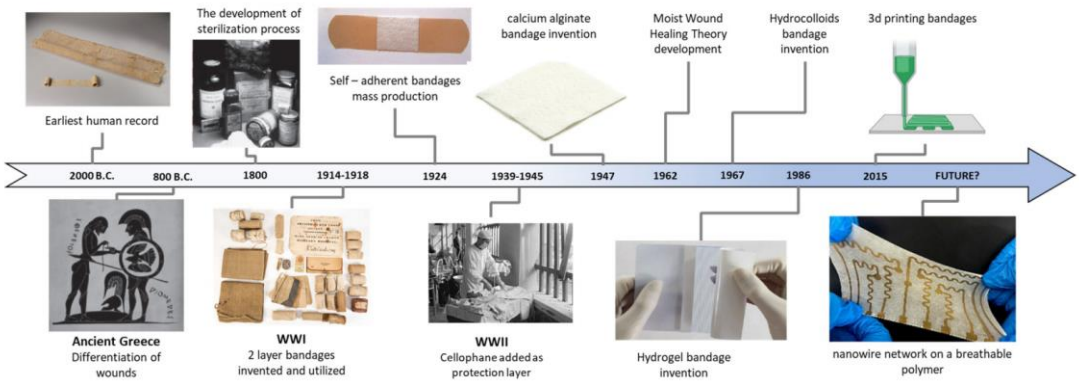

Figure 2. 5 The evolution of bandages since 2000 B.C. (*41*).

Figure 2.5 illustrates the evolution of bandage usage and design, a journey spanning approximately five millennia. This development began in Ancient Egypt, where linen was employed for wound coverage and exudate management. In addition, the Ancient Greeks further contributed by providing the first documented descriptions of various types of wounds. Key milestones include Prof. George D. Winter's introduction of the "Moist Wound Healing Theory" in 1962, Z.T. Piskozub's 1968 study on "Removing

Excess Exudate," and J.C. Lawrence's 1982 research on "Importance of Adherence to Tissue Damage." These advancements redefined the primary functions of bandages, leading to the development of more sophisticated designs(*98-104*). The integration of synthetic polymers, including polyethylene (PE), polyurethane (PU), and nylon, has significantly advanced wound care by leveraging modern material science. Since the early 2000s, breakthroughs in 3D printing and flexible electronics have paved the way for next-generation smart bandages. These innovative dressings have the potential to revolutionize chronic wound therapy by facilitating tailored treatment approaches, ultimately improving recovery rates and patient well-being.

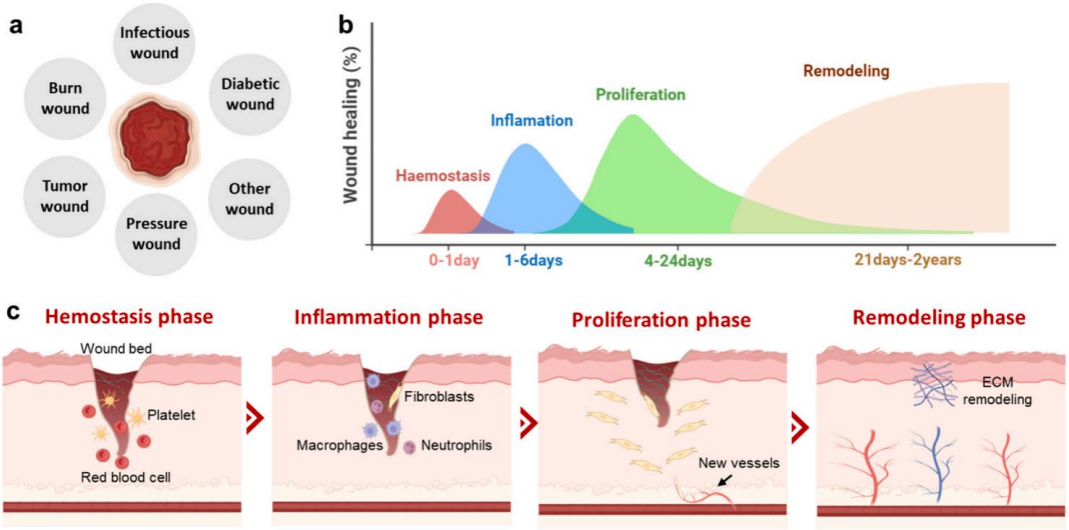

Figure 2. 6 a Wearable bioelectronics for sensing wounds and giving therapy when needed (regularly detecting, evaluating wounds, and monitoring in real-time). **b** Chronic wound healing consists of 4 phases. **c** The chemical composition of the wound sites(*39*).

Upon injury, hemostasis is triggered by vasoconstriction, which reduces bleeding. Platelets and fibrin then form a protective clot, sealing the wound and preventing infection. This is followed by vasodilation, which increases blood flow to deliver growth factors, neutrophils, and macrophages, initiating the inflammatory phase. Inflammation plays a vital role in removing bacteria and damaged tissue. Next, the proliferative phase begins, characterized by keratinocyte migration to regenerate the epidermal layer and

granulation tissue formation. Angiogenesis ensures adequate blood supply to support tissue regeneration. Finally, during remodeling, the extracellular matrix reorganizes to strengthen the wound site and restore skin integrity.

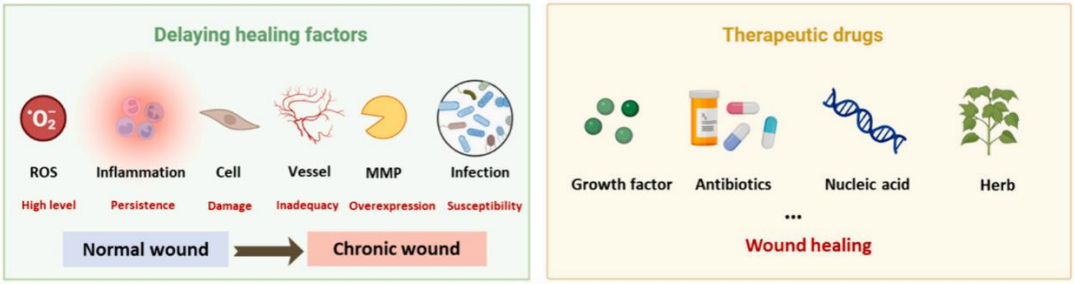

Figure 2. 7 Delaying healing factor and therapeutic drugs for non-healing chronic wounds (*103*).

In contrast to acute wounds, chronic wounds often experience impaired healing, becoming arrested in one or more phases of regeneration. Persistent infection, sustained inflammation, and insufficient oxygenation and nutrient delivery hinder tissue regeneration, preventing proper wound closure (Figure 2.7). For example, in diabetic wounds, chronic hyperglycemia increases oxygen demand, leading to cellular hypoxia and triggering excessive production of reactive oxygen species (ROS). These ROS molecules damage mitochondrial DNA and proteins, impairing endothelial cell function. Additionally, hypoxia in diabetic patients worsens inflammatory responses. The hyperglycemic microenvironment—characterized by elevated pH and temperature—further stimulates the overproduction of pro-inflammatory cytokines, such as TNF-α, IL-8, and IL-6, due to heightened reactive oxygen species (ROS) activity. Consequently, diabetic wounds exhibit excessive neutrophil accumulation, perpetuating inflammation and significantly delaying the healing process.

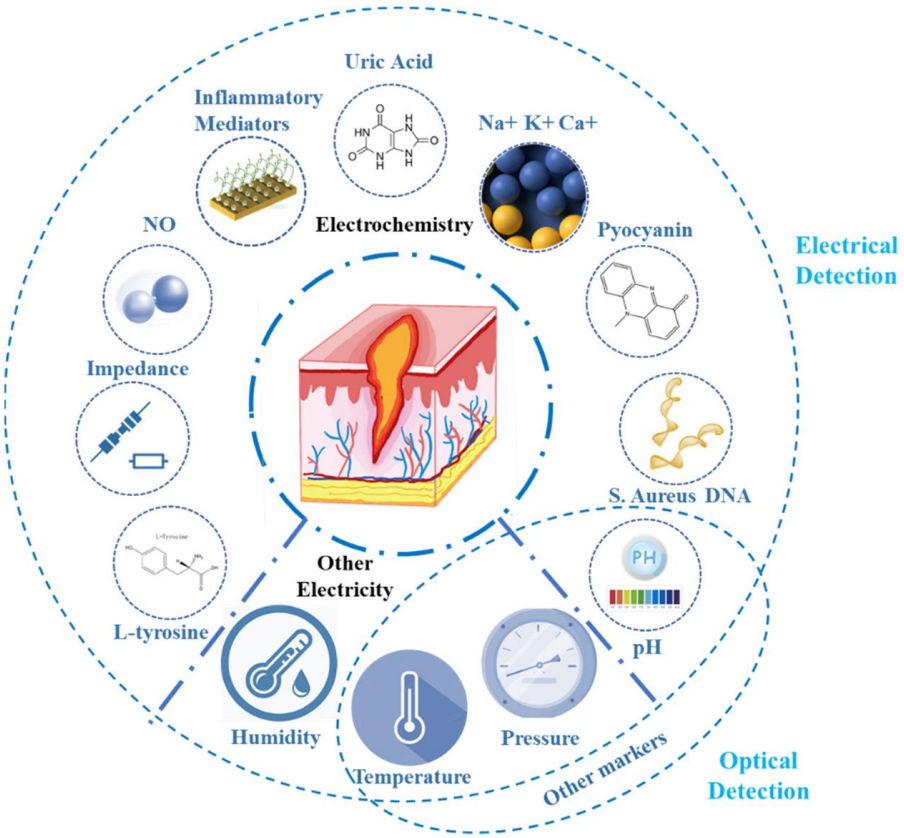

Figure 2. 8 Recent advances integrate these sensors with wireless systems (e.g., smartphone-linked dressings) for closed-loop therapy, such as on-demand drug release triggered by abnormal biomarker levels(*98*).

To address this challenge, researchers have developed innovative wound dressings that can track both physical and biochemical wound parameters (*36-38*). As illustrated in Figure 2.8, flexible wearable sensors utilizing electrical detection methods can identify critical biomarkers such as specific ions, uric acid, pyocyanin, and inflammatory signaling molecules. Beyond these, other clinically significant markers—including cytokines like IL-6, IL-1β, and acute-phase proteins such as CRP—have been shown to offer critical insights into wound progression and healing status(*105*). Recent advancements have led to the development of integrated biosensing platforms that combine multiple detection capabilities on a single chip. These systems enable simultaneous measurement of diverse wound parameters, paving the way for more precise monitoring and adaptive therapeutic interventions. Such innovations not only

promise to transform routine wound care but also hold particular value for improving outcomes in trauma and military medicine, where real-time physiological data can guide life-saving decisions(*45*).

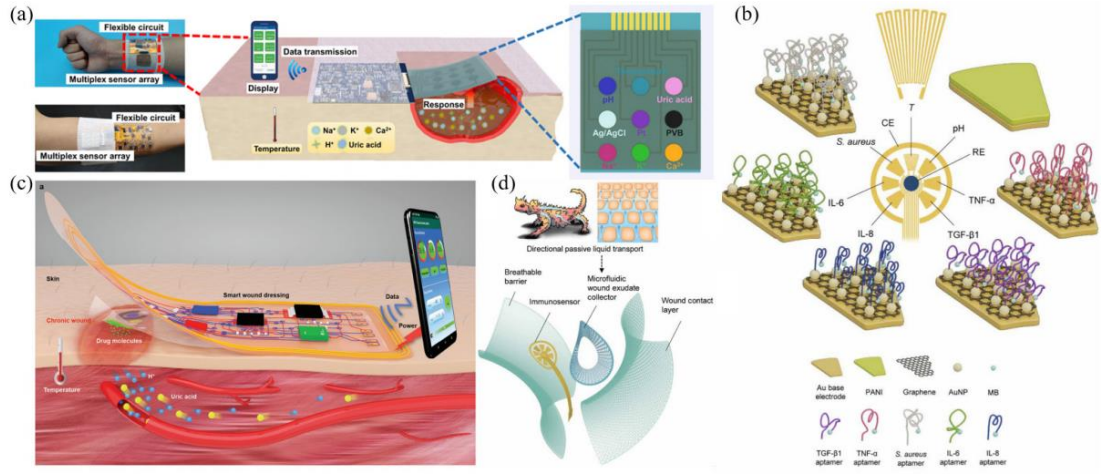

Figure 2. 9 Flexible wound sensing systems. **a** Wearable sensors for detecting different ions and temperature in wound sites. **b** An integrated electrochemical bioelectronic for inflammatory biomarkers. **c** Smart bandage for pH and temperature detection and drug delivery for treatment. **d** Sensor module for multiparameter wound detection(*98*).

The dynamic and multifaceted nature of wound pathophysiology necessitates monitoring beyond single-parameter analysis. Advanced sensor systems now utilize micro- and nanofabrication to achieve high integration for comprehensive wound assessment. Liu et al. engineered a flexible, multiplexed sensing platform capable of concurrently detecting electrolytes (Na^+, K^+, Ca^{2+}), pH, uric acid, and temperature, enabling real-time wound profiling (Figure 2.9a) (*106*). Gao et al. developed a wearable electrochemical device that synergistically evaluates inflammatory markers, microbial activity, and biochemical changes, providing insights into infection and healing progression (Figure 2.9b) (*107*). For example, Xu et al. introduced a smart bandage that integrates sensing and actuation (Figure 2.9c)(*108*). Its features include: a bioinspired microfluidic exudate sampler mimicking Texas lizard skin (Figure 2.9d) for efficient fluid collection, an electrochemical array quantifying cytokine (TNF-α, IL-6 and IL-8), bacterial load (S. aureus), and physicochemical parameters On-demand drug delivery to

target pathogens based on sensor feedback These systems exemplify the shift toward precision wound care, where integrated diagnostics and therapeutics optimize healing outcomes.

2.1.3 Electrochemical biosensors for selective and epidermal sensing

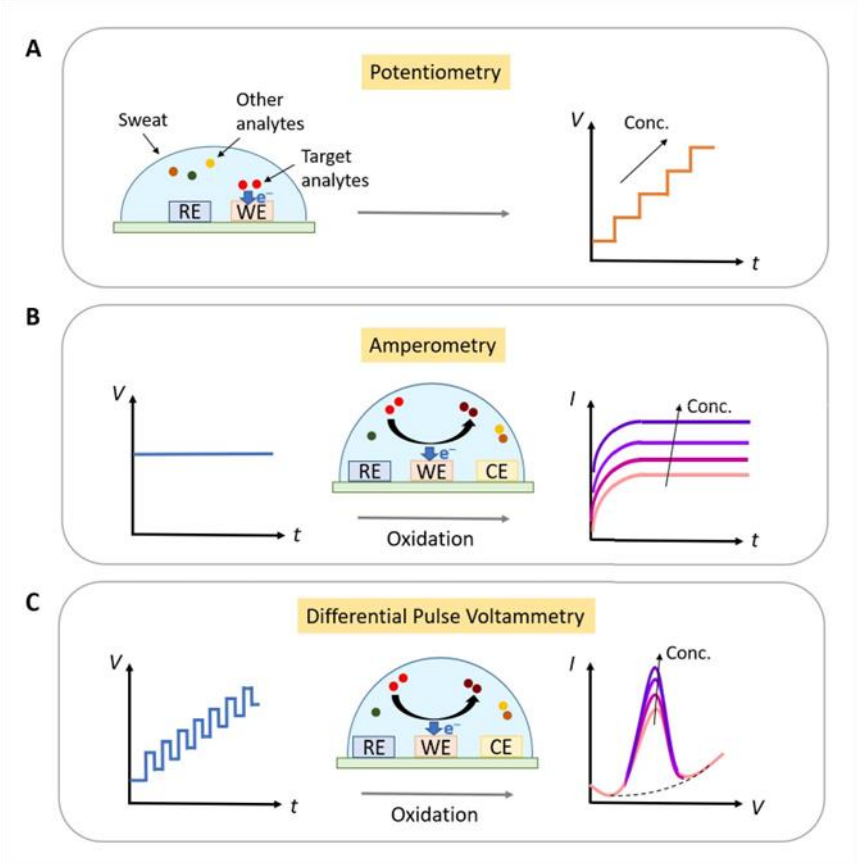

Figure 2. 10 Different sweat sensing methods for electrochemical sensors. **a** Amperometry: glucose, lactate. **b** Potentiometry: H^+, Na^+, K^+, Ca^{2+}. **c** Differential pulse voltammetry: electroactive drug molecules(*109*).

Figure 2.10 illustrates three fundamental electrochemical sensing approaches: potentiometric, amperometric, and differential pulse voltametric systems. Each method employs distinct operational principles for detecting the analyte. The first configuration utilizes an ion-selective membrane as the recognition element, creating a measurable potential difference between working and reference electrodes. In my study, I employ a

two-electrode potentiometric system, which represents the most established approach for ion detection. The system operates under equilibrium conditions with minimal current flow, where the ion-selective membrane (containing specialized ionophores) generates a membrane potential proportional to target ion activity. The second configuration is implemented in a three-electrode configuration, which monitors current changes resulting from electrochemical oxidation of target molecules at a fixed applied potential. The detection mechanism can utilize either enzymatic or direct oxidation pathways. The second configuration applies a stepped potential waveform to enhance sensitivity for detecting redox-active compounds, beneficial for pharmaceutical analysis.

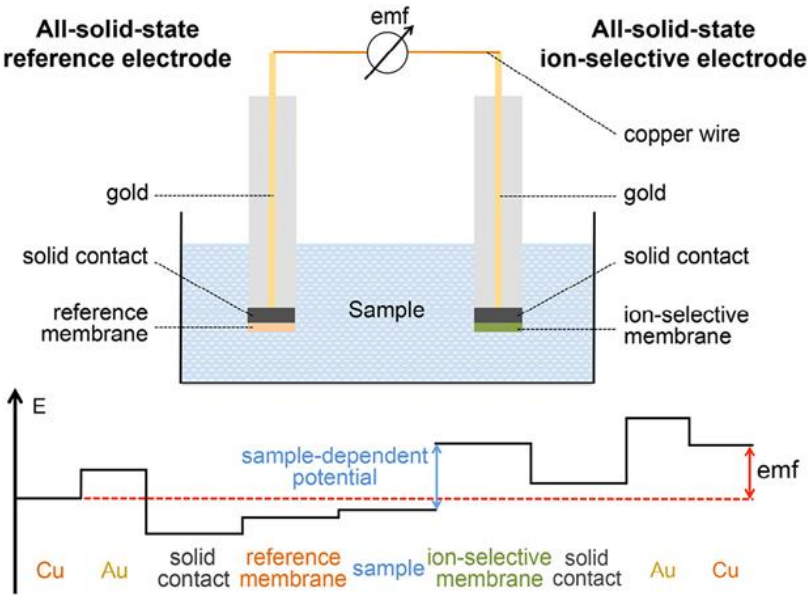

Figure 2. 11 The principle of all-solid-state electrochemical sensors for single ion detection.

Figure 2.11 illustrates an all-solid-state sensor comprising two key components: a reference electrode and a working electrode. When exposed to sweat samples of different ionic concentrations, this configuration generates distinct potential variations. The system measures these voltage changes through high-impedance detection, enabling precise monitoring of ion levels. This fundamental principle allows for quantitative analysis of ionic species in biological fluids. The relationship between the measured

potential (E) and ion concentration follows the Nernst equation, which for a complete electrochemical cell can be expressed as:

$$E = E_0 + \frac{RT}{nF} \ln \frac{C_{ox}}{C_{red}} \quad (1)$$

where E_0 represent the standard electrode potential, $\frac{RT}{F}$ denotes the temperature-dependent Nernstian coefficient, n signifies the electron transfer stoichiometry and $\frac{C_{ox}}{C_{red}}$ reflects the activity ratio of oxidized to reduced species.

For proton detection, $E - E_0$ demonstrates a characteristic 59 mV response per decade change in H^+ activity at 25°C. Therefore, the gate potential is adjusted by ion concentration, resulting in a change in the current response. Since the reducing matter (sensitive layer) is in a solid state ([Red]=1]), the potential difference is proportional to the log of the ion concentration. This electrochemical principle enables the modulation of gate potential in a concentration-dependent manner, which subsequently alters the measured current. When employing solid-state redox materials (where [Red] remains constant at unity), the potential difference varies logarithmically with target ion activity, forming the basis for quantitative ion-selective measurements.

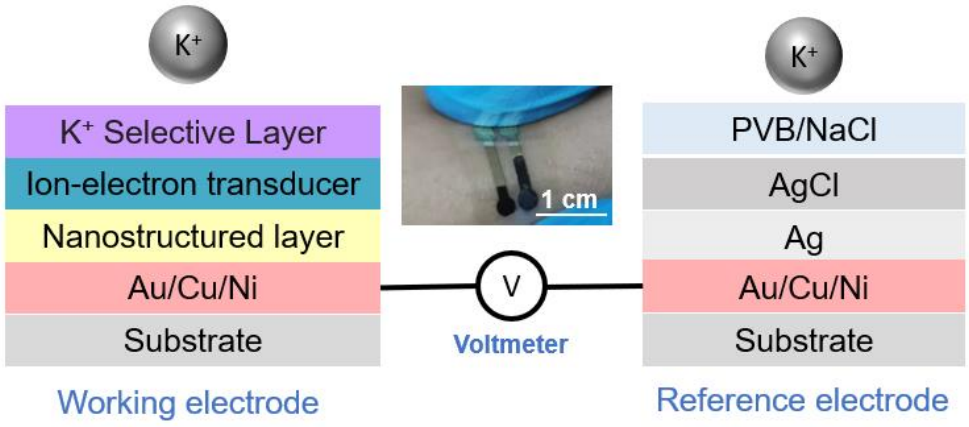

Figure 2. 12 Construction of working electrode and reference electrode based on textile.

Figure 2.12 illustrates the electrode architecture typically employed in flexible electrochemical sensors. The potassium-selective membrane incorporates valinomycin

as the recognition element, while PEDOT: PSS serves as an ion-to-electron transducer. A dendritic gold nanostructure layer improves sensor performance by increasing sensitivity and accelerating response times. The current collector utilizes a multilayer Au/Cu/Ni film, complemented by an all-solid-state Ag/AgCl reference electrode, which ensures stable potential measurements. For the K^+ sensor configuration, 10 μL of reference solution was deposited on the reference electrode. When sweat enters the sensing area between these parallel electrodes, it generates measurable potential changes. Despite the superior bending capability and good performance of flexible bioelectronics, conformal devices with breathability and comfort are greatly restricted by the substrate. Due to the evolution of materials and electronics, textile is a commonly used material for wearable bioelectronics. Bioelectronics fabricated on textiles allow direct contact with the skin while maintaining permeability and biocompatibility. Recent advances in materials science have enabled the development of textile-integrated biosensors capable of detecting various biomarkers, including electrolytes (Na^+, K^+, NH_4^+), metabolites (glucose, lactate), and pH levels in biological fluids(*110-114*).

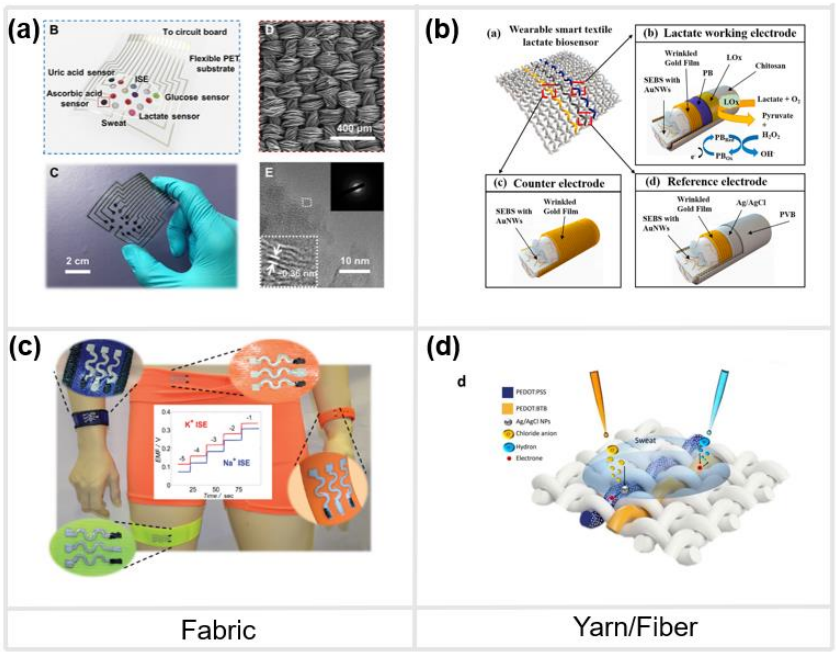

Figure 2. 13 The textile sensors based on fabric or fibers(*112-115*).

Textile-integrated electrochemical sensors offer multiple benefits, making them particularly suitable for wearable applications, including excellent breathability, mechanical flexibility, skin compatibility, and resistance to repeated washing. As depicted in Figure 2.13, contemporary textile-based electrodes exhibit performance metrics (such as sensitivity and signal stability) comparable to those of conventional designs. A comparative analysis in Table 2.1 reveals that these sensors achieve competitive detection limits and dynamic ranges for biomarker monitoring in physiological fluids, while maintaining strong reproducibility and molecular selectivity, crucial characteristics for clinical implementation. Common substrate materials include cost-effective and sustainable options like polyester fabric, carbon filaments, silk textiles, and metallic yarns. For signal transduction, these systems typically employ conductive polymers (e.g., PEDOT: PSS) or carbon nanomaterials that efficiently convert ionic signals to electronic signals.

Analyte	Textile	Nano-structure	Ion-electron Transducer	Sensing range (mM)	Sensitivity (mV)	Drift (mV/h)	Ref.
pH, K^+, NH_4^+	Cotton yarn	Carbon nanotubes (CNT)	CNT	pH: 3.0–11.0 K^+: 0.01-100	59	0.25	(*110*)
K^+, Na^+	Polyurethane (PU)	CNT	CNT	0.1 - 100	K^+: 56 Na^+: 54	-	(*114*)
Na^+	Carbon fibers	Multi-walled carbon nanotubes (MWCNTs)	MWCNTs	1 -100	Na^+: 56	1.3	(*111*)
pH, NH_4^+ Na^+	PET fiber, steel thread	-	Conductive carbon ink	Na^+:1-1000 K^+:0.1-100 pH: 4 - 8	Na^+: 52 $NH4^+$: 60.8 pH: 62.3	2	(*116*)

K^+, Na^+, glucose, lactate	Nitrogen-doped carbon textile	N-doped graphitic nanocarbon structure	PEDOT: PSS (polymerization)	K^+: 1.25 - 40 Na^+: 5 - 100	K^+: 31.8 Na^+: 51.8	-	(*113*)
Cl^-	Cotton, silk and polyester	Ag/AgCl nanoparticles	PEDOT: PSS (drop casting)	0.1 – 100	82	-	(*115*)

Table 2.1 Various potentiometric sensors have been applied for ammonium detection in the last ten years.

Cellular cytokines serve as vital mediators of immune function, facilitating critical intercellular communication during both innate and adaptive immune activation(*46*). Among these biomarkers, tumor necrosis factor-α (TNF-α) emerges as a particularly significant inflammatory indicator, participating in numerous physiological and pathological processes(*117*). This pro-inflammatory cytokine demonstrates rapid elevation following neural tissue damage and contributes to cellular necrosis and apoptosis. Beyond acute injury responses, TNF-α overexpression has been implicated in chronic conditions such as autoimmune disorders (rheumatoid arthritis, psoriasis) and vascular pathologies (atherosclerosis), as illustrated in Figure 2.14. Contemporary detection strategies have evolved beyond conventional antibody-based techniques (ELISAs) that often require complex washing protocols and costly reagents(*118*). Aptamer-based biosensors present a compelling alternative, offering several advantages including engineered nucleic acid sequences with tunable binding affinities, integrated signal transduction capabilities within a single molecular construct and enhanced specificity for target biomolecules compared to traditional immunoassays. Recent advances in inductive biosensor design have enabled the simultaneous capture of analytes and the generation of signals, driving significant research interest in aptamer-based platforms for cellular biomarker detection(*117, 119-125*). These developments demonstrate particular promise for monitoring wound inflammation dynamics and evaluating therapeutic interventions.

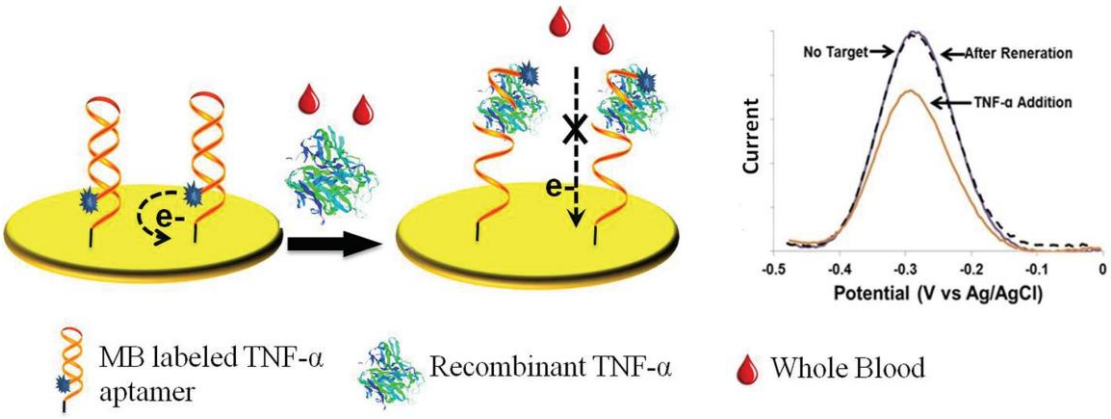

Figure 2. 14 Schematic of the TNF-α aptamer sensor (*126*).

The developed aptamer-based biosensor enables sensitive electrochemical detection of TNF-α in complex biological matrices, including undiluted human blood. As illustrated in Figure 2.15, the sensing mechanism relies on target-induced structural reorganization of the aptamer (*126*). Upon TNF-α binding, the conformational change alters the spatial relationship between the redox reporter and electrode surface, generating a quantifiable signal modulation. This platform demonstrates several key advantages:

- Regenerative capability through urea treatment (7 mM buffer solution)
- Reusability across multiple measurement cycles
- Detection sensitivity of 1 ng/mL in whole blood - comparable to established clinical ranges (1-20 ng/mL)

The operational principle involves a folded aptamer configuration that positions the methylene blue (MB) reporter near the electrode in the absence of target, facilitating efficient electron transfer. Target binding induces a structural rearrangement that increases the reporter-electrode distance, resulting in measurable current attenuation. This reversible mechanism enables repeated analyte quantification while maintaining consistent performance characteristics(*127*).

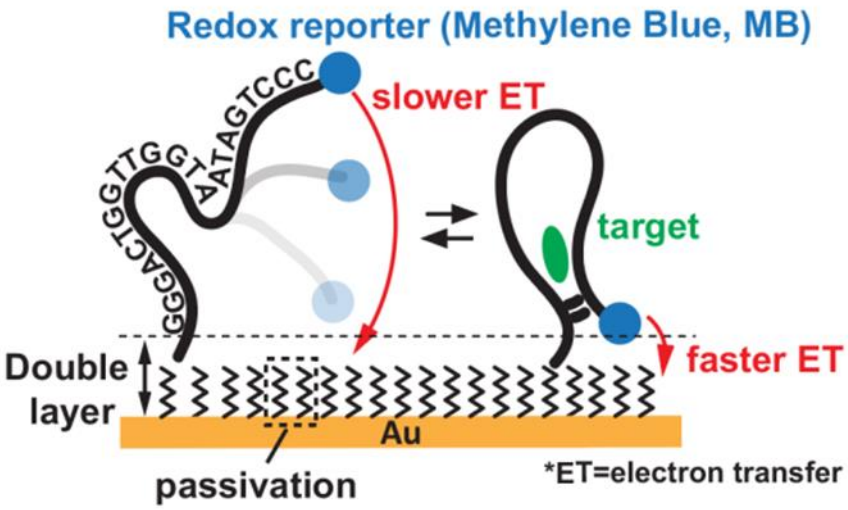

Figure 2. 15 The principle of MB-labelled aptamer sensor(*125-131*).

2.2 Advances in Textile-Based Electronics

2.2.1 Textile-based electronics in epidermal sensing

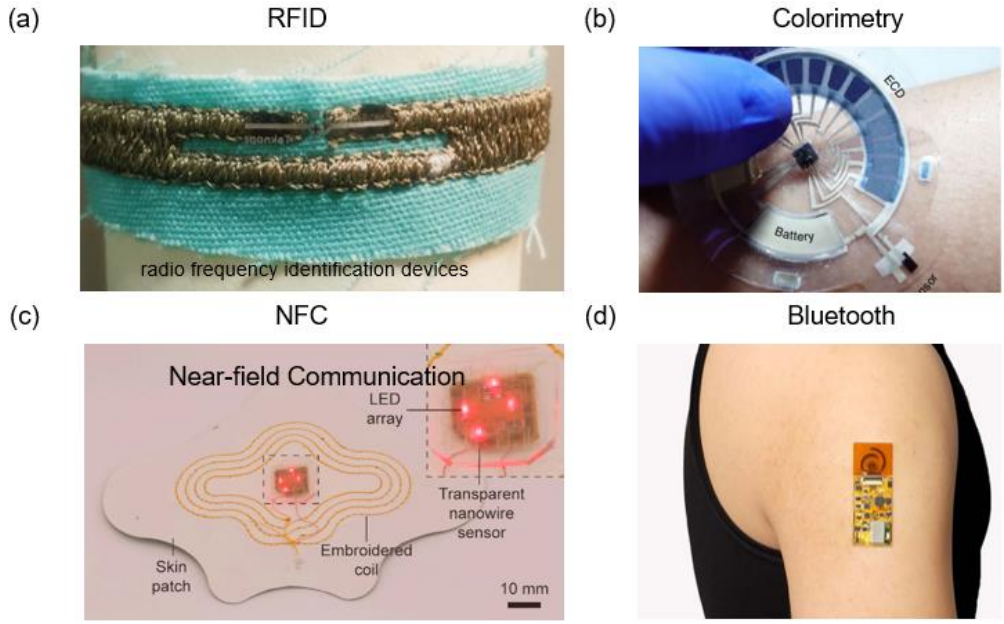

Figure 2. 16 Different transmitting methods for wireless textile electrochemical sensing system(*5, 67, 76, 132*).

Recent advances in wearable sweat monitoring have leveraged multiple wireless communication technologies, including RFID, NFC, Bluetooth, and Wi-Fi (Figure 2.16), enabling short-range, real-time data transmission. These methods are suitable for short-distance communication and transmit the signal in real-time. For instance, Gao et al. developed a flexible patch capable of 24-hour sweat analysis, demonstrating the potential for continuous biomarker tracking(*67, 133*). Textile-integrated systems often incorporate conductive metal fibers for NFC-enabled temperature sensing, though their utility is limited by short transmission ranges (3–5 cm). While textile-embedded electronics offer promising applications, mechanical mismatches can lead to structural failures (e.g., delamination), and non-monolithic designs (e.g., replaceable sensors) may compromise the inherent benefits of textile integration(*64-66*). Alternatively, modular button-based systems—combining sensors, power sources, and wireless components—provide a versatile solution for retrofitting existing garments(*134, 135*). Given these considerations, this project adopts Bluetooth for textile-based sweat sensing due to its balance of range, energy efficiency, and compatibility with wearable systems.

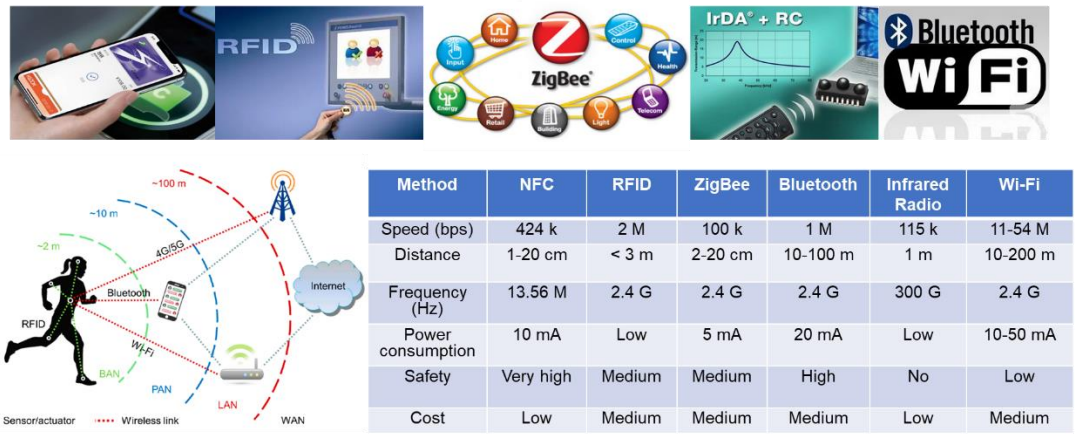

Method	NFC	RFID	ZigBee	Bluetooth	Infrared Radio	Wi-Fi
Speed (bps)	424 k	2 M	100 k	1 M	115 k	11-54 M
Distance	1-20 cm	< 3 m	2-20 cm	10-100 m	1 m	10-200 m
Frequency (Hz)	13.56 M	2.4 G	2.4 G	2.4 G	300 G	2.4 G
Power consumption	10 mA	Low	5 mA	20 mA	Low	10-50 mA
Safety	Very high	Medium	Medium	High	No	Low
Cost	Low	Medium	Medium	Medium	Low	Medium

Figure 2. 17 Schematic illustration of some communication possibilities for wearable point-of-care textile systems and the comparison for these communications possibilities (i.e., 4G/5G, Bluetooth, Wi-Fi, RFID).

Device-to-device (D2D) communication is the foundation for creating fully connected, smart healthcare textiles(*136*). Wireless technologies are crucial for linking these electronic components, with three primary methods being widely used. Near-Field Magnetic Induction, which includes Near-Field Communication (NFC), transfers data and power through magnetic fields between coils(*137*). It is a low-cost, low-power solution ideal for short-range connections (up to 10 cm). Its high efficiency makes it attractive for powering wearable devices. It is often integrated with conductive threads in textiles, where the threads handle longer-distance transmission and the inductive patterns manage short-range, wireless links. Far-field technologies use radio waves to transmit data over longer distances at high speeds. A common approach is to combine complementary methods. For instance, a system might use low-power RFID (which is the basis of NFC) for short-range device operation, while employing Bluetooth for longer-distance data collection(*132*). Another method uses the human body itself as a transmission medium. For example, radio surface plasmons can travel along conductive textiles, confining signals close to the body to enhance both energy efficiency and data privacy. Ultrasonic transmission through body tissue is particularly advantageous for implanted devices, as it eliminates the need for physical access. Because sound travels much slower than radio waves in tissue, ultrasonic wavelengths are shorter. This allows for highly directional communication even with small transducers, providing a precise and efficient link. Bluetooth is a widely adopted, moderate-cost communication technology for point-of-care textile systems. It provides reliable data transmission within a range of 10 to 100 meters, making it suitable for portable use in both clinical and home-based patient monitoring. The impact of transmission distance and physical obstructions on signal attenuation for this application is illustrated in Figure. 2.17.

2.2.2 Fabrication method of textile-based electronics

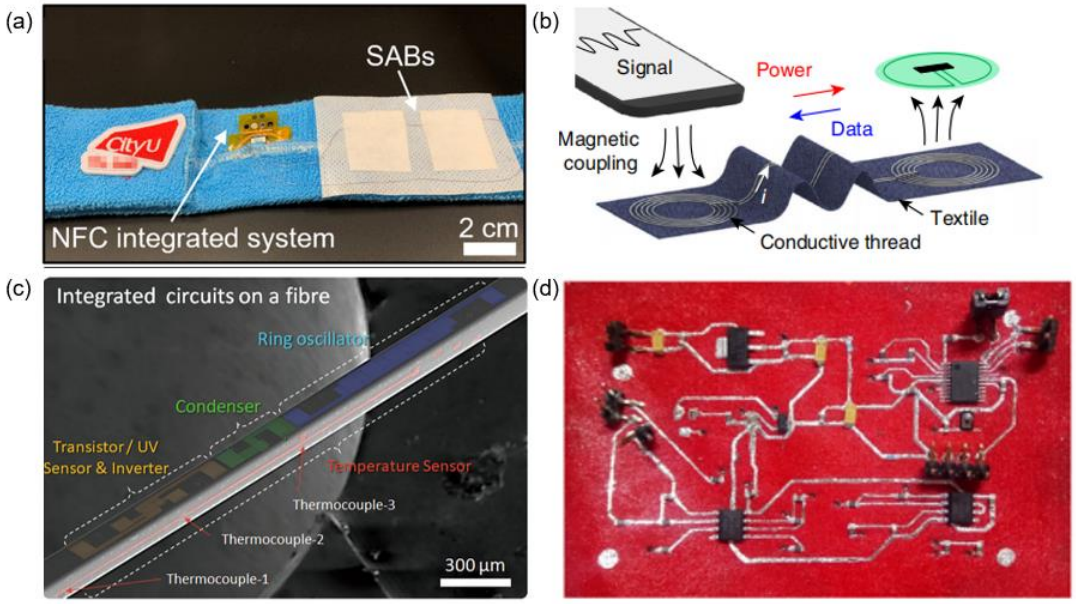

Figure 2. 18 Different substrates for fabricating textile-based electronics. **a** Images of the microelectronics system. **b** Sensor networks based on NFC. **c** Image of electronic devices on a single microfiber. **d** Schematic diagram of textile electrochemical sensor system based on liquid metal(*138-141*).

Textile-integrated electronic systems offer versatile solutions for wearable sensing by embedding flexible components into fabrics or fibers. Figure 2.18a illustrates a stretchable microelectronic system (SMS) that integrates an ultra-thin SABs-powered module with a sweat-sensing platform, featuring a biosensor for physiological analysis and an NFC-enabled circuit for wireless data transmission. This lightweight, conformable design allows seamless attachment to clothing for on-body monitoring (*140*). NFC-enabled bright garments eliminate the need for batteries by utilizing inductive coupling, with conductive silver threads woven into the fabric to relay signals across the garment (Figure 2.18b)(*138*). Another approach involves fabricating microelectronic circuits on ultrathin fibers (150 μm diameter) via precision lithography and capillary coating techniques, enabling high-density integration of functional components (Figure 2.18c) (*139*). Additionally, a PET-based textile circuit with modular

electrodes utilizes electrochemical sensing, paired with specialized circuitry to amplify faint nanoampere-level signals while filtering out noise (Figure 2.18d)(*141*).

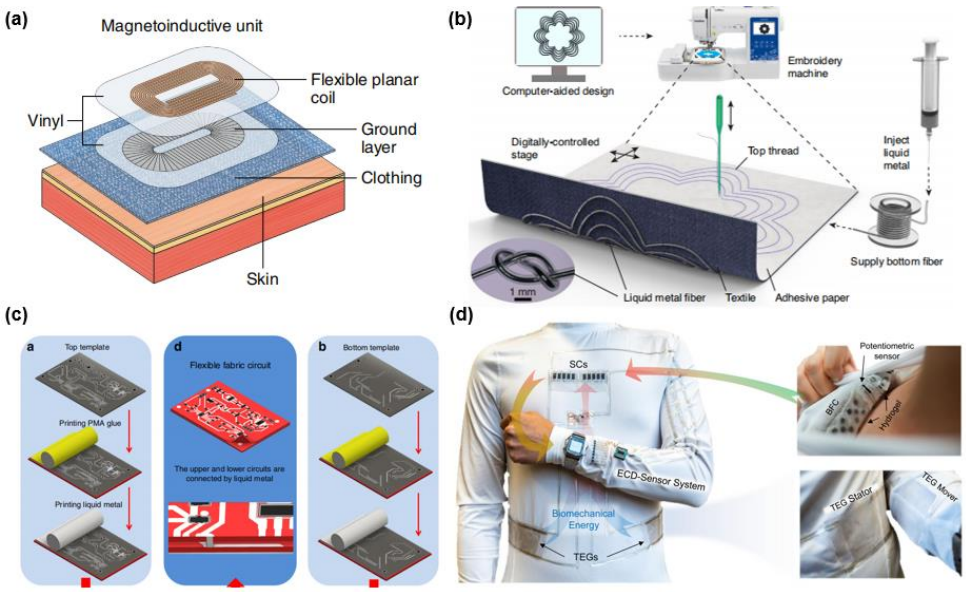

Figure 2. 19 Textile-based electronics employ diverse fabrication techniques to enable wearable functionality. **a** A body area network utilizing metamaterials embedded in textiles for enhanced signal transmission **b** Digital embroidery, where liquid metal fibers—comprising Galinstan-filled perfluoroalkoxy alkane (PFA) tubing—are stitched into fabrics to create conductive pathways. **c** Production of flexible textile circuits through layered printing and lamination processes. **d** Wearable microgrid system, with modular components strategically placed on a shirt for optimal performance and user comfort(*64, 67, 142, 143*).

Hybrid textile-based electronics employ diverse fabrication techniques to integrate functional components into fabrics. One approach involves embedding conductive tracks into garments using heat-activated vinyl adhesives, enabling near-field communication (NFC) with enhanced signal propagation (Figure 2.19a). Alternatively, digital embroidery enables the precise patterning of liquid metal fibers (e.g., Galinstan-filled PFA tubing) onto textiles, offering advantages over screen printing by eliminating solvents and preserving fabric integrity (*142*). For flexible circuits, template-based

deposition of liquid metal wires on cotton substrates leverages hydrogen bonding with PMA adhesives, ensuring adhesion without compromising breathability (Figure 2.19b). The liquid metal fiber is prepared by injecting Galinstan into a PFA tube via a syringe(*67*). Another innovation is modular e-textile microgrids, where energy-harvesting and storage components are synergistically embedded into fabrics to power wearable applications autonomously (Figure 2.19c). Applying glue only to the area of the design line can ensure that the final product retains the textile's good breathability(*64*). Figure 2.18d proposes the concept of a wearable electronic textile microgrid system, whose application is powered by energy collectors and related energy storage modules, such as triboelectric nanogenerators (TENGs)(*143*). These methods demonstrate the versatility of textile-compatible manufacturing, striking a balance between functionality and material properties such as flexibility and comfort.

2.2.3 Towards integrated textile-based sensing systems

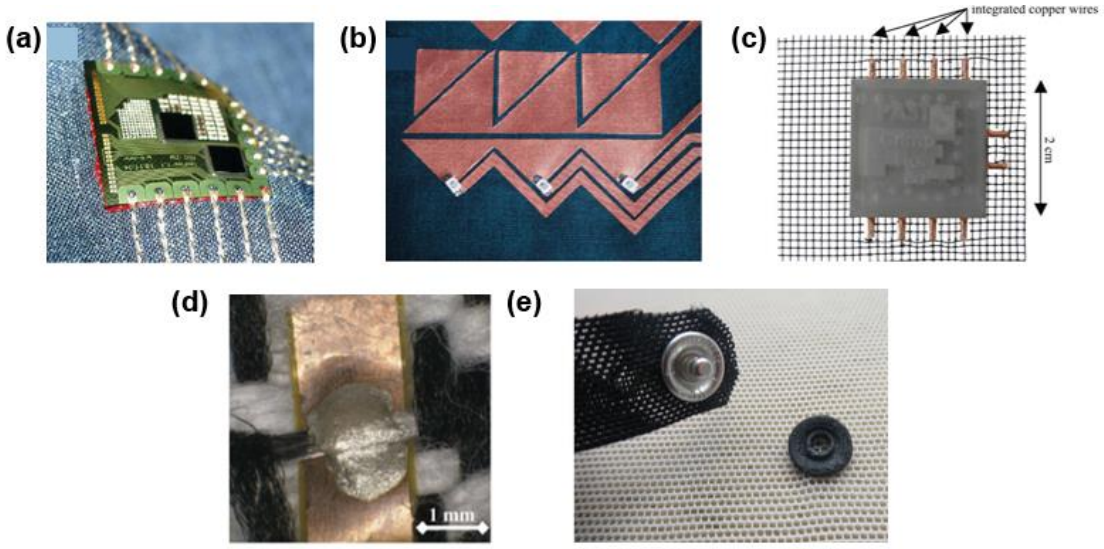

Figure 2. 20 Connectors and joining technologies for electronic textiles. **a** Stitched connection. **b** Soldering and welding. **c** Crimping. **d** Adhesives and **e** connectors(*144*).

Despite intensive research on textile sensors, fabricating electronic circuits on textiles using standard conductive materials (such as tin, copper, and other conductive inks) remains challenging (*144-146*). This is mainly because standard circuits require printed

circuit boards, which are challenging to implement on textiles due to the variations in connections and substrates. In recent years, textile-integrated systems, including biosensors and electronics, have been associated with various conductive materials (e.g., liquid metal, silver nanowires, and copper coils) through textile-embedded forms (*64, 67, 133, 140*). As shown in Figure 2.20, various connectors and joining technologies are selected to connect rigid electronic components and soft textiles, including stitched connections, soldering, welding, crimping, adhesives, and connectors. Stitched connections are challenging to apply when the chips have multiple pins, whereas soldering and welding are detrimental to the textile when the temperature exceeds 200 °C. As a result, commercial epoxy adhesives were selected as connectors for bonding the chips to the textiles.

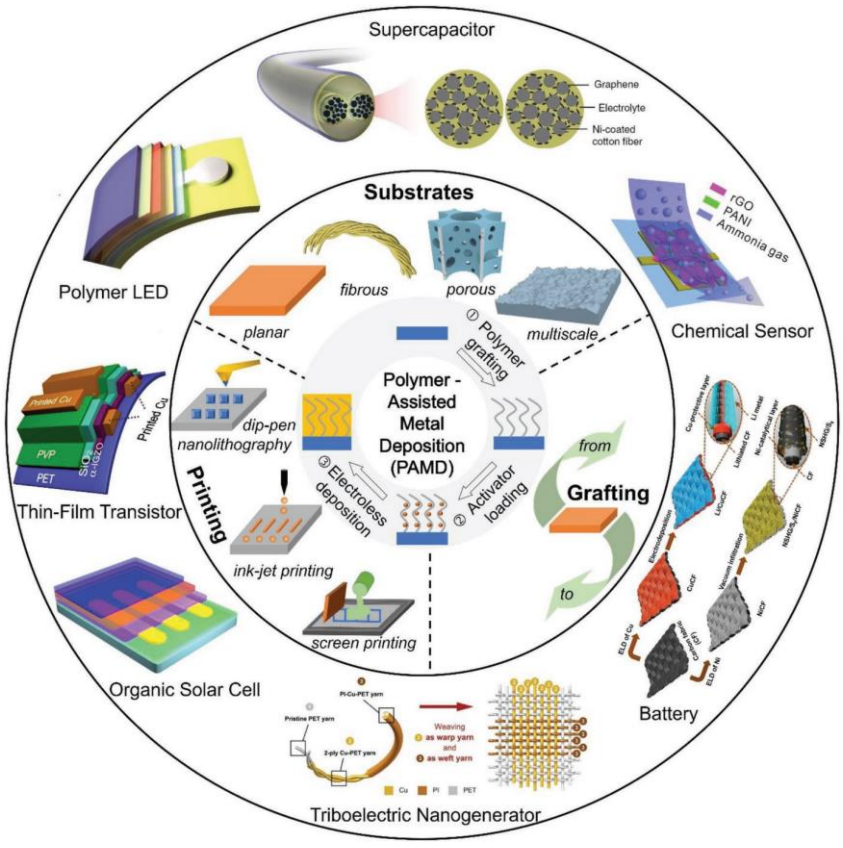

Figure 2. 21 Schematic illustrations of PAMD (*147*).

To address these limitations, we propose developing an electrochemical sensing platform using polymer-assisted metal deposition (PAMD) on polyester (PET) fabric.

This cost-effective, solution-based approach enables large-scale production of highly conductive textiles, with reported conductivities reaching 2×10^7 S m^{-1}(*148, 149*). The resulting metallized fabrics exhibit exceptional mechanical resilience, maintaining functionality under bending, folding, and stretching—critical properties for wearable applications(*150-152*). Our fabrication process employs double-sided photolithography, adapted for textile substrates by using immersion coating to accommodate the porous, three-dimensional structure of woven fabrics.

This technique overcomes challenges posed by the air permeability and complex topography (Figure 2.20). To ensure robust electrical connections, we utilize epoxy-silver adhesive to bond components while preserving textile flexibility(*153, 154*). The method offers rapid, accessible fabrication with potential for system integration. While PAMD-treated textiles demonstrate promising characteristics, their full potential in integrated sensing systems remains underexplored. Future work could combine these textile circuits with miniaturized electronics to create hybrid systems that leverage the strengths of both approaches, particularly when paired with established power and communication solutions.

The interfacial polymer layer is crucial for PAMD and the properties of the metal that it yields. Generally, thicker and denser interfacial polymer with more binding sites of the ELD activators could induce faster deposition and higher electrical conductivity of the metal layer. Therefore, one great effort in the development of PAMD is to study the polymer grafting to meet different application requirements. Over years of study, many chemistries have been reported to graft the polymer in a PAMD process (Figure 2. 22). Polymer-Assisted Metal Deposition (PAMD) is a bottom-up method for directly growing metal layers on flexible substrates. This process involves three key steps: grafting a functional polymer onto a substrate, immobilizing catalytic activators on this polymer, and then depositing metal via electroless deposition (ELD).The interfacial polymer layer is critical, as its properties dictate the quality of the final metal layer. A thicker, denser polymer with more activator binding sites results in faster deposition and higher electrical conductivity. PAMD offers several distinct advantages over traditional "metal ink" strategies:

1.Material Versatility: It enables the deposition of metals like copper and nickel, which are difficult to process with inks, by growing them in a reductive environment that prevents oxidation.

2.High-Quality Films: The resulting metal films are compact and smooth, achieving conductivity close to bulk metal and surface roughness of just a few nanometers, which is ideal for electronics.

3.Excellent Flexibility: An interpenetrating polymer/metal network at the interface creates strong adhesion, allowing for remarkable flexibility with bending radii under 10 μm.

4.Substrate Compatibility: The low-temperature, aqueous ELD process is compatible with various flexible, 3D, and porous substrates.

5.Patternability: PAMD can be integrated with printing techniques to create metal patterns with resolutions from nanometers to micrometers.

Despite its success in creating flexible conductors for sensors, solar cells, and other devices, future development must address key challenges: improving the metal's surface stability against electrochemical impurities, enabling controlled vertical deposition without contamination, deepening the mechanical understanding of the polymer-metal interface, and expanding the range of metals deposited with PAMD. Overcoming these hurdles will unlock further opportunities for high-performance flexible electronics. This method mentions the feasibility of fabric metallization and clarifies the interface bonding mechanism between the polymer brush, fabric fibers, and metal layer, understanding the core reason for “metal patterns withstanding over-time washes”. Theoretical support for material interface stability should be supplemented.

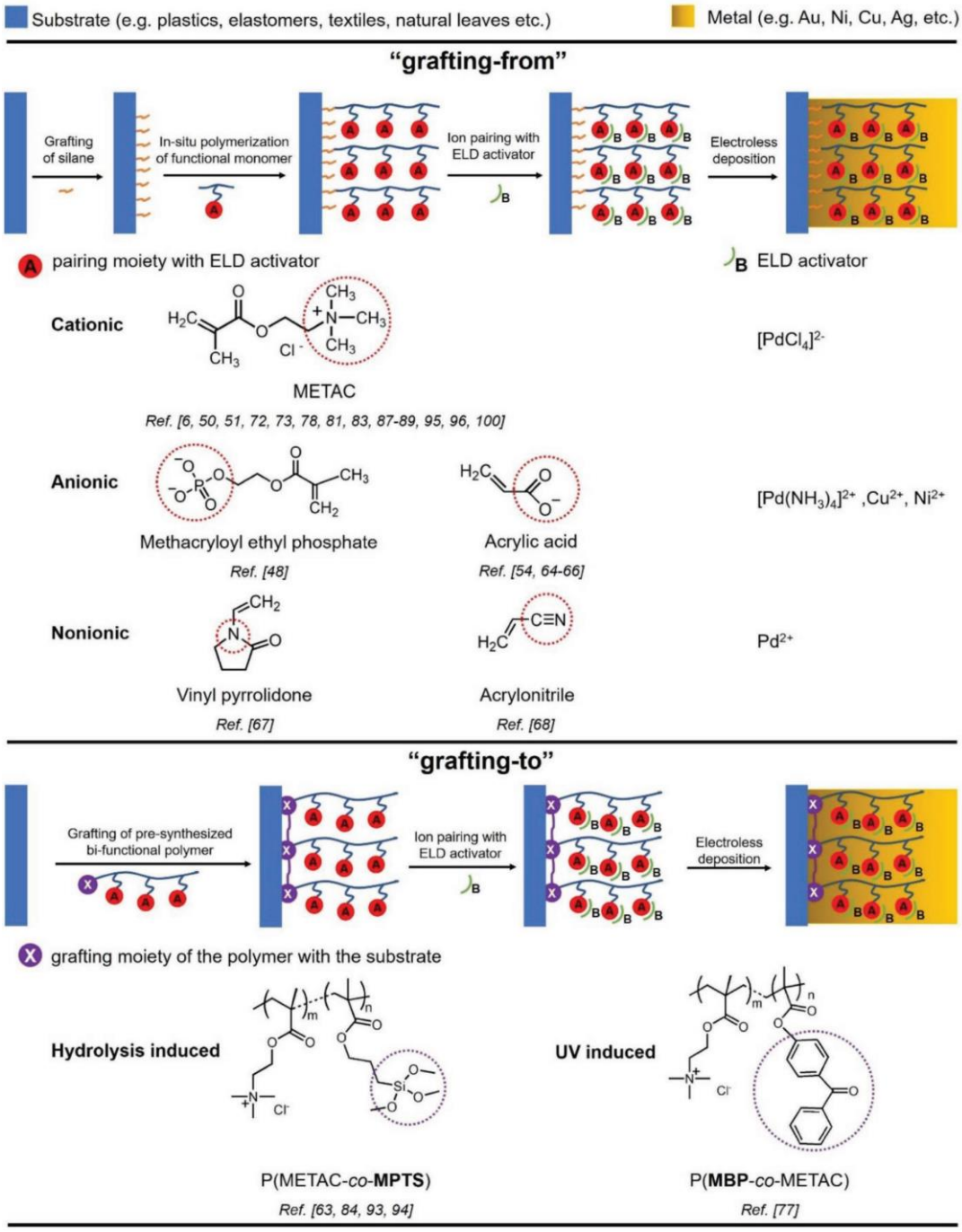

Figure 2. 22 Schematic illustration of "grafting-from" and "grafting-to" strategies developed for grafting the interfacial functional polymer in PAMD and the corresponding representative materials in use. (*147*).

CHAPTER 3: METHODOLOGY

In this chapter, the overarching methodology of this thesis is presented. The fabrication process for textile bioelectronics is described in detail. Additionally, the equipment and techniques employed for characterizing and evaluating the textile bioelectronics are thoroughly explained.

3.1 Materials

All chemicals were used as received unless otherwise specified. Key reagents included hydrogen chloride (HCl), 3,4-ethylene dioxythiophene (EDOT), poly(sodium 4-styrene sulfonate) (NaPSS), potassium hexacyanoferrate(II) trihydrate (K4[Fe(CN)6]), sodium tetrakis[3,5-bis(trifluoromethyl)phenyl]borate (Na-TFPB), bis(2-ethylhexyl) sebacate (DOS), tetrahydrofuran (THF), valinomycin (potassium ionophore), sodium tetraphenylborate (NaTPB), cyclohexanone, PBS (Biosharp BL302A), potassium chloride (KCl), calcium chloride (CaCl2), glucose, sodium hydroxide (NaOH), ethyl alcohol, acetic acid, 3-(trimethoxysilyl)propyl methacrylate (KH570), methacryloxyethyl trimethylammonium chloride (METAC), potassium persulfate (K2S2O8), ammonium tetrachloropalladate(II), potassium sodium tartrate, copper sulfate pentahydrate, formaldehyde solution, and chloroauric acid (HAuCl4), sourced from Sigma-Aldrich. Additional materials, including hydrochloric acid (HCl), high-molecular-weight polyvinyl chloride (PVC), and related solvents, were obtained from J&K Scientific. Potassium ferricyanide (III), silver paste, polyvinyl butyral resin (BUTVAR B-98, PVB), sodium chloride (NaCl), iron(III) chloride (FeCl3), and other reagents were purchased from Aladdin Biochemical Technology.

For biological assays, the Calcein/PI Cell Viability/Cytotoxicity Assay Kit (C2015M) was acquired from Beyotime Biotechnology (China). Conventional-grade male C57BL/6 mice were provided by GEMPHARMATECH (Foshan, China), and Masson's trichrome stain (C0189M) was sourced from Beyotime Biotechnology. Additional supplies, including paraformaldehyde, paraffin, carbon tetrachloride (CCl4), ethanol, pentobarbital sodium, povidone-iodine, and nylon, were commercially obtained.

Deionized water (18.2 MΩ cm) was purified using a Millipore Synergy system for all aqueous solutions.

3.2 Fabrication of Monolithically Integrated Systems

3.2.1 Fabrication of metallic textile

The polymer-assisted metal deposition (PAMD) process was employed to metallize commercial PET fabrics. First, the textile underwent ethanol cleaning followed by alkaline treatment (2 M NaOH, 80 °C, one h) to generate surface hydroxyl groups (Figure 3.1). After thorough DI water rinsing and drying, the substrate was functionalized with KH570 silane (4% v/v in 95% ethanol, 1% acetic acid, and 4% DI water) for 1 hour to enable silanol bonding. Subsequent free-radical polymerization was conducted by immersing the textile in a 20% METAC aqueous solution with K2S2O8 as the initiator (80 °C, 1 h), yielding quaternary ammonium-rich polymer brushes.

Catalytic activation was achieved by immersing the modified textile in (NH4)2PdCl4 solution (4 mM), where $[PdCl_4]^{2-}$ ions bound electrostatically to the poly-METAC chains. After removing unbound catalyst through DI washing, copper deposition was performed using an electroless plating bath comprising two components: (A) an alkaline copper-tartrate complex (12 g/L NaOH, 13 g/L $CuSO_4 \cdot 5H_2O$, 29 g/L $KNaC_4H_4O_6$) and (B) formaldehyde reductant (45 mL/L). The resulting Cu-PET fabric exhibited uniform metal coating (Figure 3.1), with the PAMD process creating a robust metal/polymer interfacial layer that enhanced adhesion stability. Key advantages included the formation of a composite structure at the fiber-metal interface, which enhanced mechanical durability while maintaining textile flexibility(*148, 155, 156*).

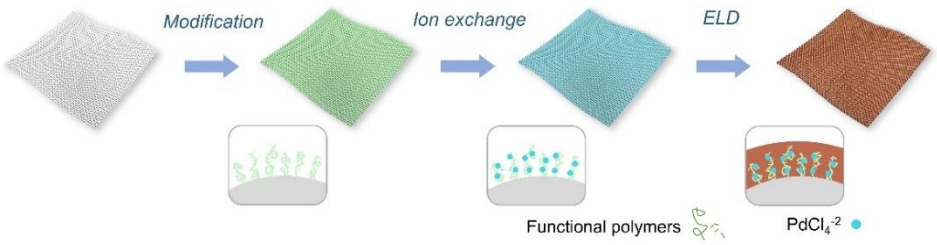

Figure 3. 1 Schematic diagram of the PAMD process.

3.2.2 Fabrication of metallic pattern on textile

The electrode and circuit fabrication process employs a dual-sided photolithographic approach on metallized textiles. First, the conductive textile substrate is uniformly coated with NR9-1500p photoresist (Futurrex, USA) through immersion coating, followed by thermal curing at 110°C for 6 minutes. Pattern definition is achieved through simultaneous UV exposure (1 minute) of both textile surfaces using aligned photomasks, with post-exposure baking at 110°C for 5 minutes to complete the photochemical reaction. The developed patterns are then revealed by removing unexposed resist areas using an RD6 developer solution (Futurrex, USA). Afterward, non-patterned metal regions are selectively etched with a 0.5 M ferric chloride solution. The remaining photoresist is stripped using acetone, yielding precisely defined conductive pathways. The completed textile circuits undergo final cleaning with ethanol and DI water before air drying (Figure 3.2), resulting in flexible electronic structures suitable for subsequent integration.

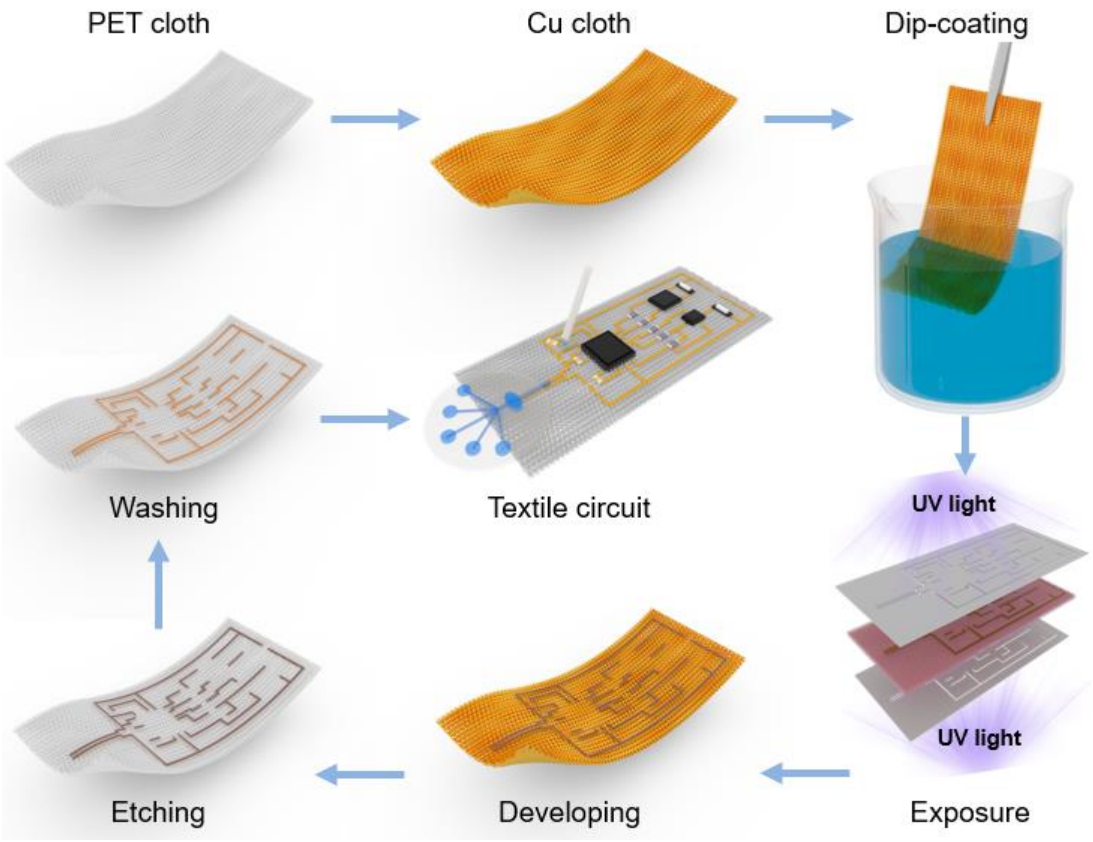

Figure 3. 2 The fabrication of double-sided photolithography for textile sensing systems.

3.2.3 Fabrication of sensor electrodes

The sensing platform employed a two-electrode system utilizing gold-coated copper (Au@Cu) electrodes for both working and reference components. Reference electrodes were prepared through sequential processing: silver was first electrodeposited on Au@Cu substrates (1 mA/cm², 30 min) followed by chlorination in 0.1 M $FeCl_3$ (60 s), with subsequent application of a polyvinyl butyral (PVB) membrane formed from a methanol solution containing 79.1 mg/mL PVB and 50 mg/mL NaCl.

For pH sensing, polyaniline (PANI) was electrochemically deposited on working electrodes using cyclic voltammetry (0.9 V amplitude, 1 Hz, 10% duty cycle, 1200 cycles) in 0.1 M aniline/1 M HCl electrolyte. Ion-selective electrodes incorporated a PEDOT: PSS interfacial layer, synthesized via constant-current polymerization (2

mA/cm², 20 mC) of 0.01 M EDOT/0.1 M NaPSS, to enhance charge transfer kinetics. Ion-selective membranes were solution-cast with optimized compositions:

- Sodium-selective: Na ionophore X (1 mg), NaTFPB (0.55 mg), PVC (33 mg), DOS (65.45 mg) in THF
- Potassium-selective: Valinomycin (2 mg), NaTPB (0.5 mg), PVC (32.75 mg), DOS (64.75 mg) in cyclohexanone

Before functionalization, electrodes underwent ultrasonic cleaning (5 min) and electrochemical pretreatment (cyclic scanning in 0.5 M H_2SO_4, -0.2 to 1.3 V, 4 V/s). Aptamer sensors were prepared through thiol-gold chemistry, involving disulfide reduction with TCEP (1 hour), surface immobilization (1 µM aptamer, 4°C, 1 hour), and passivation with C6-OH (2 mM, 6 hours). Sensor performance was evaluated in physiological buffers (10 mM phosphate, 100 mM NaCl, pH 7.4) and biological fluid mimics (1:1 mixture of urine and saliva with PBS).

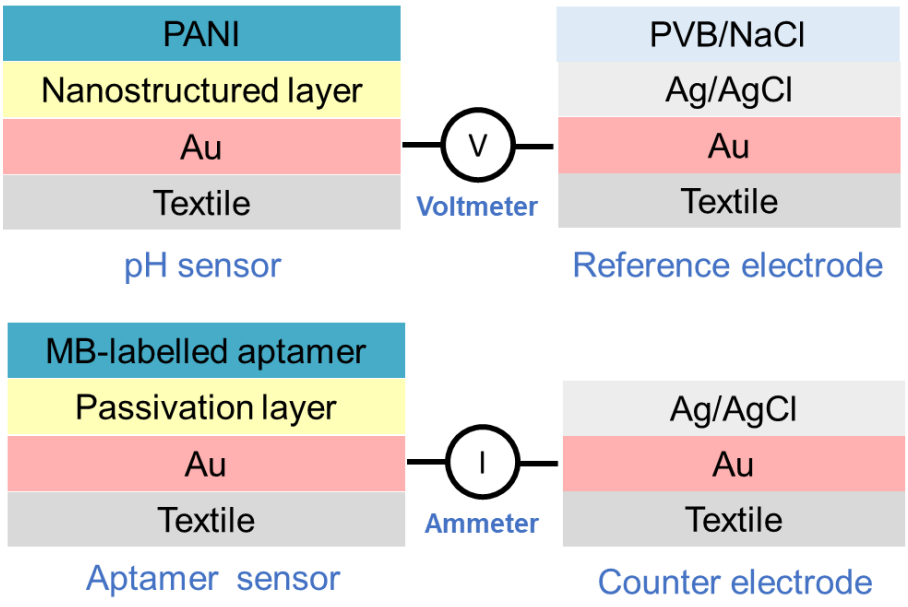

Figure 3. 3 Structure of the electrodes of 2 types of wound sensors. **a** pH sensor. **b** Aptamer sensor.

3.2.4 **Fabrication of the hybrid in-textile wristband**

The system's signal conditioning circuitry incorporated three LMV358 operational amplifiers for low-noise signal amplification, along with an AD5941 electrochemical front-end chip for precise measurement. The processing backbone consisted of an STC8H3K64S2 microcontroller for core operations, supplemented by an ESP32 for wireless connectivity. Bluetooth communication was enabled through CH9141K and FR8003 transceiver modules.

Sensor signals were first conditioned by amplifying the open-circuit potential to millivolt-level outputs, followed by noise reduction via an active low-pass filter. The microcontroller firmware, developed using Keli and Cubeide IDEs, implemented a 12-bit ADC for high-resolution analog-to-digital conversion. The AD5941's integrated DAC generated excitation waveforms, while processed data packets were wirelessly transmitted to mobile devices via the Bluetooth interface. This architecture achieved efficient signal acquisition with optimized power consumption for wearable applications.

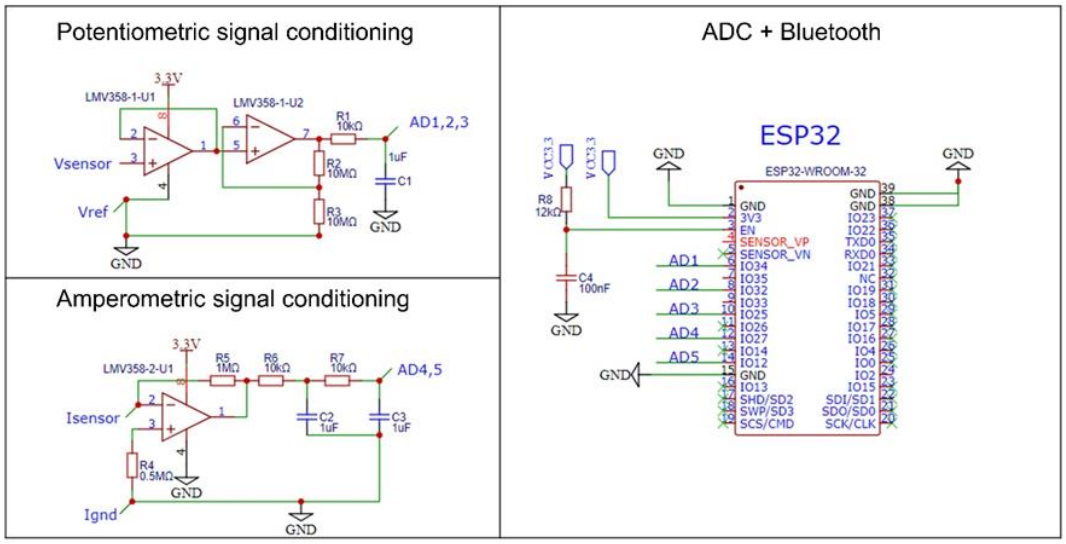

Figure 3. 4 Schematic diagram of signal-conditioning (potentiometric and amperometric) and wireless circuit. (Bluetooth, ADC part).

3.2.5 On-body and real-time epidermal analysis with wireless bioelectronics

A cohort of healthy adults (aged 20-30 years) participated in sweat analysis trials using our wearable sensing platform. The study protocol involved a two-phase exercise regimen while wearing the sensor-integrated wristband, which transmitted data wirelessly to a paired smartphone application. Participants first completed a 30-minute cycling warm-up to induce perspiration, allowing sweat to fill the microfluidic channels naturally. A standardized 30-minute stationary cycling session at constant intensity followed this.

During the exercise period, the mobile application continuously recorded and processed sensor data, displaying real-time potassium concentration trends on the user interface. For validation purposes, sweat samples were collected at 5-minute intervals for parallel analysis by ICP-MS. This dual-measurement approach enabled direct comparison between the wearable sensor outputs and laboratory-grade analytical results, providing robust performance evaluation of the system under dynamic physiological conditions.

3.3 Characterization

The study employed comprehensive analytical techniques to evaluate sensor performance and textile properties. Microstructural analysis was performed using a Hitachi TM3000 scanning electron microscope and a Nikon polarizing microscope, while electrochemical characterization utilized CHI760e and Ivium Soft 4 workstations. Elemental quantification in sweat samples was verified through ICP-MS (Thermo Q Exactive). Textile properties were rigorously assessed according to standardized methods: air permeability (ASTM D737-08, SDL MO21S tester), moisture permeability (ASTM E96/E96M-13 cup method), and mechanical properties (Instron 5599 universal testing system). Electrical characterization under strain conditions was conducted using a Keithley 2400 source meter coupled with a programmable stretching apparatus.

For physiological validation, participants (aged 20-30 years) wore either a headband or a wristband sensor during controlled exercise protocols. Following a 20-minute warm-up on stationary bicycles, subjects completed 30 minutes of standardized cycling, during which the system wirelessly transmitted data via Bluetooth to a dedicated smartphone application. Sweat samples were collected at 400-second intervals (0-1600s) from forehead microtubes for comparative analysis using a pH meter, ICP-MS, and HPLC. All samples were preserved at -4°C before laboratory analysis, with the collection sites cleaned between samplings. This protocol enabled simultaneous real-time sensor evaluation and reference measurements under physiologically relevant conditions.

CHAPTER 4: IN-TEXTILE PHOTOLITHOGRAPHY FOR FABRICATING METAL PATTERNS WITHIN TEXTILES

Textile electronics face inherent trade-offs between achieving high-resolution conductive patterns and preserving vital textile properties, such as permeability and flexibility. This work introduces in-textile photolithography, a transformative manufacturing paradigm that combines polymer-assisted metallization (PAMD) with dual-sided UV patterning to embed binder-free, three-dimensional metal networks (Cu, Ag, Ni) directly within the textile bulk. The technique achieves sub-100 μm resolution, surpassing conventional screen printing (>500 μm) and weaving methods, while eliminating planarization layers to retain >95% porosity, breathability (561 g/m²/day moisture vapor transmission, 77.3 mm/s airflow), and mechanical compliance (bending radius <1.5 mm). Metalized traces permeate the textile thickness, enabling dual-sided circuitry and multilayer integration with exceptional stability: resistance changes remain negligible after 10,000 bending cycles and 20 washing cycles. Demonstrated across diverse textiles (polyester, glass-fiber hybrids, and nonwoven PP), the method enables the development of complex e-textile systems, including micro-supercapacitors that exhibit 300% higher areal capacitance (leveraging conformal 3D current collectors) and integrated health-monitoring sensors. This approach resolves the critical precision-permeability-durability trilemma, establishing a scalable platform for advanced, comfortable wearable electronics in healthcare and human-machine interfaces.

4.1 Introduction

Wearable bioelectronic devices have emerged as crucial tools for the epidermal or non-invasive tracking of physiological indicators and chronic biomarkers, which are essential for fitness oversight and daily healthcare management(*3, 4, 17, 157-161*). Over the past two decades, significant progress has been made in flexible electronics using thin-film

substrates fabricated via established nanomanufacturing methods(*93, 162-165*). However, such thin-film devices often exhibit limited breathability and moisture permeability, reducing comfort during prolonged health monitoring. Their smooth surfaces also lack sufficient active sites for applications such as sensing or batteries, where a high surface area is critical for performance(*166*). In contrast, textiles inherently possess tunable 3D porous architectures, enabling superior airflow, moisture regulation, mechanical flexibility, and enhanced surface interactions(*136, 167-171*). These multifunctional textiles, which incorporate sensors, energy harvesters, and wireless modules, can unobtrusively interface with the body and environment, providing unparalleled comfort and enabling real-time health monitoring solutions(*172-176*). A central hurdle in textile electronics is embedding conductive pathways that retain textile properties while ensuring electrical functionality. Conventional strategies include interlacing conductive threads (e.g., metallic yarns, carbon nanotube fibers) into textiles or printing conductive pastes onto surfaces(*177-183*).

The key challenge lies in embedding conductive patterns into textiles without sacrificing permeability, softness, or durability. Existing methods involve weaving conductive yarns (e.g., silver-coated fibers, carbon nanotube threads) or printing conductive inks onto textiles(*184-188*). While textile patterning methods preserve the inherent flexibility and breathability of fabrics, their capacity to produce complex circuits is limited by incompatibility with conventional electronics manufacturing processes. In contrast, printed electronics offer a promising alternative, as conductive inks—consisting of functional materials suspended in polymeric binders—are directly deposited onto textile substrates, allowing for the creation of customizable conductive pathways. This method exhibits superior scalability and design flexibility compared to conventional textile integration techniques. (*189-191*). While woven conductive threads maintain flexibility and breathability, they lack compatibility with standard electronics manufacturing processes, which limits the complexity of circuits. Printed conductive layers, though versatile, face issues with ink diffusion on rough textile surfaces, resulting in low-resolution traces (>500 μm), reduced permeability, and stiffened textiles prone to cracking(*192-195*). Planarization layers improve patterning resolution but eliminate

textile porosity, undermining comfort. Current approaches thus fail to unite high conductivity, precision, and textile functionality.

The urgent need for seamless integration of electronic components within textiles using conventional conductors (e.g., Cu, Sn) has driven innovation in scalable manufacturing techniques (*196*). PAMD emerges as a superior method, combining cost efficiency with the high-throughput production of durable, conductive textiles(*148*). Metalized copper fabrics engineered through PAMD demonstrate exceptional electrical conductance (~2.0×10^7 S m^{-1}), approaching the intrinsic conductivity of bulk copper (6.41×10^7 S m^{-1})(*197*). The process generates a hybrid polymer-metal matrix at the interface, enhancing interfacial bonding strength while preserving textile flexibility. Despite these advances, the full potential of PAMD-engineered conductive networks in creating unified sensing architectures remains underexplored, particularly for applications that require the monolithic integration of multifunctional systems within single textile substrates.

To overcome these challenges, we introduce an innovative fabrication technique called embedded textile lithography, which integrates photolithographic patterning with selective metallization to create three-dimensional conductive architectures directly within the fabric structure. This hybrid approach enables the formation of intricate, interconnected circuitry while preserving the textile's native mechanical and comfort properties. This technique allows high-precision metal patterning (sub-100 μm) without the use of binders or planarization, thereby preserving the textile porous structure, breathability, and softness. The metalized patterns permeate the textile thickness, enabling dual-sided circuitry and multilayer integration. These interconnects exhibit exceptional stability, enduring 10,000 bending cycles and 20 washing cycles with negligible changes in resistance. This breakthrough in precision patterning overcomes key limitations in textile electronics, paving the way for highly integrated, permeable, and durable wearable systems for healthcare and human-machine interfaces.

4.2 Experiment

4.2.1 Fabrication of metallic cloth

The metallization process began with commercial polyethylene terephthalate (PET) fabric, which underwent sequential surface modifications to enable electroless metal deposition. Initial preparation steps included solvent cleaning with ethanol and alkaline pretreatment (2 M NaOH, 80°C, 1 h) to generate reactive hydroxyl groups. The hydroxylated substrate was then silanized using γ-methacryloxypropyltrimethoxysilane (4% v/v in ethanol/acetic acid/water) to create polymerizable surface sites. Surface functionalization was continued through thermally initiated (80°C) radical polymerization of [2-(methacryloyloxy)ethyl]trimethylammonium chloride (20% v/v aqueous solution) using potassium persulfate as the initiator, resulting in positively charged polymer brushes. These quaternary ammonium groups served as anchoring sites for palladium catalyst immobilization from a four mM $(NH_4)_2PdCl_4$ solution via ion exchange.

The final metallization step employed an electroless copper plating system consisting of:

- An alkaline copper complex solution (CuSO4·5H2O, NaOH, KNaC4H4O6)
- A formaldehyde-based reducing agent

The resulting copper-coated textiles exhibited uniform conductivity while maintaining fabric flexibility, achieved through the formation of a durable metal-polymer interface at the fiber surface. This PAMD approach enabled the creation of highly conductive textile circuits without compromising the substrate's inherent properties.

4.2.2 Fabrication of metallic electrodes and interconnects on textile

A dual-sided photolithographic method was implemented to construct textile-integrated electrodes and circuitry. Initially, the conductive fabric substrate was uniformly coated with a negative-tone photoresist (NR9-1500p) via immersion, followed by thermal curing at 120°C for 5 minutes to stabilize the polymer layer. Symmetrical UV exposure through aligned photomasks was performed for 60 seconds under collimated light to

transfer the predefined circuit patterns onto both surfaces. A post-exposure bake (120°C, 3 minutes) enhanced crosslinking in UV-irradiated regions, after which unexposed areas were selectively dissolved using an alkaline developer (RD6). The exposed metallic zones were chemically etched via immersion in 1 M ferric chloride solution to isolate conductive traces, followed by stripping residual resist with acetone. Finalized patterned textiles underwent sequential rinses in ethanol and deionized water to remove processing residues, followed by drying in an ambient environment. This optimized protocol enables high-resolution, dual-layer circuit fabrication while preserving textile flexibility and permeability.

4.2.3 Fabrication of micro-supercapacitors

The Fabrication of micro-supercapacitor electrodes employed dual methodologies: mask-based lithographic patterning on textile substrates and stencil-assisted conductive ink deposition. Manganese dioxide (MnO_2) electrodeposition was conducted using an aqueous solution containing 0.1 M manganese acetate, 0.1 M sodium sulfate, and 10 vol.% ethanol as a wetting agent. A pulsed asymmetric voltage profile (1.4 V peak potential, 0.75 V baseline) with a 11% duty cycle and a frequency of 0.11 Hz was applied for 10 minutes to achieve a conformal MnO_2 coating on interdigitated textile current collectors. The solid-state electrolyte formulation consisted of polyvinyl alcohol (11 g) and a 85% aqueous solution of lithium acetate (11 g) dissolved in 120 mL of deionized water, stirred continuously at 80°C, followed by ambient-temperature gelation before precise application over the active electrode regions.

Morphological analysis of the textile architecture revealed bicomponent elliptical geometries, with warp yarns exhibiting primary/minor axis ratios of 3:1 and weft yarns demonstrating 2.5:1 dimensional proportion. Each elliptical conductive strand is integrated with twelve hemicylindrical microfilaments (radius ≈ approximately 50 μm), arranged in a periodic array across the polyester-dominated (approximately 98%) textile matrix. The effective surface area enhancement was computationally modeled using geometric superposition principles, which account for the hierarchical organization of conductive microstructures within the heterogeneous textile framework. This structural

optimization facilitated enhanced interfacial charge storage while maintaining the mechanical compliance characteristic of textile-based energy storage systems:

$$Ratio = \left(\frac{\mathrm{Lwarp}\times\frac{\pi}{2}}{\mathrm{L}} + \frac{\mathrm{Lwarp}\times\frac{\pi}{2}}{\mathrm{L}}\right) \times 0.98 = \left(\frac{(\pi+2\times2)\frac{\pi}{2}}{2\times3} + \frac{(\pi+2\times3)\frac{\pi}{2}}{2\times4}\right) \times 0.98 = 3.72 \qquad (2)$$

where *L* is the length of the cross section for one chosen yarn, *Lwarp* and *Lweft* are the parameters of chosen yarn, 0.98 is the cover factor.

4.2.4 Characterization

Microstructural analysis was conducted using a Nikon Eclipse Ni-U inverted microscope for optical imaging, complemented by high-resolution morphological assessment via a TESCAN MAIA3 field-emission scanning electron microscope. The mechanical robustness of metalized textile traces was quantified through uniaxial tensile testing (Instron 5566, using the ASTM D5035 protocol). At the same time, electromechanical stability under dynamic bending was evaluated using a Keithley 2400 Source Meter synchronized with programmable linear actuators (strain rates: 0.1–5 mm/s). Permeability metrics were systematically characterized under controlled ambient conditions (26°C, 65% RH). Airflow resistance was measured under ASTM D737-08 standards using an SDL MO21S differential pressure system, while moisture vapor transmission rates (MVTR) were determined through gravimetric analysis of water loss in sealed test chambers (ASTM E96/E96M-13). Durability against laundering was assessed through accelerated wash cycles (AATCC 135, 40°C, 50 rpm) in a Whirlpool WTW4955H industrial washer with nonionic detergent.

4.3 Results and Discussion

4.3.1 In-textile photolithography of conductive metal patterns in textiles

Figure 4.1 delineates a two-stage process for creating precision metallic architectures within textile substrates: (i) polymer-mediated metallization and (ii) dual-side photolithographic patterning. Initially, the textile undergoes polymer-assisted metal deposition (PAMD) to establish a conformal conductive layer across its fibrous network. Subsequently, the metalized substrate is immersion-coated with a negative-tone photoresist and subjected to synchronized ultraviolet irradiation from opposing directions. This advanced photolithographic strategy diverges from conventional single-sided exposure techniques typically employed in planar microelectronics. By aligning identical photomasks on both surfaces of the three-dimensional porous matrix, the protocol ensures uniform photochemical crosslinking throughout the textile's depth. Such bidirectional irradiation addresses the optical scattering challenges inherent in fibrous media, enabling faithful replication of micron-scale patterns across the textile's z-axis. The dual-exposure mechanism facilitates comprehensive photoresist modification on individual fibers within the textile's interwoven hierarchy. This critical innovation addresses the limitations of traditional single-plane lithography, which often results in incomplete pattern transfer due to shadowing effects in non-planar geometries. Following exposure, the meticulous development of the resist in a selective manner, coupled with the subsequent etching process, yields conductive traces that are geometrically precise and elegantly delineated. Simultaneously, this procedure ensures the substrate retains its inherent mechanical compliance, a quintessential attribute indispensable for the burgeoning field of wearable electronics.

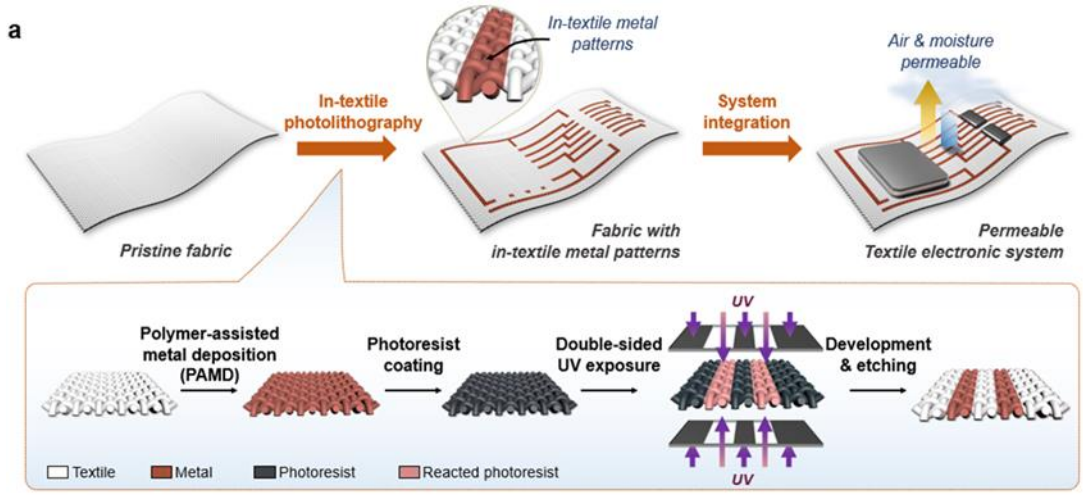

Figure 4. 1 Schematic illustration of in-textile photolithography.

Following bidirectional UV irradiation, the photolithographic sequence progressed through alkaline development, which dissolved the unexposed resist regions, allowing for the selective etching of underlying metallic layers (Figure 4.2). UV-polymerized resist domains functioned as protective barriers during chemical etching, preserving predetermined conductive pathways. Subsequent resist stripping revealed high-fidelity metallic architectures embedded within the textile matrix. This subtractive patterning methodology facilitates scalable production of complex circuitry across meter-scale textile substrates. A 7×10 cm polyester-integrated circuit exhibited geometrically defined Cu traces (300 μm to 2 mm linewidths) while maintaining textile drape characteristics. Microstructural analysis via SEM confirmed localized metallization restricted to individual fiber surfaces within patterned zones, avoiding interfilamentous bonding that typically compromises textile flexibility. Crucially, the processed textile retained its native mechanical and transport properties. Comparative vapor permeability tests demonstrated a deviation of less than 5% from untreated substrates.

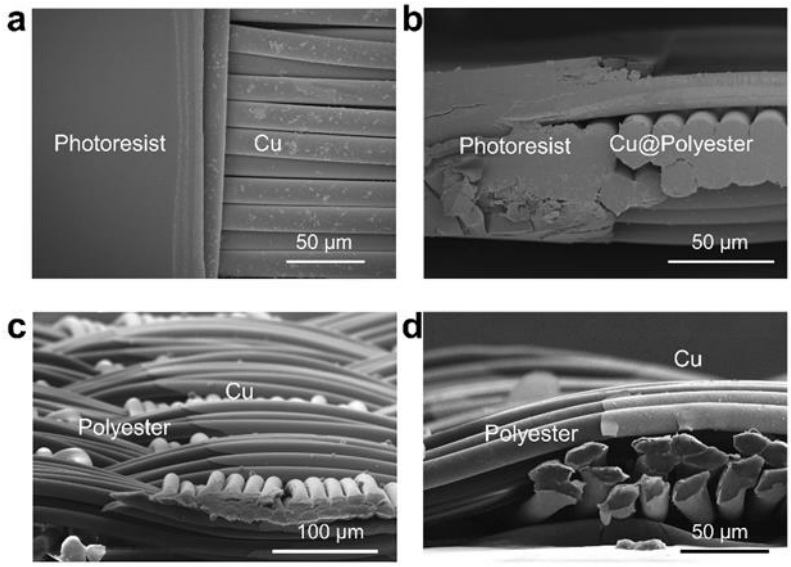

Figure 4. 2 SEM images of Cu patterned PET fabrics. **a-b** SEM image of the photoresist-coated Cu-PET textile after the developing process. **c-d** Images showing the boundary of the Cu in PET fabrics after the etching process.

To validate the broad applicability of the in-textile photolithographic technique, functional conductive architectures were engineered across heterogeneous textile systems: silver (Ag) interconnects and nickel (Ni) interdigitated electrodes (100 μm linewidth resolution) in polyester textiles, copper (Cu) sensing arrays within glass-fiber/cotton hybrids, and Ni electrode networks in polypropylene nonwoven substrates. (Figure 4.3). This cross-material Fabrication achieved sub-200 μm feature consistency while retaining textile flexibility (bending radius < 1.5 mm) and porosity (> 90% of that of untreated textiles). The successful replication of intricate geometries in noble metals (Ag), transition metals (Ni, Cu), and varied textile matrices (woven, composite, nonwoven) underscores the method capacity as a generalized platform for e-textile manufacturing. Notably, energy-dispersive spectroscopy confirmed metal localization to fiber surfaces (<5 μm depth), preserving inter yarn mobility critical for textile drape (Figure 4.4) Such precision enables concurrent integration of signal transmission pathways (Ag), energy storage components (Ni interdigitated arrays), and biochemical

sensors (Cu) within a single textile system, meeting stringent resolution requirements for wearable microelectronics. This substrate-independent approach bridges the gap between conventional micro-fabrication and textile-compatible processes, offering a scalable route to multifunctional e-textiles that maintain inherent breathability and mechanical compliance.

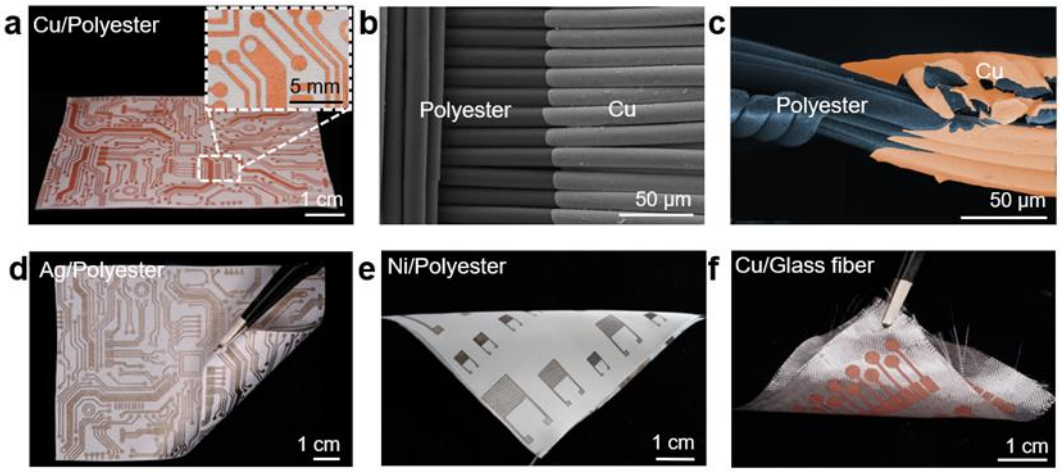

Figure 4. 3 Implementation of in-textile photolithography for creating metallic circuit architectures on fabric substrates. **a** Macroscopic view of a copper-based printed circuit board (PCB) design patterned onto polyester textile. **b&c** High-resolution scanning electron microscopy reveals the precise interface between deposited copper traces and textile fibers in both planar and cross-sectional orientations. **d&e** The technique's material versatility is evidenced by silver PCB patterns on polyester and nickel interdigitated electrodes with varying feature sizes. **f** Adaptation of this approach to glass-fiber textiles.

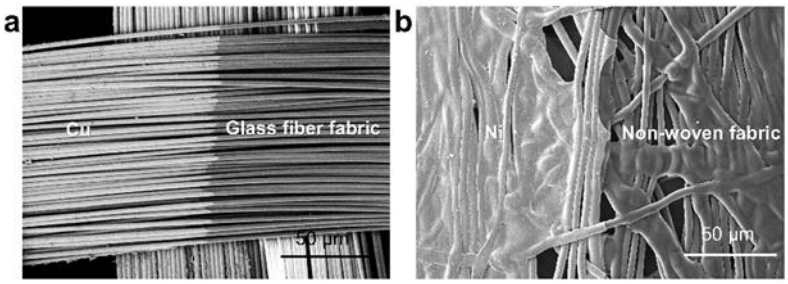

Figure 4. 4 SEM images of Cu lines in different textiles. **a** Cu pattern on glass-fiber textile. **b** Ni pattern on non-woven textile.

4.3.2 Permeable, robust and sub-100 µm conductive metal patterns in textiles

The in-textile photolithographic approach demonstrates superior performance metrics compared to established textile patterning techniques, particularly in breathability retention, mechanical resilience, feature definition, and conductive pathway stability. This enhancement stems from the three-dimensional distribution of metallic networks within the textile matrix and their nanoscale conformal encapsulation of individual filaments (Figure 4.5), which is enabled by the polymer-assisted metallization protocol (PAMD). Unlike surface-applied conductive coatings, this strategy ensures the preservation of the native fibrous architecture, thereby maintaining interconnected micro-voids that are critical for unrestricted gaseous exchange.

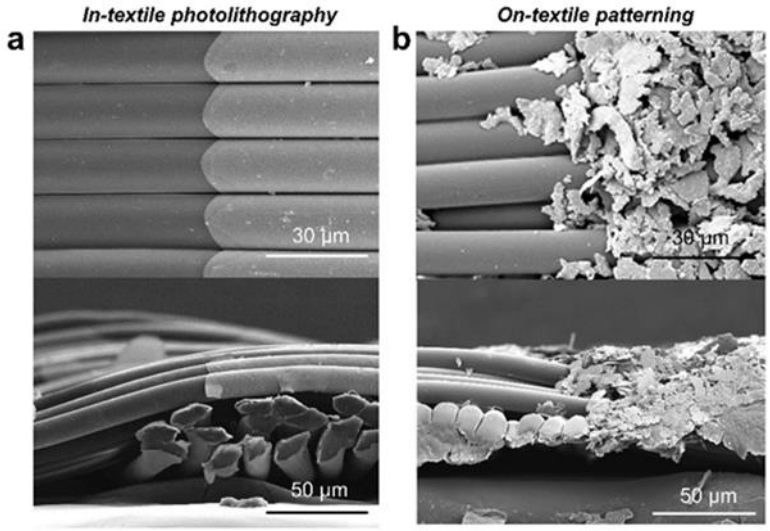

Figure 4. 5 Cu patterns on Polyester$_{0.94}$ made by different patterning methods. **a** Metal-textile boundary by in-textile photolithography. **b** Metal-textile boundary by an on-textile patterning method.

In contrast, conventional non-textile patterning techniques—such as screen printing, as demonstrated in this study—rely on surface deposition of conductive inks, which diffuse into the textile matrix and coat fiber bundles within printed regions (Figure 4.6). This infiltration leads to pore occlusion, which increases fabric rigidity and reduces breathability. The resulting conductive layers exhibit restricted air and moisture permeability, as well as diminished mechanical flexibility, compared to embedded metallization approaches.

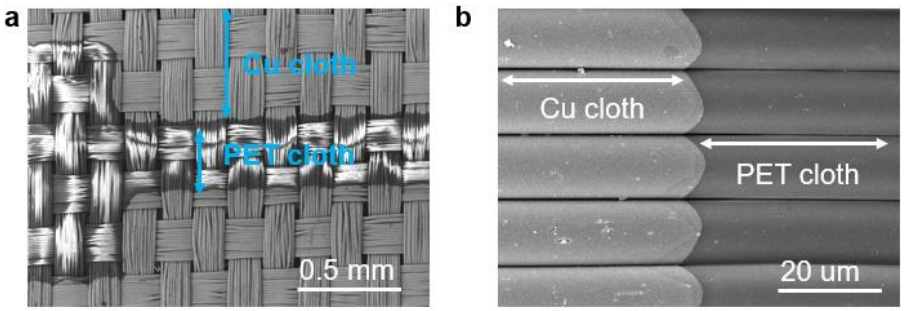

Figure 4. 6 SEM photos of Cu PET textile. **a** Sensor electrode. **b** Etched Cu cloth.

The in-textile lithographic methodology demonstrated substantial improvements over surface-applied conductive patterning, achieving a 21-fold increase in air permeability (77.3 vs. 3.4 mm/s) and a 10% higher moisture vapor transmission rate (560 g/m²/day) compared to conventional techniques (Figure 4.7a). Electromechanical testing revealed superior interfacial stability under cyclic flexure: embedded conductive traces exhibited minimal normalized resistance drift ($R/R_0 \approx 2$) after 500 bending cycles (4.7 mm radius), stabilizing thereafter, whereas surface-patterned equivalents degraded catastrophically ($R/R_0 > 4$) within 10,000 cycles (Figure 4.7b). This methodology further advanced microfeature resolution, producing 200 μm linewidths with stable conductivity (22 Ω/cm) – surpassing the 300 μm limit of traditional approaches (Figure 4.7c). The enhanced precision stemmed from two synergistic mechanisms: (i) photoresist-

mediated confinement of conductive phases, suppressing lateral diffusion, and (ii) bidirectional UV crosslinking ensuring uniform pattern replication across the textile's depth. Such innovations preserved textile porosity (>95% retention) while enabling micron-scale circuit definition, overcoming the resolution-flexibility trade-off inherent to planar textile electronics. The combined geometric control and structural preservation establish this technique as a transformative advancement for breathable, mechanically compliant e-textiles requiring high-density interconnects.

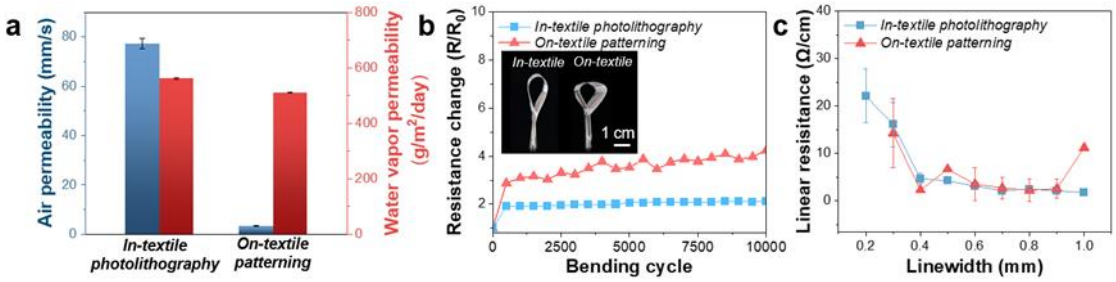

Figure 4. 7 A systematic evaluation of copper-coated textiles reveals distinct performance differences between in-textile photolithography and on-textile patterning methods. **a** Water vapor and air permeability of the textiles coated with Cu fabricated with different patterning methods. **b** Resistance changes (R/R_0) of the Cu patterns fabricated with different patterning methods. **c** Linear resistance of the Cu patterns fabricated with different patterning methods.

A comparative analysis of single versus dual UV exposure protocols revealed fundamental limitations in the fidelity of textile metallization. Opaque textile substrates prevented complete photoresist crosslinking during unilateral exposure, resulting in incomplete polymerization at depth (Figure 4.8a). This incomplete reaction caused developer-induced resist dissolution on unexposed surfaces, exposing the underlying metal to etchant penetration and creating discontinuous conductive pathways. Conversely, bidirectional irradiation enabled full-depth photochemical modification, with cross-sectional analysis confirming the presence of uniform protective barriers surrounding individual fibers (Figure 4.8b). The methodology's efficacy proved thickness-dependent: 100 μm textiles achieved 80 μm UV penetration per side, while

170 μm polyester required dual exposure for full-depth curing. Optimal pattern fidelity was achieved in substrates with thicknesses ≤160 μm, where bidirectional processing enabled 200 μm linewidths at 22 Ω/cm resistivity, surpassing the unilateral exposure's 600 μm resolution limit (25-63 Ω/cm). Electrical characterization demonstrated the superiority of bilateral exposure: features with diameters of 400-1000 μm maintained a linear resistance of 1.7-4.6 Ω/cm, whereas unilateral failure occurred below 600 μm. This performance enhancement stems from three factors: (i) volumetric resist crosslinking preventing etchant infiltration, (ii) elimination of optical shadowing in 3D textiles, and (iii) precise confinement of conductive phases through spatial photopatterning. The technique's depth-resolved curing mechanism enables microelectronic-grade patterning in breathable textiles while preserving <5% permeability reduction versus untreated textiles.

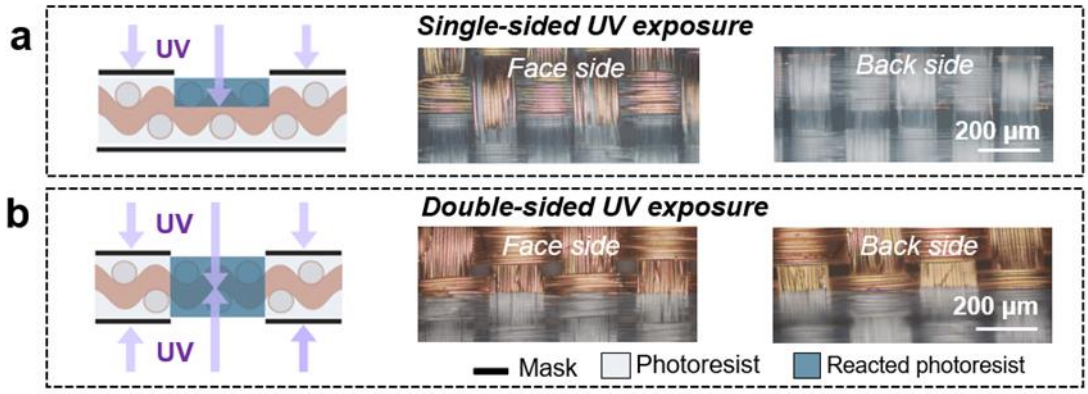

Figure 4. 8 a Schematic illustration of the single-sided UV light exposure in photolithography. **b** Schematic illustration of the double-sided UV light exposure.

The geometric packing density of woven substrates quantified through the textile coverage index (TCI = projected yarn area/total textile area), emerged as a critical determinant of both lithographic precision and electrical functionality in textile-integrated circuits (Figure 4.9). Elevated TCI values (>0.85) corresponded to reduced inter-yarn spacing, creating interconnected microfibril networks that facilitated percolative charge transport across metalized regions. This enhanced conductive continuity enabled reliable current pathways even in ultranarrow traces (≤200 μm

linewidth), overcoming the classical trade-off between miniaturization and conductivity degradation typically observed in sparse textiles (TCI < 0.7).

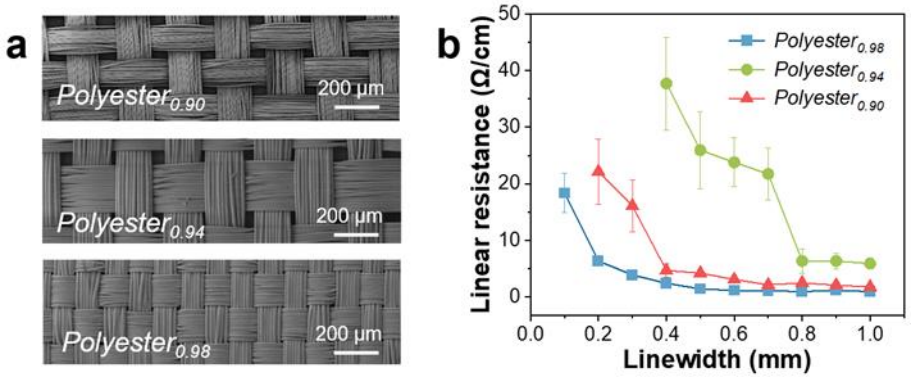

Figure 4. 9 a SEM photos of well-defined metal patterns in different PET textiles. **b** Linear resistance of the Cu PET patterns with different cover factors.

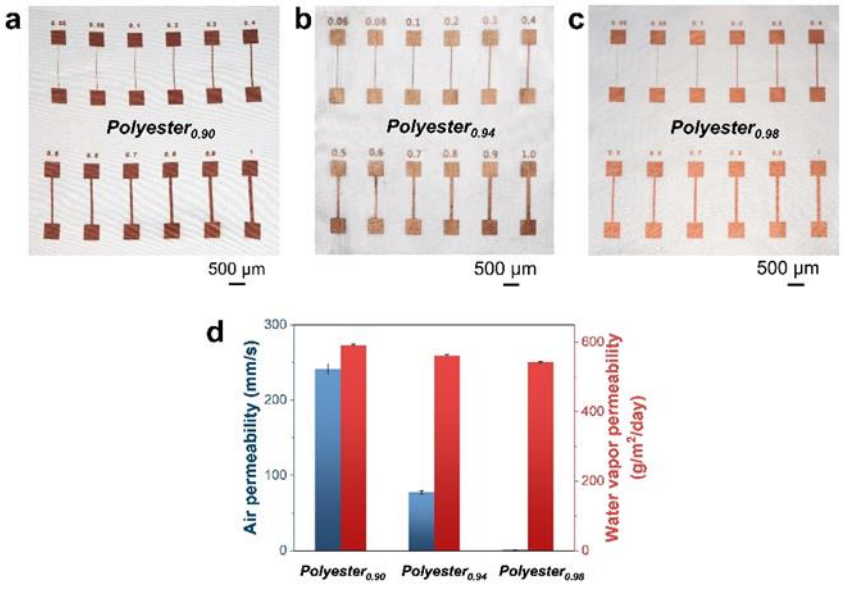

Figure 4. 10 Cu patterns Characterization with different widths. **a-c** Images showing the Cu patterns with different linewidths patterned in $Polyester_{0.90}$ textile, $Polyester_{0.94}$ textile, and $Polyester_{0.98}$ textile. (0.90, 0.94, and 0.98 are the cover factors of the polyester textiles). **d** Air and moisture permeability of the different PET textiles.

The experimental analysis demonstrated that textile coverage density is the predominant factor governing lithographic resolution limits and charge transport efficiency. Metallization processes on woven matrices with 0.94 coverage achieved critical dimensions of 400 μm. In comparison, ultra-dense substrates (0.98 coverage) enabled state-of-the-art linewidths of 100 μm, accompanied by ohmic resistance of 18 Ω/cm and interlacing spacing of 80 μm (Figure 4.10 and Table 4.1). This fourfold enhancement in resolution originates from inter-yarn proximity effects in high-coverage architectures, where compressed microfibril networks establish redundant conductive pathways via three mechanisms: (i) increased surface contact areas between metalized fibers, (ii) reduced current crowding at pattern edges, and (iii) controlled electric field distribution during electrodeposition. Importantly, these microscale advancements were achieved without compromising macroscale permeability, as evidenced by moisture transmission rates of 590 g/m²/day and airflow rates of 240 mm/s – key performance indicators for epidermal-compatible wearables. The methodology's ability to decouple electronic resolution from textile porosity represents a paradigm shift, overcoming longstanding challenges in achieving simultaneous miniaturization and breathability for on-skin microsystems.

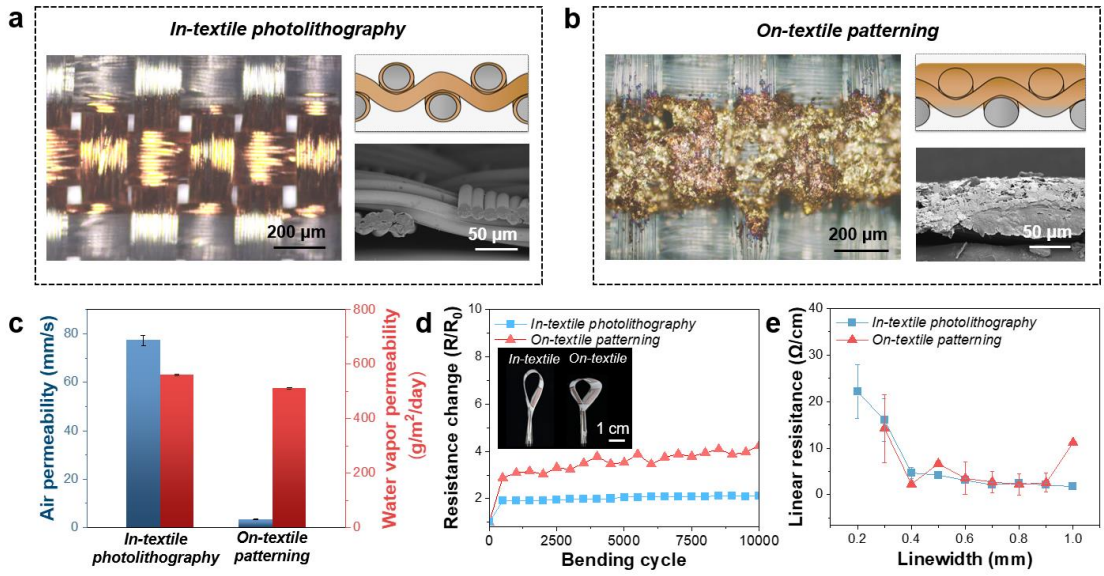

Figure 4. 11 Characterization of well-defined and conductive metal patterns in textiles. **a** Optical image (left), cross-sectional schematic diagram (top right), and SEM image

(bottom right) of the Cu pattern fabricated by the in-textile photolithography method. **b** Optical image (left), cross-sectional schematic diagram (top right), and SEM image (bottom right) of the Cu pattern fabricated by on-textile patterning method (screen printing). **c** Comparison of water vapor and air permeability of the fabrics coated with Cu made by the in-textile photolithography method and the on-textile patterning method. Error bars represent the s.d. of the mean from three fabrics coated with Cu. **d** Comparison of resistance changes (R/R0) of the Cu patterns made by the in-textile photolithography method and on-textile patterning method. Inset is the digital image showing the flexibility of the Cu patterns made by two methods. **e** Linear resistance of the Cu patterns as a function of the patterning resolution. Error bars represent the s.d. of the mean from three Cu patterns.

In-textile photolithography demonstrates clear advantages over standard on-textile patterning techniques across several performance metrics, including breathability, mechanical durability, feature resolution, and electrical performance. The fundamental reason for this lies in the unique composite structure it forms. Utilizing a solution-based metal deposition process (PAMD), this technique creates conductive tracks that permeate the textile scaffold, resulting in a firm and conformal metal coating exclusively around individual fibers (Figure 4.11a). This approach maintains the original configuration of the fiber bundles, safeguarding the fabric's inherent 3D porous network. This preserved structure is vital for maintaining softness and allowing unimpeded air and moisture flow. Furthermore, the composite at the metal-fiber interface, as previously discussed, ensures strong adhesion, drastically improving the pattern's mechanical endurance. Conversely, traditional methods like screen printing, as examined in this study, suffer from ink diffusion that floods the fabric scaffold. This creates a conductive layer that predominantly coats the textile surface and fuses the fiber bundles together within the patterned zone (Figure 4.11b). This fusion critically obstructs the material's pores and increases stiffness, adversely impacting both the fabric's breathability and the flexibility of the electronic patterns.

Quantitative tests confirm these structural differences. Fabrics patterned with the in-textile method showed an air permeability of 77.3 mm/s, which is 21 times greater than

the 3.4 mm/s measured for the on-textile patterned fabric. A 10% improvement in water vapor permeability (561 g/m²/day) was also recorded for the in-textile sample (Figure 4.11c). The mechanical robustness was also superior; when subjected to bending tests, conductive tracks from in-textile photolithography saw their resistance stabilize at approximately twice the initial value (~2 R/R_0) after just 500 cycles. In stark contrast, the resistance of the on-textile patterns escalated to over four times the original value after 10,000 cycles (Figure 4.11d). Finally, in-textile photolithography provides a significant leap in patterning fidelity. It retains the high precision of its namesake, producing circuits with sharp, well-defined edges. The conventional approach was limited to a minimum linewidth of 300 μm, but the in-textile technique reliably fabricated finer lines down to 200 μm while maintaining a low sheet resistance of 22 Ω/cm (Figure 4.11e). This enhanced resolution is a direct result of the photoresist barrier, which curbs the uncontrolled diffusion of the conductive coating, combined with the process's double-sided UV exposure mechanism.

Materials	Patterning techniques	Resolution	Resistance	Process rate	Cost	Yield	Ref.
CNT/PU	Screen printing	1.5 cm	0.2 kΩ/sq	6 hours	Low	-	(*198*)
CNT@Silk	Stitching	-	310 S/cm	1.5 hours	Medium	1 cm/ min	(*199*)
Ag/AgCl/TPU	Screen printing	1 mm	5,000 S/cm	Seconds to hours	-	-	(*200*)
Ag flake	Screen printing	500 μm	1,333 S/cm	12 hours	Low	180 mm /min	(*162*)
Plated Cu	Electroless plating	2.5 mm	0.5 Ω/sq	Minutes to hours	Medium	-	(*201*)
Ag flake/TPU	Screen printing	1 mm	4.31×10^4 S/cm	-	Low	79 threads/ cm	(*202*)
Liquid metal	Embroidery	635 μm	4.2 Ω/m	Low	High	5 mm/s	(*67*)
AgNW/TPU	Laser scribing	135 μm	5,030 S/cm	Low	Medium	-	(*203*)
Cu	In-textile photolithography	100 μm	1.7 Ω/cm	Minutes to hours	High	1000 cm^2/h	This work

CNT: carbon nanotube; PU: polyurethane; AgNW: silver nanowire; TPU: thermoplastic polyurethane.

Table 4.1 Comparison of the resolution and conductivity of different metal patterns reported in the literature.

4.3.3 High-performance bioelectronics enabled by Cu patterns in textiles

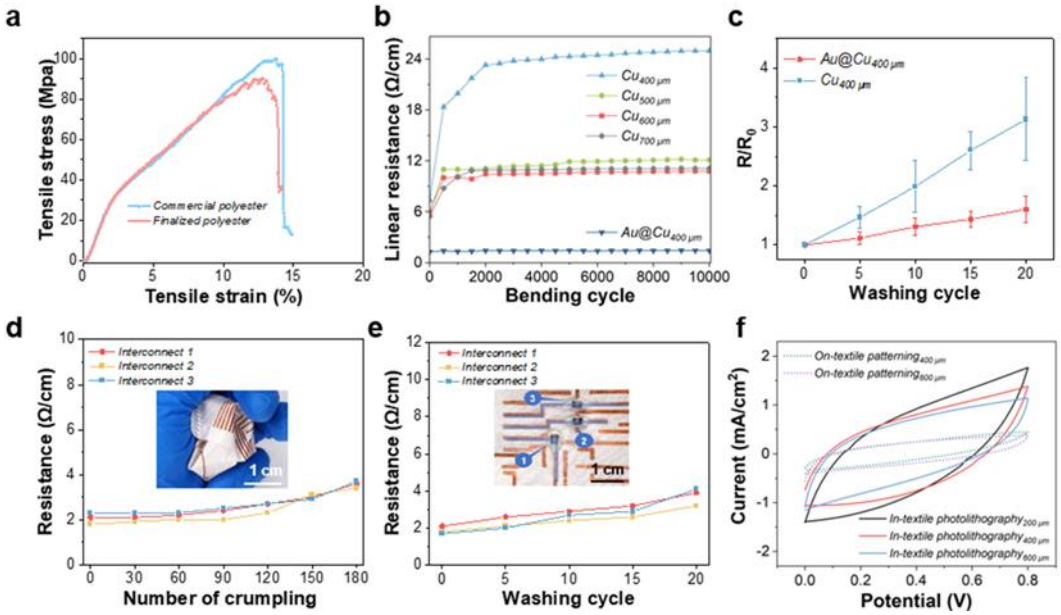

Figure 4. 12. High-performance supercapacitor enabled by in-textile lithography. **a** Mechanical testing revealed minimal alteration in tensile properties between pristine and metallized polyester fabrics. **b** Electrical durability assessments demonstrated stable conductivity of copper traces during extended bending (10,000 cycles, 4.4 mm radius), with linewidth-dependent resistance variations. **c** Washability tests showed gold-deposited interconnects exhibited superior stability (<20% resistance change after 20 cycles) compared to non-treated counterparts. **d** The metallized textiles also endured severe mechanical deformation, showing <15% resistance variation after 180 crumpling cycles. **e** Resistance upon 20 washing cycles. **f** Electrochemical characterization of nickel interdigital electrodes revealed linewidth-dependent capacitive behavior when coated with MnO_2 active material.

The textile-integrated lithographic technique enables the fabrication of multiscale metallic networks within woven matrices, demonstrating critical durability for wearable implementations. Mechanical characterization revealed only an 11% reduction in ultimate tensile strain compared to untreated textiles (Figure 4.12a), confirming the structural preservation. Cyclic flexural testing (10,000 cycles, 4 mm radius) on 400–700 μm Cu traces exhibited initial resistance increases (1,000–2,000 cycles) due to microfibril reorientation, followed by ohmic stabilization through microstructural relaxation (Figure 4.12b). Laundering tests demonstrated exceptional wash fastness, with only a 2-fold resistance elevation after 20 cycles, despite the presence of hydrodynamic shear stresses (Figure 4.12c). Performance was significantly enhanced by employing noble metal cladding, specifically Au-overcoated traces, which ensured consistent baseline conductivity after 10,000 bending cycles and 20 washing cycles. System-level robustness was validated through elastomer encapsulation, which reduced interconnect resistance drift by 50% post-laundering and limited fluctuations to 11% during 120 crumpling cycles (Figure 4.12d and e). This multifunctional durability arises from three mechanisms: (i) depth-localized metallization preventing yarn embrittlement, (ii) interfacial alloying at Au-Cu junctions mitigating oxidative degradation, and (iii) viscoelastic stress dissipation through textile-encapsulant composites.

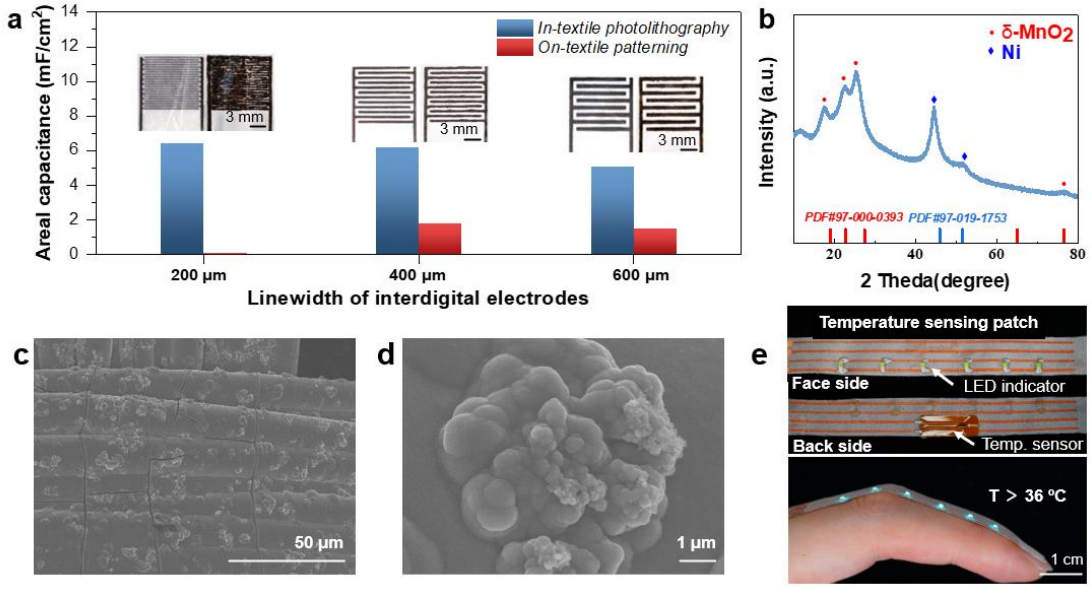

Figure 4. 13 a Electrochemical analysis revealed that the areal capacitance of micro-supercapacitors exhibited a clear dependence on electrode linewidth, with finer features demonstrating enhanced charge storage capacity. **b** Structural characterization through XRD confirmed the successful integration of MnO_2 with nickel interdigital electrodes, showing characteristic diffraction peaks of the composite material. **c-d** Microscopic evaluation via SEM revealed a homogeneous MnO_2 coating with porous morphology, providing high surface area for electrochemical reactions. **e** The practical application of this technology was demonstrated through a fully functional, double-sided temperature monitoring patch featuring precision-patterned copper circuits on polyester fabric.

The in-textile photolithographic technique establishes three-dimensional distributed conductive networks within textile matrices, serving as foundational elements for miniaturized wearable devices. As demonstrated through micro-supercapacitor development, this method surpasses surface-limited approaches (e.g., screen printing's 400 μm resolution barrier) by fabricating 200 μm comb-shaped current collectors with matched interelectrode spacing, eliminating electrical cross-talk while retaining 92% substrate porosity (Figure 4.12f). Geometric modeling revealed a 3.7-fold increase in electroactive surface area relative to planar counterparts, attributable to conformal metal deposition along individual fibers rather than superficial coating. This structural advantage enabled enhanced MnO_2 nucleation during electrodeposition, resulting in energy storage devices with 300% greater areal capacitance than their screen-printed equivalents under matched synthesis parameters (Figure 4.13a-d). The methodology's through-thickness conductivity further permits bidirectional circuit integration within monolithic textile layers, exemplified by a dual-surface thermal monitoring system: resistive sensors on the dorsal surface enabled epidermal temperature acquisition. At the same time, ventral LED arrays triggered optoelectronic alerts when the temperature exceeded 36°C thresholds (Figure 4.13e).

4.4 Conclusions

In-textile photolithography represents a transformative advancement for textile electronics, overcoming longstanding limitations in integrating high-precision, durable conductive pathways without compromising the inherent properties of textiles. By synergizing polymer-assisted metallization (PAMD) with dual-sided photolithography, this technique embeds 3D interconnected metal networks (e.g., Cu, Ag, Ni) directly within the textile bulk, achieving sub-100 μm resolution—unattainable with conventional methods such as screen printing or conductive yarn weaving. Crucially, the technique eliminates binders and planarization layers, preserving >95% of the textile's porosity, breathability (561 g/m²/day moisture transmission, 77.3 mm/s airflow), and mechanical flexibility (bending radius <1.5 mm). Metalized patterns permeate the textile thickness, enabling dual-sided circuitry and multilayer integration while exhibiting exceptional stability, with resistance changes remaining negligible after 10,000 bending cycles (4.4 mm radius) and 20 laundering cycles. The technique's versatility is demonstrated across diverse textiles (polyester, polypropylene, glass-fiber hybrids) and applications, including micro-supercapacitors with 300% enhanced areal capacitance (leveraging 3.7× surface area amplification) and dual-sided wearable sensors for real-time health monitoring. This innovative methodology successfully bridges the gap between microscopic precision and textile functionality, enabling the development of sophisticated electronic textiles that combine superior comfort with robust durability. The technology demonstrates particular promise for next-generation medical monitoring systems and intuitive human-machine interfaces, meeting stringent performance requirements for real-world applications. Furthermore, the fabrication process establishes a production-compatible framework that seamlessly integrates with conventional electronics manufacturing protocols, facilitating scalable industrial implementation.

CHAPTER 5: IN-TEXTILE SYSTEMS FOR MULTIPLEXED SWEAT BIOSENSING

This study presents a monolithically integrated textile-based platform for multiplexed, continuous monitoring of sweat biomarkers. The system was fabricated directly onto conformally metalized polyester (PET) cloth via a modified photolithographic process, enabling precise patterning of conductive interconnects (line width = 1 mm) while preserving substrate permeability. The platform incorporates potentiometric sensors (K^+, Na^+, pH) and amperometric biosensors (glucose, lactate) with nanostructured electrodes (e.g., dendritic Au on Cu) to enhance sensitivity. A PEDOT: PSS ion-to-electron transducer minimized potentiometric drift (2.88 mV/h at 1 mM K^+). Microfluidic channels facilitated continuous sweat sampling, and porous Ecoflex encapsulation maintained mechanical robustness (>3000 bending cycles). Custom signal-conditioning circuitry interfaced with a BLE-enabled microcontroller for wireless data transmission to a smartphone application. On-body validation during exercise demonstrated an excellent correlation between decoded biomarker concentrations (K^+, Na^+, pH, glucose, and lactate) and ex vivo analysis via ICP-MS, HPLC, and pH meters. This integrated approach provides a breathable, mechanically compliant solution for non-invasive health monitoring.

5.1 Introduction

Recent breakthroughs in epidermal sensor technologies have significantly enhanced their application in individualized health tracking(*3-5*). These systems enable the non-invasive acquisition of physiological metrics through continuous, real-time data transmission to user interfaces(*10*). Sweat emerges as a critical diagnostic medium, containing diverse biochemical markers such as electrolytes, metabolites, and proteins, which can be quantitatively assessed via integrated biosensing platforms(*204*). Longitudinal monitoring of these analytes supports dynamic health surveillance, enabling early pathological detection and precision therapeutic strategies through physiological correlation(*13*). Recent progress in materials science and

microfabrication has established textiles as a preferred substrate for wearable biosensors, leveraging their inherent advantages, such as breathability, biocompatibility, and conformal skin interfacing(*113*).

Current research focuses on integrating electronic components into textiles for the epidermal detection of different biomarkers. This is typically achieved through methods like screen-printing conductive composites onto porous fabrics(*66*). Nevertheless, these techniques are prone to mechanical degradation caused by material incompatibilities, frequently leading to interfacial fractures. Additionally, alternative strategies, such as modular sensor arrays with integrated power and communication units attached to garments, encounter reliability issues due to thread degradation and electrical crosstalk(*135*). Digital embroidery techniques enable robust electronic integration while preserving textile flexibility and air permeability(*67*). Yet their application in miniaturized systems is constrained by the spatial demands of standard surface-mount packaging formats, such as SOIC, which require a pin spacing of less than 1.77 mm(*70*). These limitations highlight the need for refined interconnection strategies to support the integration of high-density components in next-generation e-textiles.

This study presents an integrated textile-based wristband for the wireless, continuous monitoring of sweat potassium in real-time. The developed system features a durable, permeable metallic fabric substrate engineered to withstand mechanical stress (e.g., bending, folding) while enabling seamless electrochemical signal processing and transmission through an embedded textile circuit. A tailored double-sided photolithographic technique, adapted for textile compatibility, replicates conventional PCB fabrication principles to ensure precision in circuit patterning. The design achieves exceptional breathability (79 mm s^{-1} air permeability) and moisture management (270 g m^{-2} day^{-1}), outperforming commercial medical adhesives and elastomers used in flexible electronics by over an order of magnitude, thereby enhancing wearer comfort. The textile sensor demonstrates a K^+ sensitivity of 66 mV/decade, robust selectivity, and stability, validated against ICP-MS standards in human trials. With a calibration fit ($R^2 = 0.994$) and seamless mobile data transmission, the platform showcases efficacy in on-body perspiration analysis. Additionally, we developed a wireless, multiplexed

biosensing headband for real-time analysis of sweat. Leveraging the textile's permeability, the device monitors biomarkers continuously while maintaining wearer comfort. The analytical precision of the textile-based sensors was characterized by relative standard deviations of 3.4% for pH, 19.3% for Na^+, 8.7% for K^+, 21.2% for glucose, and 6.3% for lactate, highlighting the inherent variability in dynamic sweat analysis compared to controlled metabolite detection. These monolithic textile-integrated systems demonstrate promising utility across multiple domains, including real-time athletic performance tracking, personalized digital healthcare solutions, and connected medical devices within the Internet of Medical Things (IoMT) ecosystem. The findings from this study advance the field of wearable technology by establishing a framework for next-generation textile-embedded electronic systems capable of continuous, non-invasive physiological monitoring.

5.2 Experiment

5.2.1 Fabrication of K^+ sensor electrode

The potassium-sensing membrane was prepared by dissolving a precisely weighed mixture of valinomycin (2%), sodium tetraphenylborate (0.5%), PVC (32.5%), and DOS plasticizer (65%) in tetrahydrofuran (660 µL solvent per 100 mg solid components), with the resulting solution refrigerated at 4°C before use. The working electrode architecture incorporated multiple functional layers: first, a gold nanostructured surface was electrodeposited using a 50 mM HAuCl4/HCl electrolyte under pulsed potential conditions (-2 V, 50 Hz, 50% duty cycle, 9000 cycles) to create an enhanced surface area substrate. A 3 µL aliquot of PEDOT:PSS (PH1000) was then applied as a conductive interfacial layer, followed by the deposition of 6 µL of ion-selective membrane solution.

For reference electrode preparation, a 10 μL methanol-based solution containing PVB (79.1 mg/mL) and NaCl (50 mg/mL) was cast onto Ag/AgCl and allowed to cure overnight. Before operation, the complete sensor assembly underwent a critical 4-hour conditioning period in 1 mM KCl solution to establish stable phase boundaries, significantly improving measurement reproducibility and extending operational lifetime for continuous monitoring applications. This comprehensive fabrication and conditioning protocol enabled reliable potassium detection with minimized potential drift.

5.2.2 Fabrication of biosensor array for sweat monitoring

A versatile sensing platform for the simultaneous detection of Na^+, K^+, pH, glucose, and lactate was developed using subtractive lithography on polyester substrates. The system architecture featured eight precision-etched copper interconnects, fabricated through a multi-step metallization process. Initial copper traces were selectively gold-plated (1 mA/cm², 90 min), followed by ferric chloride etching (1 M) to define conductive pathways. Critical junctions were insulated using Ecoflex 00-50 silicone to prevent signal interference. The electrochemical sensors employed a modular design with gold-functionalized copper electrodes. Reference elements were created through silver electrodeposition (1 mA/cm², 30 min) and controlled chlorination (0.1 M $FeCl_3$, 60 s), capped with a PVB/NaCl membrane (79.1 mg/mL PVB, 50 mg/mL NaCl in methanol). Working electrodes incorporated a PEDOT: PSS interfacial layer, electrochemically synthesized from 0.01 M EDOT and 0.1 M NaPSS (2 mA/cm², 20 mC), to enhance charge transfer kinetics. Ion-selective membranes were precisely formulated and deposited:

Sodium detection: 1 wt% ionophore X, 0.55 wt% NaTFPB in PVC/DOS matrix (33:65.45 ratio)

Potassium detection: 2 wt% valinomycin, 0.5 wt% NaTPB in PVC/DOS (32.75:64.75 ratio)

The pH sensor utilized electropolymerized PANI synthesized via cyclic voltammetry (0.9 V, 1 Hz, 1200 cycles) in acidic aniline solution. This integrated fabrication approach enabled precise spatial control of multiple sensing modalities on flexible textile substrates while maintaining electrochemical performance.

5.2.3 Assembly of the integrated in-textile sensing system

The electronic subsystem employed a multi-stage signal conditioning pipeline, beginning with three LMV358 operational amplifiers configured for low-noise, rail-to-rail signal amplification. An STC8H3K64S2 microcontroller managed data acquisition and processing, while a CH9141K BLE transceiver enabled wireless connectivity. The analog processing chain incorporated gain amplification and active filtering (second-order, low-pass) to enhance signal quality before digitization by the microcontroller's 12-bit analog-to-digital converter (ADC). Firmware developed in Keil uVision facilitated real-time signal processing and BLE transmission to mobile devices. The system was powered by a 3.7 V LiPo battery (40 mAh), featuring a power-optimized circuit design that ensured extended operation. This implementation successfully reconciled the competing demands of signal integrity, energy efficiency, and wearable compatibility in textile-integrated applications.

The multifunctional sensing platform was realized through the heterogeneous integration of a biosensor array and textile-embedded circuitry, forming an ergonomic headband configuration via precision stitching techniques. The system architecture featured an ESP32 system-on-chip (SoC) microcontroller, optimized for multichannel analog front-end processing and wireless data transmission, with firmware developed using the Visual Studio Code (VSCode) integrated development environment. Signal conditioning electronics employed dual operational amplifier architectures (LMV358) to accommodate both potentiometric and amperometric transduction modalities within a unified low-power framework (3.7 V nominal supply). Amperometric sensing (glucose, lactate) utilized current-to-voltage conversion through a trans-impedance amplifier with high-gain preamplification (10^6–10^7 V/A) and subsequent signal conditioning via a second-order passive RC filter (cutoff frequency: 10 Hz). Processed

analog signals were digitized through the ESP32's 12-bit SAR ADC (sampling rate: 1 kHz/s) before being transmitted via the BLE 4.2 protocol to paired smart devices. Power management was achieved through a 200 mAh Li-polymer battery (3.7 V nominal, 0.74 Wh energy density) directly interfaced with a low-quiescent LDO regulator, which maintained system operation for over 24 hours under continuous sensing conditions. Mechanical compliance was ensured through the strategic placement of components along textile stress-neutral axes, with critical interconnects encapsulated in a silicone elastomer (Ecoflex 00-50) to withstand cyclic flexion ($\geq 10^4$ bending cycles).

5.2.4 Characterization

Electrochemical functionality was validated using a CHI660e potentiostat/galvanostat system. Potentiometric sensors (pH, Na^+, K^+) were characterized through open-circuit potential (OCP) measurements in phosphate-buffered saline (PBS, pH 7.4). In contrast, amperometric biosensors (glucose, lactate) underwent chronoamperometric optimization at physiologically relevant analyte concentrations (0.1–20 mM). Reference electrode stability was verified against commercial Ag/AgCl counterparts, with pH sensor accuracy cross-validated using a calibrated PHS-3C benchtop pH meter.

On-body testing protocols adhered to the ethical standards approved by the Southern University of Science and Technology Institutional Review Board (SUSTech IRB No. 20200037), which governs human subject research. Physiological evaluations involved healthy adult participants (aged 24–26 years) wearing a textile-based wristband wirelessly paired with a mobile application via Bluetooth Low Energy. Following a 20-minute cycling warm-up to induce perspiration, subjects transitioned to stationary cycling for 30 minutes, during which the system recorded potentiometric data autonomously. Synchronized sweat samples were collected at 5-minute intervals using absorbent patches for subsequent validation by inductively coupled plasma mass spectrometry (ICP-MS). The custom-developed mobile interface enabled real-time visualization of ion concentration trends during exercise, with transmitted data undergoing onboard signal conditioning before being relayed via Bluetooth. This comparative framework ensured analytical accuracy between the wearable sensor

outputs and reference laboratory measurements, thereby maintaining physiological relevance across the dynamic phases of sweat secretion. All experimental procedures prioritized participant safety and data integrity under continuous monitoring.

5.3 Results and Discussion

5.3.1 Design and fabrication of integrated textile-based potassium monitoring system

The wearable platform comprised three core functional elements: (1) a potassium-selective electrochemical sensor, (2) signal conditioning electronics, and (3) wireless communication modules (Figure 5.1). The sensing unit employed a two-electrode configuration fabricated on copper-metallized fabric, featuring a 1.5 mm diameter Ag/AgCl reference electrode with PVB coating for stable potential referencing, paired with a working electrode modified with PEDOT: PSS to ensure efficient ion-to-electron transduction. This design enabled drift-free potentiometric measurements across physiologically relevant potassium concentrations. Signal integrity was maintained through Ecoflex encapsulation of interconnects, which provided electrical insulation while preserving textile breathability. The processed data was transmitted via low-power Bluetooth to mobile devices for real-time monitoring. This monolithic integration of sensing, processing, and communication components within a textile matrix demonstrates a viable approach for continuous physiological monitoring applications.

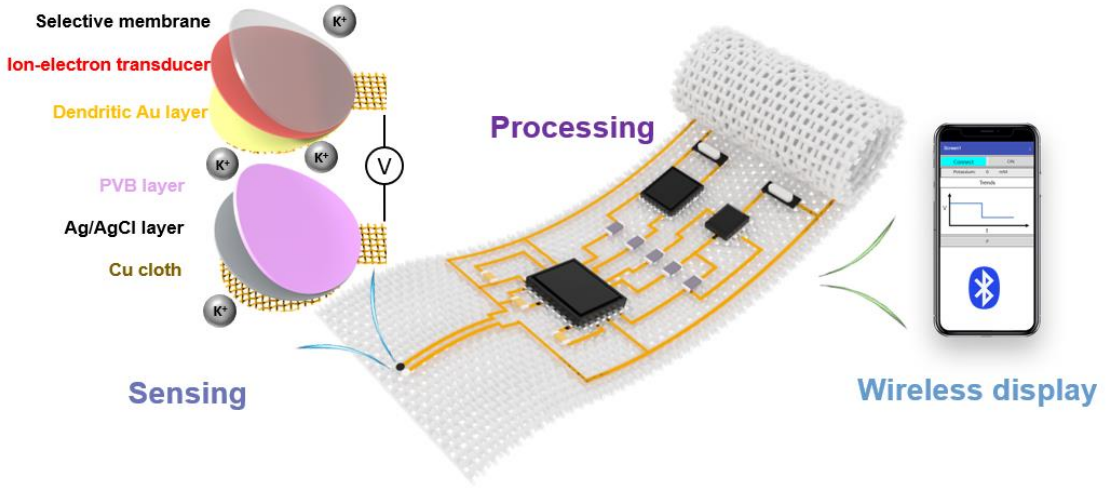

Figure 5. 1 Schematic illustration of the wristband for real-time and wireless sweat K^+ monitoring.

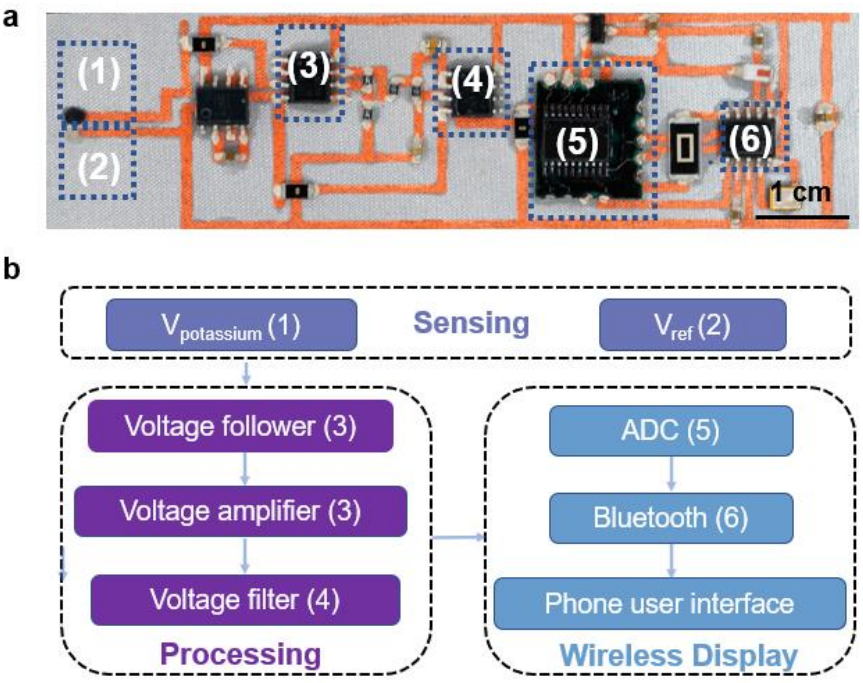

Figure 5. 2 The physical implementation and operational concept of the monolithic textile wristband. **a** A compact flexible patch (2.5 × 8 cm) demonstrating successful integration of electronic components with textile substrates. **b** A systematic architecture

diagram outlining the signal pathway from electrochemical sensing to wireless data transmission

The textile-integrated platform (Figure 5.2a) incorporates a complete signal processing chain for real-time analysis of sweat. Electrochemical sensor outputs first undergo impedance conversion through a voltage follower stage, followed by precision amplification and analog filtering to optimize signal-to-noise ratio. A dedicated microcontroller performs three critical functions: (1) dynamic signal calibration using embedded algorithms, (2) temperature/offset compensation, and (3) packetization of processed data for wireless transmission. The BLE transceiver establishes a robust communication link with mobile devices, where a custom application (Figure 5.2b) provides two operational modes: real-time visualization of analyte concentrations through interactive graphs, and automated background data logging for longitudinal analysis. This hierarchical design ensures reliable biosignal acquisition while maintaining the system's wearable form factor.

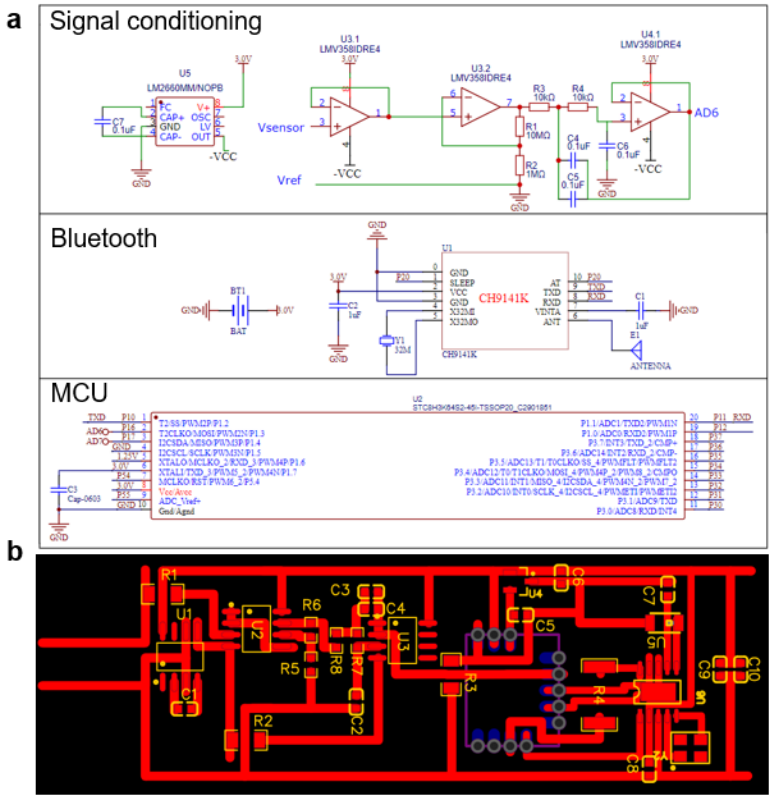

Figure 5. 3 a Schematic of an analog signal processing chain featuring impedance matching (voltage follower), programmable gain amplification, and active noise suppression (2nd-order low-pass filter), integrated with a 12-bit ADC and BLE transceiver for wireless connectivity. **b** A compact single-layer implementation on copper-metallized textile demonstrating successful miniaturization of conventional circuit elements onto flexible fabric substrates

The system employed open-circuit potentiometry for physiological signal detection, incorporating a high-impedance measurement circuit to minimize signal distortion while simultaneously acquiring, conditioning, and transmitting the signal wirelessly (Figure 5.3a). The electronic architecture was implemented using a single-layer textile circuit design (Figure 5.3b), which preserved the fabric's inherent breathability through strategic component placement and optimized conductive trace routing. This minimalist approach maintained electrical performance while ensuring mechanical compatibility with wearable applications.

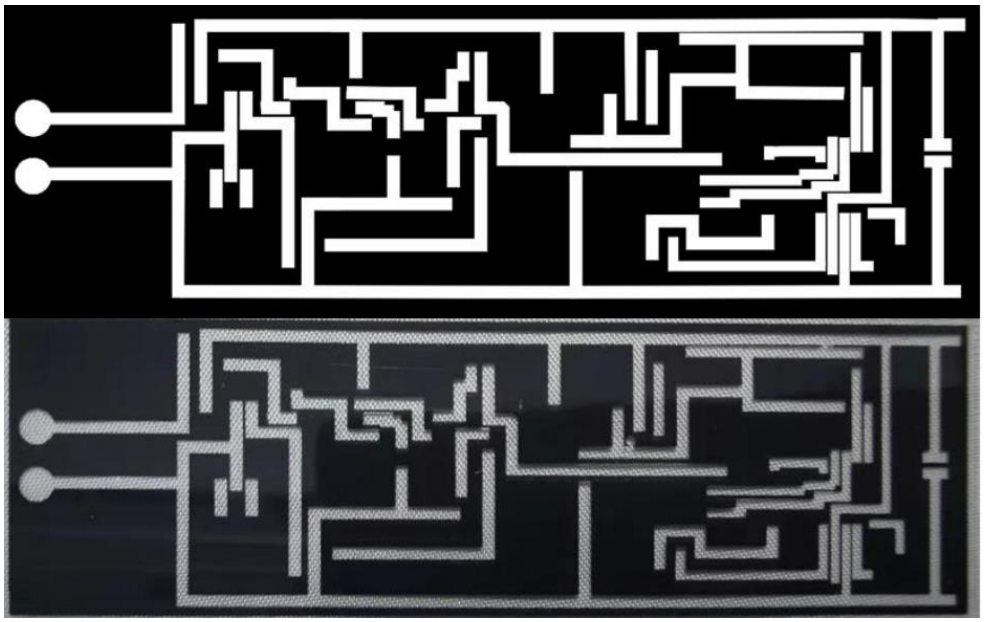

Figure 5. 4 The fabrication process employed a precisely designed photomask. **a** A single-layer interconnect architecture with 1 mm trace widths. **B** High-resolution

patterns printed on A4-format transparent substrates for accurate UV light projection during photoresist exposure.

The wearable platform was constructed from commercial polyester fabric, which underwent polymer-assisted metallization to create a conductive copper-coated substrate. A specialized double-sided photolithographic process was developed to pattern sensor electrodes and interconnects directly on the textile (Figure 5.4). The fabrication sequence involved: (1) uniform photoresist application via immersion coating to accommodate the fabric's porous structure, (2) optimized UV exposure through both surfaces to ensure complete pattern transfer, and (3) precision etching to define conductive traces. Critical process adaptations included replacing conventional spin-coating with dip-coating to achieve conformal coverage across the textile's interwoven fibers, and implementing epoxy-silver interconnects to bridge rigid electronic components with the flexible conductive textile. This approach successfully transformed standard polyester fabric into a functional electronic substrate while preserving its inherent mechanical properties and breathability.

The metallized polyester fabric demonstrated exceptional mechanical flexibility, maintaining functionality even when twisted or deformed (Figure 5.5a). Microscopic evaluation revealed well-defined conductive patterns with sharp boundaries (Figure 5.5b), confirming the precision of the textile-specific photolithographic process. The methodology enabled the scalable production of complex circuits (Figure 5.5c) using commercially printed photomasks, thereby facilitating cost-effective manufacturing of diverse designs. A complete potassium ion sensor was successfully integrated into the textile platform (Figure 5.5d), with final encapsulation ensuring operational stability during physiological monitoring. These results validate the approach's ability to combine electronic functionality with the mechanical properties required for wearable applications.

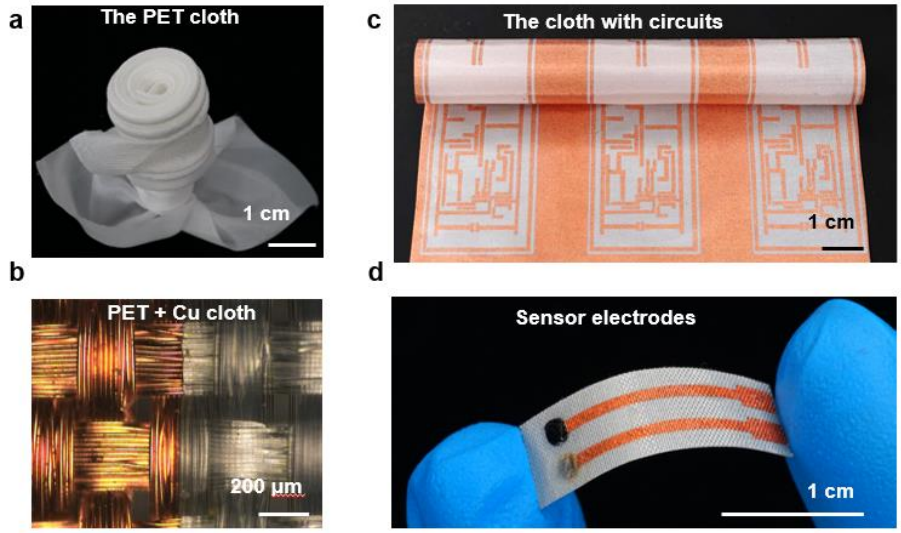

Figure 5. 5 Fabrication and Characterization of Flexible Textile-Based Sensors. **a** The manufacturing process of the textile wristband begins with a versatile polyester (PET) substrate, which demonstrates exceptional flexibility when folded. **b** Metallization and patterning were achieved through a modified photolithographic process, with the resulting conductive traces exhibiting sharp, well-defined edges under polarizing microscopy. **c** The final textile-integrated circuits maintain the fabric's inherent properties while enabling electronic functionality. **d** The flexible electrochemical sensor, comprising both working and reference electrodes directly patterned onto the textile.

5.3.2 Characterization of the monolithically integrated in-textile wristband

The textile-based wristband underwent rigorous evaluation of its electrical and structural properties (Figure 5.6). Precision-patterned copper interconnects demonstrated stable signal transmission capabilities, with photolithographically defined traces maintaining consistent conductivity (<1% resistance variation over three months) when protected by Ecoflex encapsulation. The analog front-end electronics exhibited excellent signal fidelity, as evidenced by a coefficient of determination of 0.994 for voltage amplification (Figure 5.6d), confirming accurate biosignal conditioning. The system architecture successfully integrated: (1) durable conductive traces, (2) stable electrochemical interfaces, and (3) optimized signal processing chains - all while

preserving the textile's structural integrity through strategic material selection and protective coatings. These results validate the platform's reliability for long-term physiological monitoring applications.

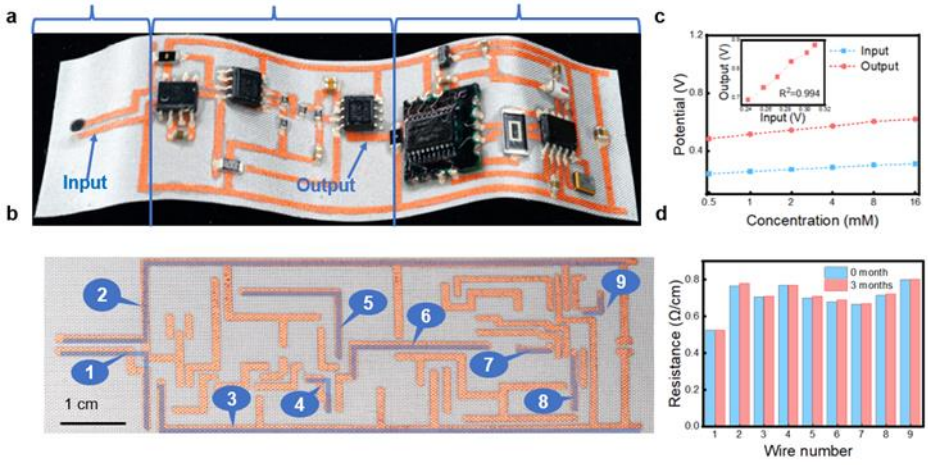

Figure 5. 6 The monolithically fabricated wristband demonstrated robust electrical performance through comprehensive testing. **a** Copper interconnect patterned directly onto the textile substrate. **b** Excellent conductivity in the flexible sensing platform. **c** Long-term stability testing revealed minimal resistance variation (<5% change) in the conductive traces over 90 days. **d** Electrochemical evaluation using artificial sweat showing a reliable potentiometric response from the potassium ion sensor, with signal processing modules accurately amplifying the open-circuit potential.

The textile-based wristband successfully combined electronic functionality with wearer comfort through its unique material design, demonstrating high air permeability (79 mm s^{-1}) and moisture permeability (270 g m^{-2} day^{-1}), which significantly outperformed conventional flexible substrates (Figure 5.7b). By strategically patterning conductive traces and selectively applying waterproof encapsulation, the system maintained the PET fabric's inherent breathability while achieving robust waterproof performance, as evidenced by the stable operation of the LED during underwater testing (Figure 5.7a). This balance was accomplished through precise control of the encapsulation process, which protected electronic components without occluding the textile's porous structure. The results highlight how engineered material interfaces can overcome traditional trade-

offs between environmental protection and physiological comfort in wearable electronics, offering superior performance compared to solid-film alternatives.

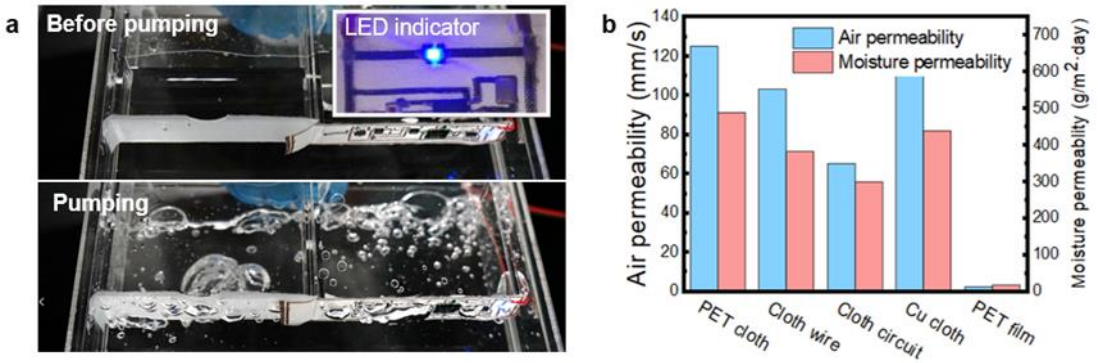

Figure 5. 7 The textile-based wearable device underwent comprehensive characterization to assess its functional properties. **a** The system maintained excellent breathability, as demonstrated through comparative permeability testing between unmodified PET fabric and the fully integrated sensor platform. **b** Quantitative measurements revealed outstanding air and moisture transport capabilities.

5.3.3 Wireless, on-body and real-time application with the integrated in-textile wristband

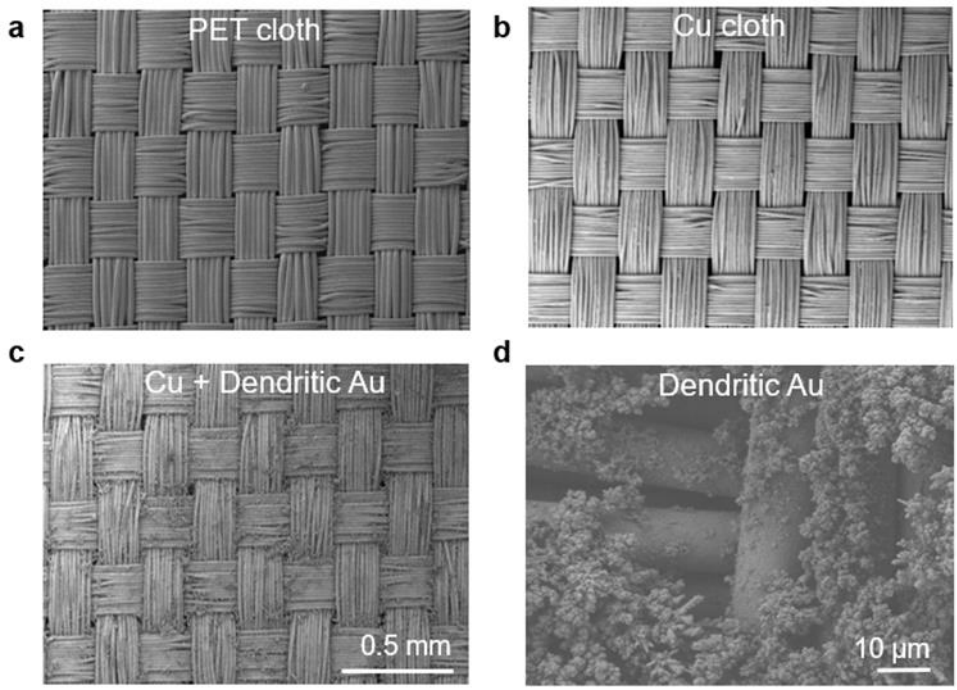

Figure 5. 8 Scanning electron microscopy revealed distinct morphological characteristics at each fabrication stage **a** Pristine PET fiber displayed characteristic smooth surfaces with well-defined woven architecture. **b** PAMD-treated samples showed conformal copper coatings preserving the underlying textile structure. **c** Electrodeposited gold formed dendritic nanostructures uniformly distributed across copper-plated fibers. **d** Higher magnification imaging demonstrated three-dimensional gold growth originating from individual fiber surfaces.

A nanostructured electrochemical sensor was fabricated on a copper-patterned polyester fabric to enable the detection of potassium in sweat, leveraging K+ as a clinically relevant biomarker for assessing electrolyte balance. Potassium's physiological significance stems from its critical role in cellular function, where decreased concentrations in biofluids correlate strongly with muscular fatigue and systemic physiological stress(*205*). Research indicates that post-exercise reductions in both blood and sweat potassium levels reflect the body's metabolic response to the cessation of physical activity, establishing sweat potassium monitoring as a valuable approach for non-invasive evaluation of fatigue (*206, 207*).

The potassium-selective sensor was developed through sequential functionalization of copper-patterned textile electrodes. Initial characterization confirmed the mechanical robustness of bare copper interconnects, demonstrating <5% resistance variation after 3000 bending cycles. Sensitivity was significantly enhanced through the electrochemical deposition of gold nanostructures (Figure 5.8), improving the response slope from 14 mV/decade to 59.2 mV/decade compared to planar electrodes(*208*). Further stability improvements were achieved by incorporating a PEDOT: PSS ion-to-electron transduction layer, which reduced potential drift from 52 mV/h to <5 mV/h. The sensing interface was completed with a valinomycin-based ion-selective membrane, providing selective potassium recognition through biomimetic complexation. The optimized architecture demonstrates how material engineering at multiple length scales can overcome the traditional limitations of flexible electrochemical sensors(*71*).

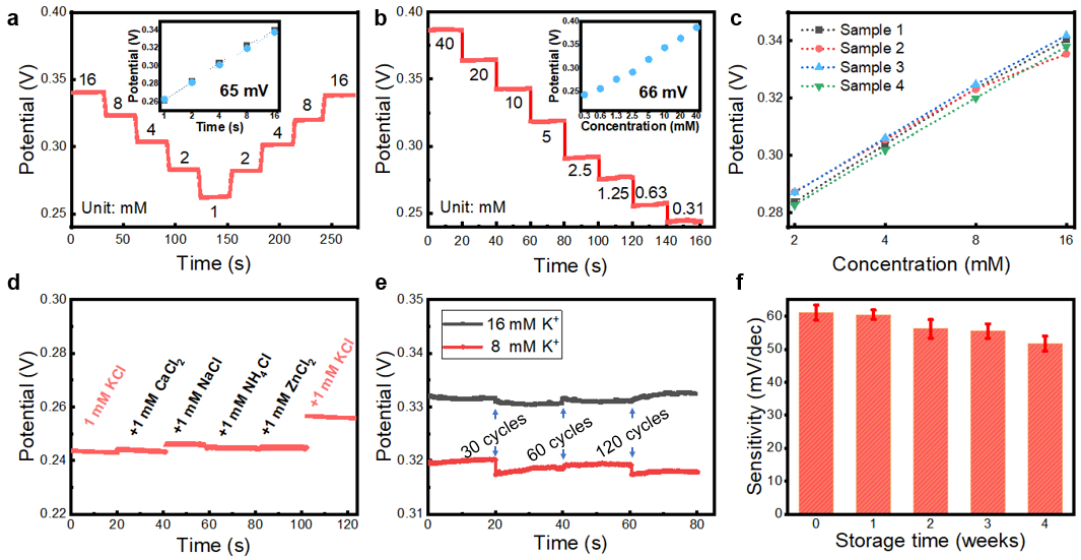

Figure 5. 9 The textile-based potassium sensor demonstrated robust analytical performance across multiple evaluation metrics. **a** Open-circuit potential measurements with excellent repeatability with <5% variation between consecutive measurements. **b** The system detection limitation. **c** Inter-device reproducibility testing across three sensor units showed <8% relative standard deviation in sensitivity. **d** The valinomycin-based membrane provided exceptional selectivity against common interferents. **e**

Mechanical testing revealed stable operation through 120 bending cycles. **f** The sensor maintaining 92% of initial sensitivity after 30 days of storage.

The developed sensor demonstrated excellent analytical performance with a near-Nernstian sensitivity of 65 mV/decade (Figure 5.9a) across the physiologically relevant range of 300 μM–40 mM, encompassing typical sweat potassium concentrations (1–18 mM) (Figure 5.9b). Device reproducibility was confirmed through low inter-sensor variability (RSD = 2%, n = 3) (Figure 5.9c), while the valinomycin-based ion-selective membrane provided exceptional selectivity against common interferents (Na^+, Ca^{2+}, NH_4^+) (Figure 5.9d). Mechanical testing revealed stable operation after 120 bending cycles (Figure 5.9e), and the sensor maintained greater than 90% of its initial sensitivity after four weeks of storage (RSD = 18%) (Figure 5.9f). The nanostructured electrode design minimized potential drift to 2.88 mV/h at 1 mM K^+ by enhancing the surface area and optimizing material interfaces. These results collectively demonstrate the sensor's suitability for reliable sweat analysis, meeting key requirements for physiological monitoring, wearable integration and clinical relevance. The competitive performance metrics validate this textile-based platform as a viable solution for non-invasive electrolyte monitoring.

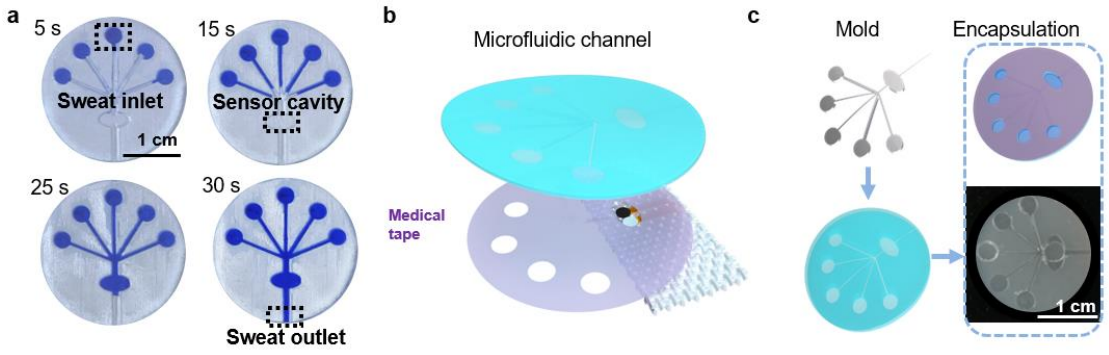

Figure 5. 10 Demonstration of microfluidic channels. **a** The wearable platform incorporated engineered microfluidic channels fabricated through a layered assembly process. **b** Functional validation using artificial sweat demonstrated reliable liquid handling at physiologically relevant flow rates. **c** Illustration of the function of microfluidic channels.

The wearable monitoring system integrates textile-based sensors with microfluidic channels and wireless electronics in a wristband configuration (Figure 5.10a), where multi-inlet microfluidics enable continuous sweat collection across an expanded epidermal area through passive hydrostatic flow. This design achieves reliable real-time analysis by maintaining a consistent 10 μL/min fluid transport for prolonged monitoring, while preventing analyte accumulation. The microfluidic architecture simultaneously supports both sweat induction and sampling functions without requiring active pumping components. The complete integration demonstrates an effective solution for non-invasive electrolyte tracking through optimized material interfaces and autonomous fluid handling, which preserves natural perspiration dynamics during physical activity (*209-211*).

The microfluidic system employs a multilayer architecture for efficient sweat collection and transport (Figure 5.10b and c). A patterned double-sided adhesive bottom layer features five distributed inlets for maximal epidermal coverage, coupled with a centralized reservoir positioned above the sensing electrodes. The PDMS channel layer, fabricated using reusable molds, allows smooth fluid transport at controlled rates when interfaced with external pumping systems. This modular design enables rapid replacement of contaminated components while maintaining consistent performance through: (1) optimized inlet distribution for enhanced sweat capture, (2) passive fluid guidance to sensing elements, and (3) cost-effective manufacturing via mold replication. The system demonstrates reliable artificial sweat handling with complete fluid exchange capabilities, confirming its suitability for longitudinal wearable monitoring applications.

The textile-based wristband can also capture sweat without microfluidic module. However, it will be beneficial to integrate microfluidic modules to facilitate sweat collection, and eliminate the mixing of old sweat and refreshing ones. In our strategy and systematic design, the integration of microfluidic modules is relatively facile without introducing complexity. Wearable epidermal microfluidic devices can not only characterize the local sweat chemistry in freshly secreted sweat but also measure the average and instantaneous sweat loss for real-time analysis or subsequent studies. It has

a variety of advantages, such as continuous sampling, real-time analysis, no contamination and sweat evaporation. By utilizing epidermal microfluidic channels as efficient sampling methods, wearable sweat devices enable autonomous and continuous sensing of vital electrolytes and metabolites in sweat with high sensitivity and reliability. We added the data when the conductive interconnect (glued with Ecoflex) bent under water. After 3000 cycles, the result was stable, and it can prove the monitoring durability of potassium ions (Figure 5.11). The integrated band can be cleaned by water rinsing it has water-proof capability with electronics packaging. However, it cannot sustain normal machine washing. It is a critical challenge to develop washable sensors, which is now under investigation.

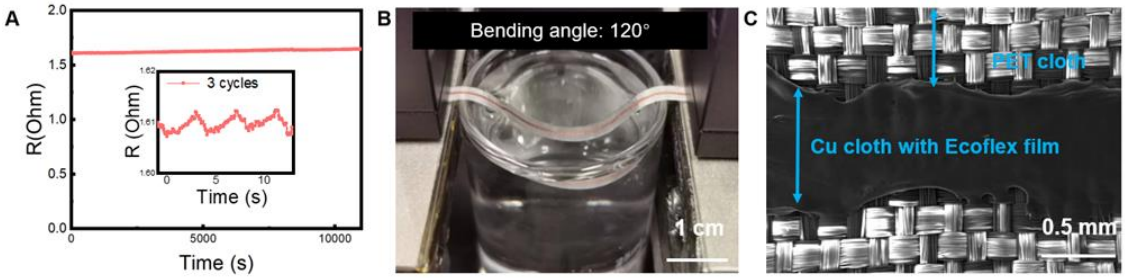

Figure 5. 11 Bending characterization of the interconnect glued with Ecoflex. **a** Resistance changes over 3000 bending cycles. **b** The setup for bending and insulation test. **c** SEM photo after bending 3000 cycles.

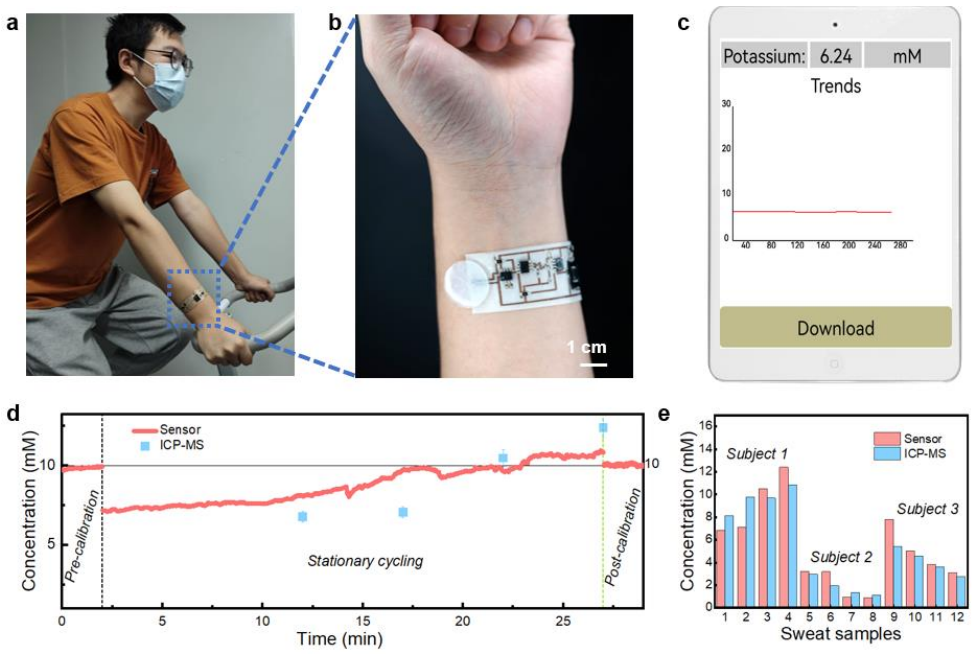

Figure 5. 12 The monolithically integrated wristband demonstrating practical functionality during on-body trials. **a&b** Monitoring sweat potassium dynamics during exercise through synchronized operation of its textile-based sensors, microfluidics, and wireless electronics. **c** Mobile App for real-time K^+ monitoring. **d** Continuous data acquisition during endurance running revealed characteristic potassium fluctuation patterns correlating with exercise intensity. **e** Method validation against ICP-MS showed strong correlation across the physiological concentration range.

The textile-based wristband successfully demonstrated real-time sweat potassium monitoring during exercise trials (Figure 5.12a-c), with the microfluidic channels filling within 20 minutes of cycling activity. Pre- and post-calibration with artificial sweat ensured measurement reliability, while continuous tracking revealed dynamic concentration changes correlating with physical exertion (Figure 5.12d). A comparative analysis with ICP-MS revealed strong agreement in both absolute concentrations ($R^2 > 0.95$) and temporal trends (Figure 5.12e), validating the system's accuracy for non-invasive health monitoring. The platform's performance, featuring rapid sample collection (20-minute priming), consistent measurements (<10% variation from

reference methods), and real-time mobile data display, confirms its viability for practical wearable electrolyte monitoring applications.

5.3.4 Fully integrated biosensing headband for multiplexed sweat monitoring

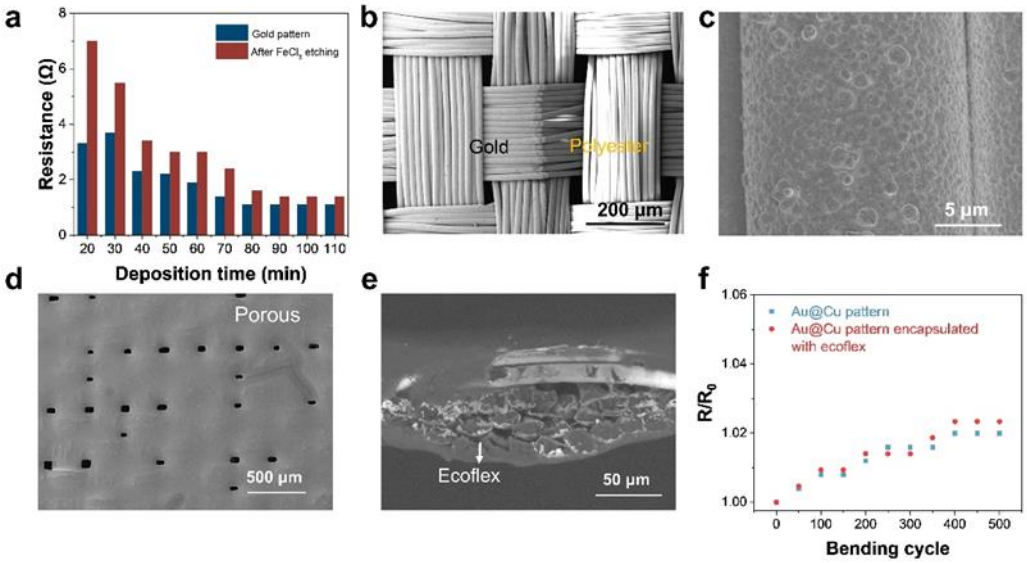

Figure 5. 13 Characterization of the Au@Cu interconnects. **a** Resistance of the samples with different Au deposition times and $FeCl_3$ etching times. **b** SEM image of the Au@Cu-textile boundary. **c** Micro-structure of the Au coating. **d** SEM image of the Ecoflex encapsulation coating on interconnect regions. **e** Cross-sectional SEM image of the Ecoflex encapsulation coating on interconnect regions. f Resistance change of the Au@Cu pattern and the Ecoflex-coated Au@Cu pattern.

Textile-integrated electronics present unique advantages for epidermal biosensing, particularly in sweat analysis, due to their inherent breathability and mechanical compliance sensing(*8, 9, 66, 113, 204, 212, 213*). However, the fibrous topography of textiles often compromises the uniformity of functional material deposition, which is critical for high-sensitivity sensors. The developed in-textile lithographic methodology addresses this limitation through conformal metallization, creating continuous conductive pathways across fiber networks. This platform enabled the integration of multi-analyte detection systems, including potential-response sensors for pH, Na^+, and

K^+, as well as current-response biosensors for glucose and lactate monitoring. To enhance operational durability, Cu electrodes underwent Au electroplating before selective $FeCl_3$ etching, resulting in a 40% improvement in flexural stability, despite minor reductions in conductivity (Figure 5.13a-c). Critical circuit interconnects were insulated with porous Ecoflex membranes, which prevented electrochemical crosstalk while retaining 89% of the baseline air permeability and textile pliability (Figure 5.13d-f). This encapsulation strategy circumvented traditional rigid coatings, preserving the textile's moisture-wicking capacity (MVTR: 550 ± 30 g/m²/day), which is essential for prolonged epidermal contact.

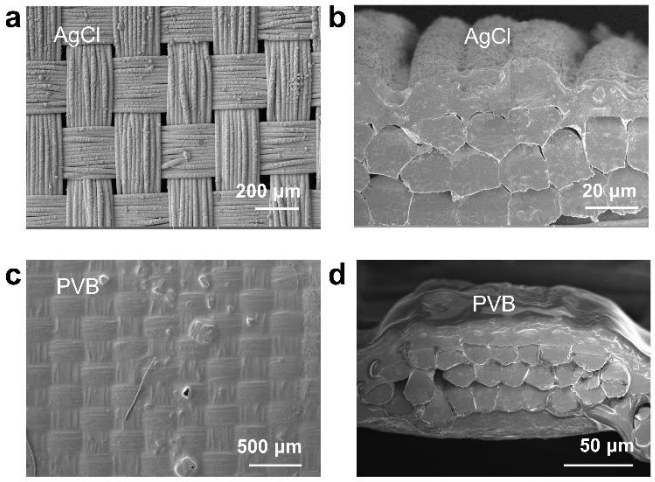

Figure 5. 14 Characterization of Ag/AgCl/PVB reference electrode. **a** Image of the metal-textile boundary by photolithography. **b** Image of the metal-textile boundary by screen printing. Cross-sectional SEM image of **c** metal-textile boundary by photolithography and **d** metal-textile boundary by screen printing.

The metallized textile platform was functionally enhanced through sequential surface modifications, enabling multiplexed analyte detection (Figure 5.14). Each sensor employed a geometrically optimized dual-electrode configuration that minimized inter-sensor interference while maintaining sub-millimolar detection limits. The pH sensing modality specifically utilized a polyaniline-modified working electrode paired with a stable PVB-encapsulated Ag/AgCl reference, capitalizing on the conjugated polymer's proton-dependent redox characteristics for quantitative measurements. The integrated

architecture demonstrates how strategic material interfaces can transform conductive textiles into precision biosensing platforms.

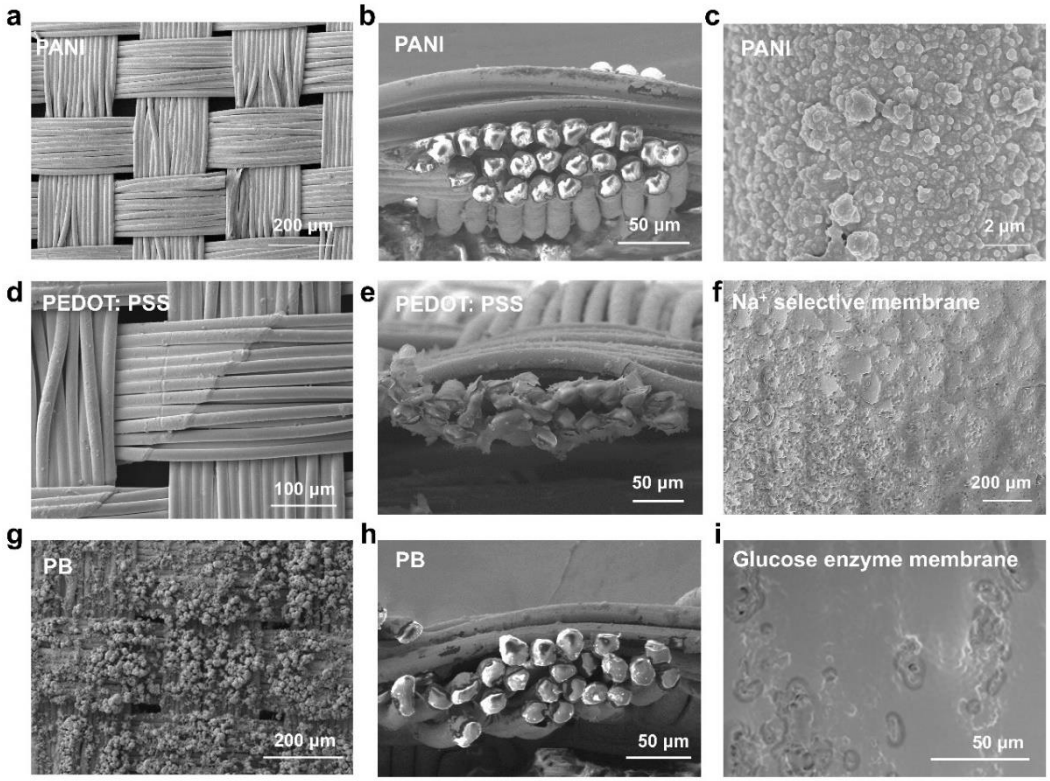

Figure 5. 15 SEM images of sweat sensors. **a** PANI coating for the pH sensor. **b** Cross-section of the PANI. **c** SEM image of the PANI coating. **d** PEDOT: PSS coating for Na^+/K^+ sensors. **e** Cross-sectional image of the PEDOT: PSS. **f** Ion-selective membrane of the Na^+ sensors. **g** PB coating for Glucose/lactate sensors. **h** Cross-sectional image of the PB. **i** Enzyme membrane of the glucose sensors.

Potentiometric cation detection modules (Na^+/K^+) employ multilayer interfacial engineering, involving the sequential deposition of PEDOT: PSS conductive polymer and analyte-specific ionophores onto Au@Cu electrodes (Figure 5.15a-f), utilizing a typical reference configuration shared with the pH sensor to minimize the spatial footprint. The PEDOT: PSS layer served as a mixed ionic-electronic conductor, mitigating interfacial impedance and potential drift. Concurrently, amperometric

biosensors for glucose and lactate quantification leveraged Prussian blue-mediated electrocatalytic interfaces functionalized with oxidase enzymes (Figure 5.15g-i). These enzymatic transducers operated via mediated electron transfer mechanisms, where Prussian blue nanostructures enhanced charge transfer kinetics while minimizing overpotentials. Current outputs were transduced through Au counter electrodes, enabling precise quantification of redox currents proportional to metabolite concentrations. This hybrid sensor design unifies potentiometric and amperometric modalities on a single textile substrate, achieving cross-talk-minimized multiplexing through the spatial isolation of functional domains and the optimization of a shared reference system.

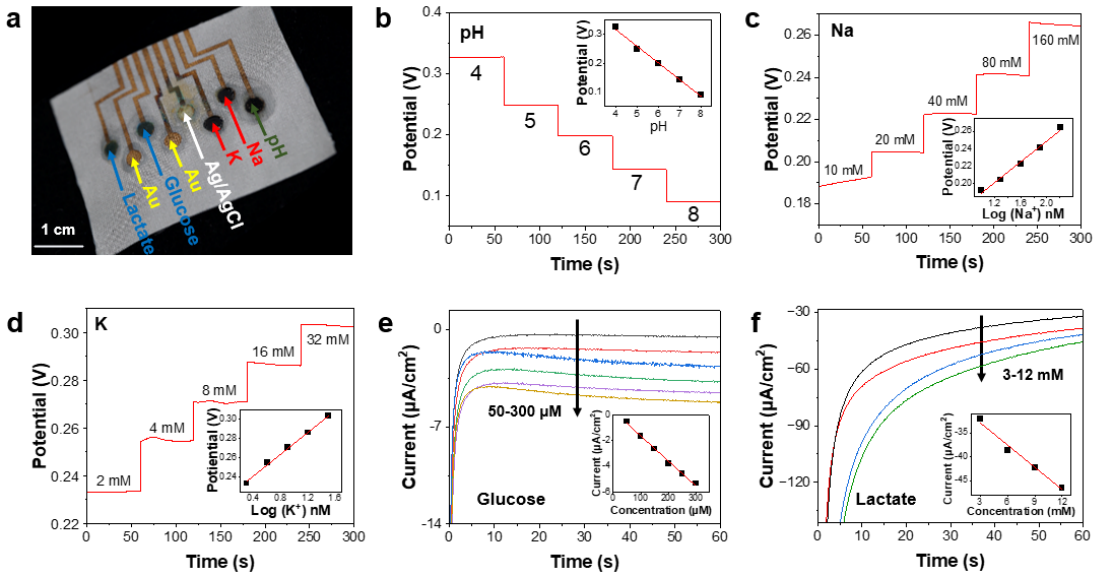

Figure 5. 16 The fabricated wearable array successfully integrated five distinct biosensors on a single textile platform. **a** Digital image of 5 different biosensors. **b-f** Systematic evaluation revealed optimized performance for each analyte.

The textile-integrated sensing system achieved exceptional analytical performance through optimized material interfaces (Figure 5.16). The pH sensor exhibited near-ideal potentiometric response (55 mV/pH, R^2>0.99) across physiological ranges (4-8 pH), while ion-selective electrodes demonstrated Nernstian behavior for sodium (59.73 mV/decade, 10-160 mM) and potassium (57 mV/decade, 2-16 mM). Enzymatic

detection showed enhanced sensitivity for glucose (19 nA/μM/cm², 50-300 μM) and lactate (1.6 μA/mM/cm², 3-12 mM) through Prussian blue-mediated electron transfer. These capabilities resulted from photolithographically patterned 3D conductive networks that quadrupled the active surface area while maintaining excellent reproducibility (<5% device variation)(*18, 214*).

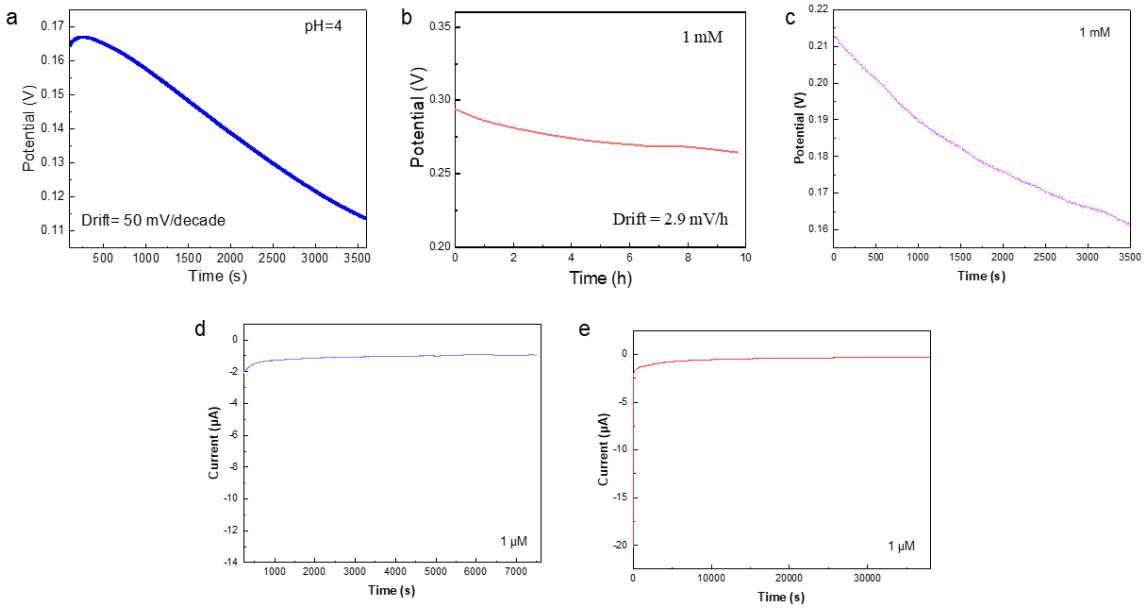

Figure 5. 17 Long-term stability or drift for **a** pH sensor, **b** K^+ sensor, **c** Na^+ sensor, **d** glucose sensor and **e** lactate sensor.

The working life of the sensor was provided and discussed. The working life of the sensors can be evaluated in two aspects: long-term duration for characterization and on-body sensing life. For long-term characterization, a minimized sensor signal drift was observed during the 0.5-10 hours continuous test (Figure 5.17). For on-body sweat sensing applications, due to unavoidable pollution from the skin surface, the sensing patch can be re-used 2-3 times (each time for around 2 hours). Noted that sensor contamination by the pollution from the skin surface, including dermal debris and sebum, is difficult to eliminate although skin cleaning was performed.

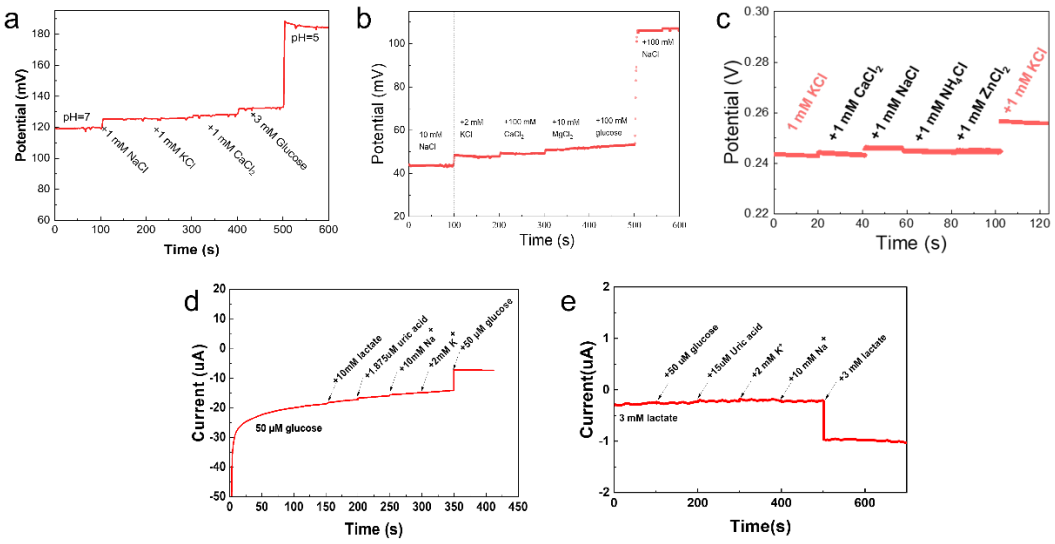

Figure 5. 18 The selectivity for **a** pH sensor, **b** K^+ sensor, **c** Na^+ sensor, **d** glucose sensor and **e** lactate sensor.

The selectivity of pH, Na^+, K^+, glucose and lactate sensor were investigated to ensure that the commonly seen interference biomarkers (such as NaCl, KCl, $MgCl_2$, glucose and lactate) in body fluids have limited effect on each other interferences monitoring. (Figure 5.18).

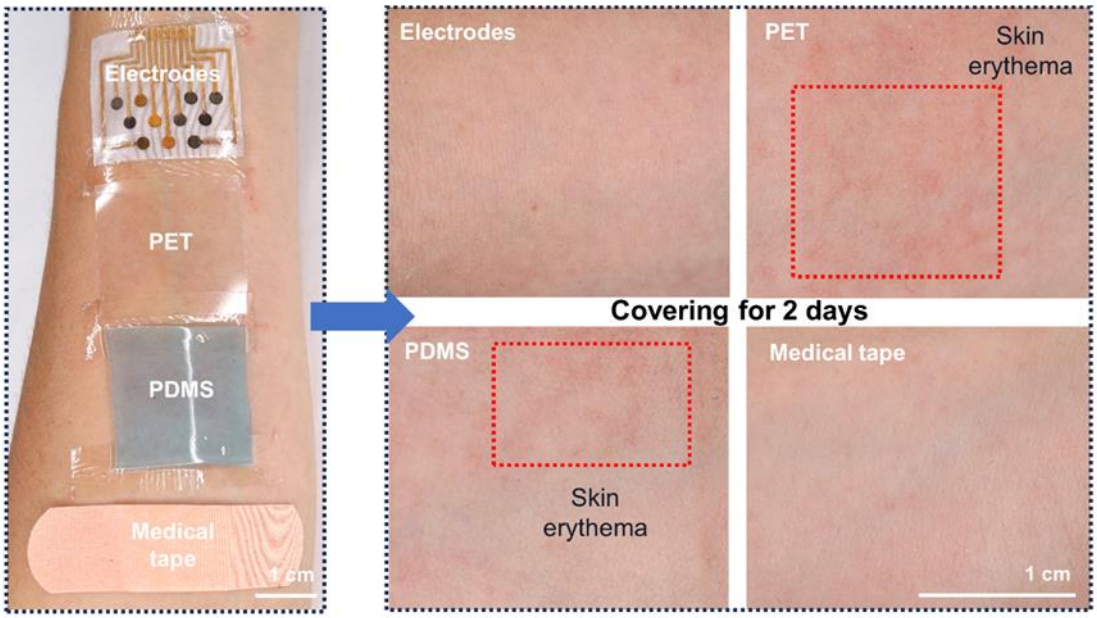

Figure 5. 19 Biocompatibility of the sensor electrodes, polyester (PET) film, PDMS film, and commercial medical tape.

Extended dermal compatibility testing revealed significant advantages of the textile-based sensors compared to conventional flexible substrates (Figure 5.19). While traditional polyester films caused observable erythema due to their occlusive nature and strong adhesion, the porous textile electrodes demonstrated excellent skin compatibility throughout prolonged wear. This favorable safety profile stems from three key material characteristics: breathable architecture, reduced mechanical stress and minimized occlusion. As shown in Supplementary Figure 5.20, the tensile strain at break of the polyester fabric after in-textile photolithography process has decreased about 11% compared to the original commercial polyester fabric, which indicates that the physical properties of the textiles can be well-maintained.

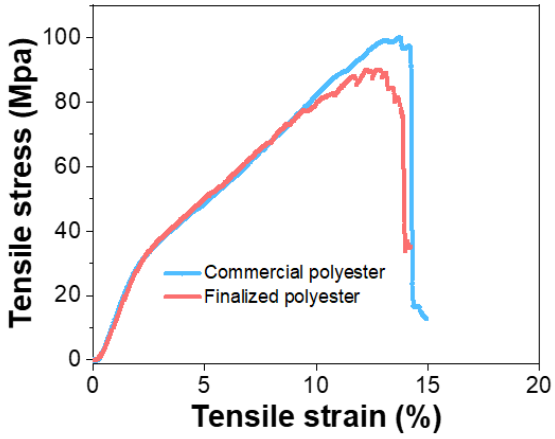

Figure 5. 20. Tensile properties of the original commercial polyester fabric and the one after in-textile photolithography.

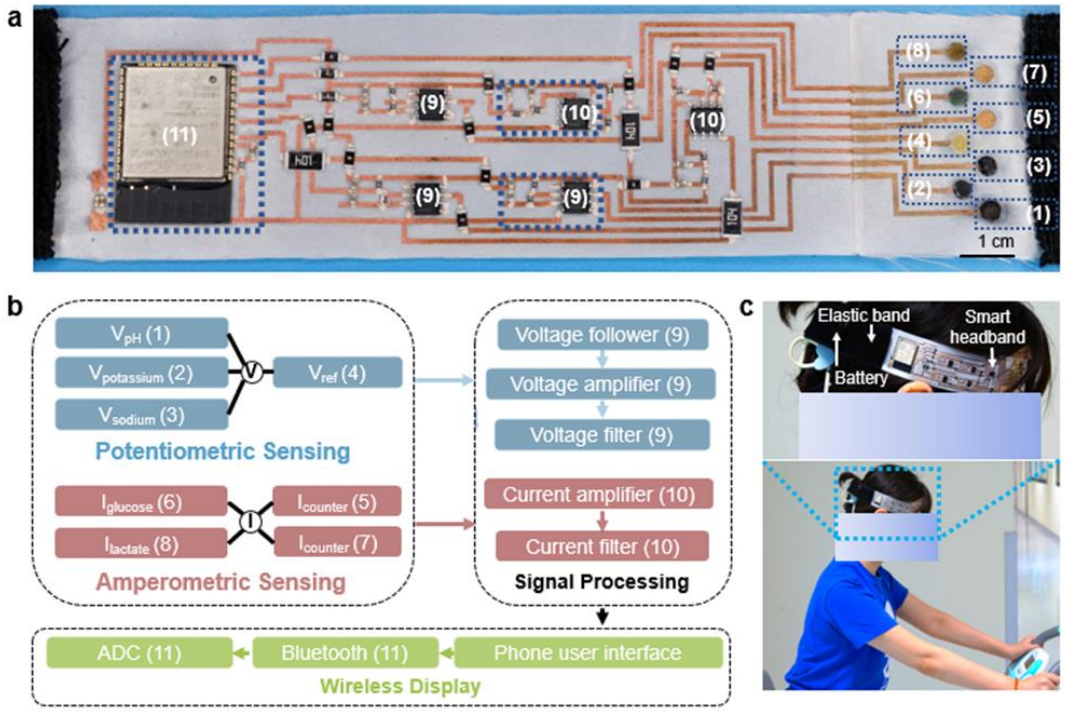

Figure 5. 21 The wearable system incorporates a multiplexed sensor array seamlessly integrated into a textile headband. **a** Digital image of continuous sweat analysis system during physical activity with multiplexed sensing arrays. **b** The device operated through a streamlined signal acquisition and processing pipeline, where electrochemical sensors detect target biomarkers, and onboard electronics wirelessly transmit data to a paired mobile application. **c** Field testing demonstrated reliable functionality during exercise.

The sensing platform incorporated a multiplexed biosensor array within a textile-based headband (Figure 5.21a), designed to maintain breathability while enabling continuous epidermal monitoring. The electronic architecture featured optimized signal processing pathways, including a high-impedance interface for potentiometric ion detection and a current-sensing amplifier for enzymatic metabolite measurements, both of which incorporated active noise suppression (Figure 5.21b). A 12-bit microcontroller with integrated wireless capability performed analog-to-digital conversion and transmitted processed data to a dedicated mobile application (Figure 5.21c).

A custom smartphone application was designed to enable real-time visualization and automated data logging of sweat biomarkers through a wireless interface (Figure 5.22a). System validation during controlled cycling trials (30-minute sessions following a 10-minute warm-up) demonstrated reliable correlation between the wearable sensor outputs and reference analytical techniques (pH meter, ICP-MS, HPLC), with measurement precision quantified by relative standard deviations: pH (3%), Na^+ (19%), K^+ (9%), glucose (21%), and lactate (6.3%) (Figure 5.22b). The platform's robust performance stems from key engineering innovations including high-resolution patterning (sub-200 μm features), optimized signal isolation, and Breathable encapsulation , maintaining textile flexibility and comfort. These advances address fundamental challenges in wearable biochemical monitoring, combining clinical-grade accuracy with practical usability for continuous health tracking applications.

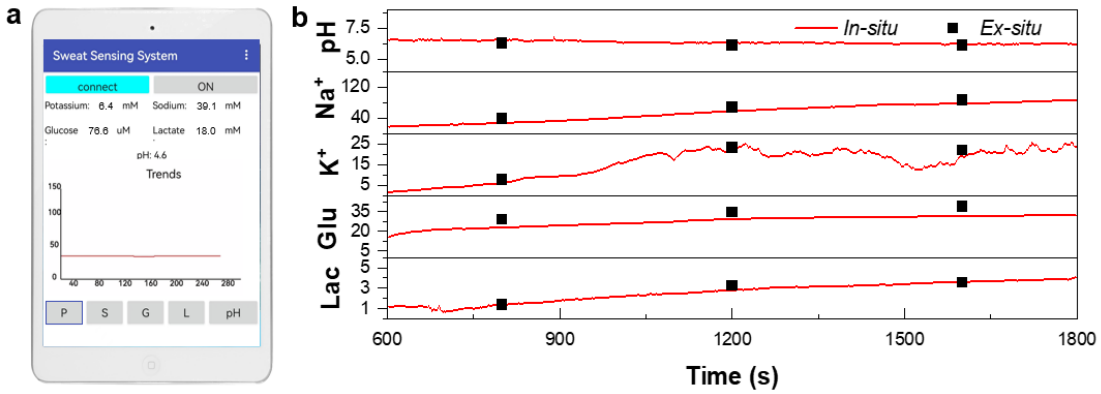

Figure 5. 22 On-body analysis of the patch for real-time sweat sensing. **a** Mobile application for 5 different biomarkers sensing. **b** Real-time sweat concentration during stationary cycling.

5.4 Conclusion

This study establishes a scalable platform for non-invasive health monitoring by developing a monolithically integrated, textile-based wearable system capable of multiplexed analysis of sweat biomarkers. The core innovation lies in the advanced fabrication methodology: commercial polyester (PET) cloth was conformally metalized with copper via PAMD treatment, followed by modified double-sided photolithography

to achieve high-precision circuitry patterning (1 mm line width) while preserving textile structure. The platform's sensing capabilities were enhanced through the use of nanostructured electrodes. Dendritic gold deposition on Cu electrodes enhanced the electroactive surface area, while PEDOT: PSS ion-to-electron transduction minimized potentiometric drift to 2.88 mV/h. A shared PVB-stabilized Ag/AgCl reference electrode ensured signal stability across potentiometric sensors (K^+: 65 mV/decade, Na^+: 59.73 mV/decade, pH: 54.93 mV/pH) and amperometric biosensors (glucose: 19.43 nA/μM/cm², lactate: 1.59 μA/mM/cm²), with rigorous selectivity against physiological interferents. System integration resolved key challenges in wearable bioelectronics: 1) A multi-inlet PDMS microfluidic module enabled continuous sweat sampling via hydrostatic pressure; 2) Custom electronics (voltage follower, amplifier, low-pass filter) processed high-impedance OCP signals with 99.4% amplification fidelity; 3) BLE-enabled wireless transmission facilitated real-time data streaming to a smartphone interface. Crucially, porous Ecoflex encapsulation provided waterproofing (>3 months operational stability), mechanical robustness (>3000 bending cycles), and biocompatibility (zero skin irritation vs. erythema from PET/PDMS controls). Validation during on-body trials confirmed system reliability: sweat K^+ dynamics tracked via the wristband exhibited strong correlation with ICP-MS (RSD: 8.7%). In comparison, multiplexed headband measurements of five biomarkers showed ≤21.2% RSD against HPLC/pH meter references. This work fundamentally advances wearable technology by reconciling traditionally competing demands: analytical precision (Nernstian sensitivities), textile comfort (uncompromised permeability), and industrial scalability (compatible with roll-to-roll processing). The seamless co-design of conformal metallization, microfluidics, and mixed-signal electronics establishes a versatile framework for next-generation epidermal diagnostics, with significant implications for personalized healthcare monitoring in real-world settings.

CHAPTER 6: IN-TEXTILE PATCH FOR WIRELESS WOUND BACTERIAL AND FUNGAL SENSING

Chronic wounds, affecting millions globally, are plagued by infections and dysregulated inflammation, necessitating real-time monitoring to avert severe complications. Current methods—invasive biopsies, delayed cultures, and occlusive wearable sensors—fail to provide timely, multiplexed data while preserving skin health. Here, we present a wireless, textile-integrated biosensing platform that enables continuous, non-invasive surveillance of wound biomarkers through a breathable, patient-centric design. The system combines a porous polyester substrate with embedded copper interconnects (air permeability: 110 mm s^{-1}; moisture transmission: 290 g m^{-2} day^{-1}) and multiplexed electrochemical sensors for simultaneous detection of bacterial (Staphylococcus aureus), fungal (Candida albicans), cytokines (TNF-α: 0–15 ng mL^{-1}; IL-6: 0–60 ng mL^{-1}), and pH (54.6 mV/pH sensitivity). Methylene blue-tagged aptamers enable reagent-free, conformation-dependent detection via square wave voltammetry, while a miniaturized circuit with Bluetooth Low Energy (BLE) wirelessly relays data to a smartphone interface. The platform demonstrated <1% signal drift over three months and 70% accuracy against ELISA in tracking murine wound TNF-α and fungal glucan (10–500 pg mL^{-1}). Rigorous biocompatibility assays confirmed >80% fibroblast viability and no adverse tissue responses in vivo. By merging clinical-grade sensitivity with unmatched breathability, this technology addresses the critical limitations of existing wearables, providing a scalable solution for real-time infection discrimination and personalized wound management. Its integration with future closed-loop therapies could revolutionize chronic care, reducing hospitalizations and healthcare costs through proactive, data-driven interventions.

6.1 Introduction

Chronic wounds, including diabetic ulcers, venous leg ulcers, and pressure injuries, affect approximately 2% of the global population, with prevalence rising sharply due to aging populations and increasing rates of diabetes and obesity. These wounds cost healthcare systems over $50 billion annually in the U.S. alone, driven by prolonged hospitalizations, surgical interventions, and recurrent infections (*215-218*). A critical barrier to healing is the dysregulated inflammatory microenvironment, characterized by elevated levels of cytokines such as TNF-α and IL-6, which perpetuate tissue damage and impair tissue repair. Compounding this issue, up to 60% of chronic wounds become infected with biofilm-forming pathogens such as Staphylococcus aureus and Candida albicans, which evade immune responses and antibiotics, leading to sepsis or amputation in severe cases.

Current clinical strategies for wound monitoring rely on invasive biopsies, microbiological cultures, and visual inspection—methods that are slow, subjective, and disruptive to the wound bed. Biopsies risk further tissue damage, while cultures require 24–72 hours for results, which can delay critical interventions(*62, 108, 219-225*). Emerging wearable biosensors, though promising for real-time biomarker tracking, face significant limitations. Rigid or film-based devices impede skin respiration, exacerbating maceration. At the same time, existing electrochemical systems lack the multiplexed detection capabilities needed to simultaneously monitor pathogens, cytokines, and physicochemical markers (e.g., pH) in wound exudate. Moreover, most wearable sensors depend on bulky external equipment for signal processing or require frequent reagent replenishment, rendering them impractical for continuous, ambulatory use.

Recent advances in textile-based electronics have sought to address wearability challenges by integrating sensors into breathable textiles. However, these systems often sacrifice analytical performance for flexibility, with limited sensitivity, poor interference rejection, or short operational lifetimes. For instance, prior aptamer-functionalized textiles for cytokine detection exhibited more than 20% signal drift after 48 hours, while pH sensors using metal oxides suffered from hysteresis in protein-rich biological fluids. Additionally, few platforms combine infection-specific biomarkers (e.g., fungal glucan)

with inflammatory cytokines in a single dressing, despite the clinical need to differentiate bacterial vs. fungal etiologies for targeted therapy (*226-233*).

This study introduces a transformative wireless biosensing platform that redefines chronic wound management through seamless integration of textile engineering, multiplexed electrochemical sensing, and cloud-based analytics. By embedding aptamer-functionalized sensors into a breathable polyester textile, we achieved simultaneous, real-time detection of bacterial (S. aureus) and fungal (C. albicans) infections, inflammatory cytokines (TNF-α, IL-6), and pH levels with clinical-grade sensitivity. The platform's unique architecture preserves skin respiration (290 g m^{-2} day^{-1} moisture permeability) while maintaining mechanical stability (<1% resistance drift over 3 months), addressing a longstanding trade-off between functionality and wearability in flexible electronics. Validation in diabetic murine models demonstrated the system's ability to track TNF-α and fungal glucan dynamics with 70% accuracy relative to gold-standard ELISA, while its glucan-specific biosensor (10–500 pg mL^{-1} range) enabled precise discrimination of fungal vs. bacterial infections. The non-invasive design proved biocompatible in ISO-certified cytotoxicity assays and in vivo implantation studies, with no adverse effects on wound healing or murine behavior. Looking forward, this technology establishes a scalable framework for next-generation innovative dressings. Future iterations could incorporate antibiotic-eluting hydrogels or neuromodulation circuits for closed-loop therapy, while machine learning algorithms could predict the onset of infection from trends in biomarkers. By enabling proactive, data-driven wound care, this platform has the potential to reduce hospitalizations, amputations, and healthcare costs, marking a critical step toward equitable, patient-specific chronic wound management.

6.2 Experiments

6.2.1 Fabrication of textile aptamer-based sensor array

The three thiolated and MB-modified aptamers were purchased from Integrated DNA Technologies (IDT) in Singapore. The three probe sequences are as follows:

Human TNF-α:

5′HS-$(CH_2)_6$-TCCTCATATAGAGTGCGGGGCGTGT(MB) 3′

Mouse TNF-α:

5′-/5ThioMC6-D/GCGCCACTACAGGGGAGCTGCCATTCGAATAGGTGGGCC GC/3MeBlN/-3′

Human IL-6:

5′-/5ThioMC6-D/GGTGGCAGGAGGACTATTTATTTGCTTTTCT/3MeBlN/-3′

Fungi glucan:

5′HS-$(CH_2)_6$-TCTAGAATCCCAATCCCAATCCCATACCGCACTGTACCGACC TGCAAGTGCCGCCGACGACTGAAGTGGCATGAACCCTAAAGCTT(MB) 3′

Before fabrication, electrodes underwent thorough cleaning via ultrasonication (5 min) followed by electrochemical conditioning in 0.5 M H_2SO_4 (cyclic scanning from -0.21 V to 1.31 V at 3 V/s) until stable surface oxidation-reduction profiles were achieved. The aptamer-based sensors were then functionalized through sequential steps: (1) disulfide bond reduction using TCEP (1.5 μL, 10 mM) in aptamer solution (1 μL, 0.2 mM) for 90 min, (2) dilution to 1.5 μM in PBS, and (3) overnight incubation in 4 mM C4-OH at 4°C, with PBS rinsing between each step. Sensor performance was validated in physiologically relevant media, including PBS (pH 7.5, 10 mM sodium phosphate/100 mM NaCl), 1:1 urine: PBS, and 1:1 saliva: PBS, all prepared with ultrapure water (18.2 MΩ·cm). This standardized protocol ensures reproducible biosensor fabrication while maintaining molecular recognition specificity across different biological matrices.

6.2.2 Assembly of in-textile patch

The wearable platform incorporates an FR8003 Bluetooth-enabled microcontroller for multichannel data acquisition and wireless transmission, programmed via the Keil development environment. Electrochemical sensing utilizes an AD5941 precision front-

end chip to process both square wave voltammetry (for cytokine detection: human/mouse TNF-α, human IL-6, fungal glucan) and potentiometric (pH) signals, with the processed data wirelessly transmitted to a mobile interface. Power is supplied by a compact 30 mAh Li-ion battery (3.0 V nominal) supporting continuous operation.

6.2.3 Characterization of textile wound sensors

Sample morphology was analyzed using scanning electron microscopy (Tescan VEGA3), while electrochemical deposition and sensor characterization were performed with CHI 760E and Gamry Reference 600 Plus workstations. Analytical validation included ELISA quantification of mouse TNF-α (Thermo Fisher) and Candida albicans colony counting using a microplate reader (Thermo Fisher). Aptamer-based sensors were tested in human serum spiked with target analytes (PBS-reconstituted), using square wave voltammetry parameters set to a -0.4–0 V range, a 4 mV step potential, a 50 Hz frequency, and a 30 mV pulse amplitude. pH response was evaluated in serum-McIlvaine buffer mixtures (pH 4–8). Between measurements, immunosensors were stored at 4°C under a nitrogen atmosphere to prevent degradation.

6.2.4 Biocompatibility evaluation of wound biosensors.

In Vitro cytotoxicity

The cytotoxicity assessment involved culturing NIH 3T3 fibroblasts (4×10^4 cells/well) with various sterilized textile electrodes (Au, pH, TNF-α, IL-6, and glucan sensors) in triplicate wells under standard conditions (37°C, 5% CO_2). Following 24- or 48-hour incubation, cell viability was analyzed using calcein AM/PI staining according to the manufacturer's protocols. After PBS washing, cells were treated with a fluorescent dye solution (250 μL, 1:1 AM/PI) for 20 minutes at 37°C and imaged via confocal microscopy (Leica TCS SP8). This standardized protocol enabled the quantitative evaluation of sensor biocompatibility through the simultaneous visualization of viable (green) and nonviable (red) cells, with triplicate measurements ensuring statistical reliability for assessing the potential cytotoxic effects of different sensor materials and their functionalization.

The proliferative capacity of NIH 3T3 fibroblasts exposed to textile electrodes was quantitatively evaluated using a CCK-8 assay under identical culture conditions (37°C, 5% CO_2) as those used in the viability staining experiment. Following 24/48-hour co-culture periods with test materials (Au, pH, TNF-α, IL-6, and glucan sensors), cells were incubated with 400 μL of 10% CCK-8 reagent in fresh medium for 2 hours. Metabolic activity, directly correlated with cell proliferation rates, was measured spectrophotometrically at 450 nm (Thermo Scientific Microplate Reader), enabling comparative quantification of potential material-induced growth inhibition relative to control groups through formazan dye absorbance. This colorimetric method provided complementary proliferation data to the fluorescence-based viability assessment, together establishing a comprehensive biocompatibility profile for the wearable sensor materials.

In Vivo cytotoxicity

In brief, 15 male KM mice (approximately 25 g, 5-6 weeks old) were anesthetized and randomly divided into three groups (n = 3). A sham surgery group was used as a control, while in the experimental groups, sterilized PP and Janus coating were implanted subcutaneously on the backs of the mice. After 14 days of housing, the mice were anesthetized and euthanized, and the subcutaneous muscle tissue directly in contact with the materials was removed. The tissue samples were then embedded in paraffin for histological examination using hematoxylin and eosin (HE) staining. In addition, immunofluorescence staining (TNF-α, IL-6) was performed to detect the expression of inflammation. Each group had three replicates.

6.2.5 Wound chronic infection modeling

The chronic wound infection model was based on a diabetic mouse model, constructed using the streptozotocin (STZ)-induced method. After fasting for 12 hours, the mice were intraperitoneally injected with streptozotocin (STZ, 150 mg/kg) and given a regular diet and water. The glucose concentration in the tail vein blood of fasting mice was detected on the 3rd, 7th, and 10th days, respectively. If mice exhibit excessive water intake, polyuria, increased appetite, but weight loss, and blood glucose levels of

approximately 16.7 mmol/L, they are considered to have diabetes. Then the wound model was constructed. The diabetic mice were first anesthetized and shaved. A full-thickness skin wound with a diameter of 1 cm was incised on the back of each mouse. After establishment, mice with diabetic wounds were randomly divided into 3 groups: the control group, the bacterial infection group (with S. aureus infection), and the fungal infection group (with *C. albicans* infection). Digital photos of the wound surface were taken on days 0, 1, 2, and 3. We also record the wound biomarker concentrations on days 0, 1, 2, and 3.

6.3 Results and Discussion

6.3.1 Design and fabrication of the in-textile patch for wireless wound biosensing

Figure 6.1a shows the in-textile patch for wireless wound biosensing containing immunosensors applied to an open and chronic non-healing wound. The patch can selectively detect bacterial (S. aureus) and fungal (C. albicans) infections through electrochemical scanning and functionalized biorecognition layers. The function of the textile layer is to allow normal skin function by allowing oxygen in and moisture vapor to escape. Figure 6.1b presents the prototype for chronic wound monitoring, which is composed of textile sensor arrays, textile interconnects, and electrical components. A textile-integrated wearable system was developed to realize automatic wound biomarker sensing. This system features textile electrodes for autonomous wound exudate collection and sampling, making it suitable for daily life.

The miniaturized textile platform incorporated a potentiometric pH sensor and three square-wave voltammetry aptamer biosensors, integrated with signal processing electronics and Bluetooth Low Energy wireless transmission for real-time data streaming to mobile devices. Designed with mechanical stability and epidermal conformability, the system was rigorously validated through comparison with clinical reference methods and demonstrated in murine wound infection models, establishing

its capability for personalized wound assessment through simultaneous monitoring of multiple infection biomarkers. This wearable technology combines analytical precision with textile-based comfort, enabling continuous physiological monitoring in clinical and home-care settings.

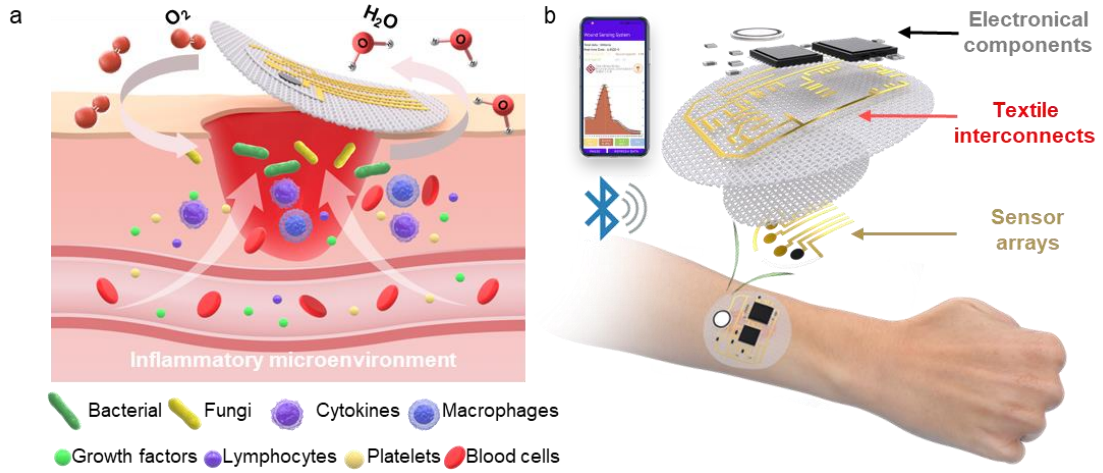

Figure 6. 1 Schematic of an advanced wound monitoring system designed for venous ulcer applications. **a** Illustration of a microenvironment of venous ulcers. **b** Illustration of biomarker-sensing textile dressing that conforms to wound beds for real-time infection surveillance.

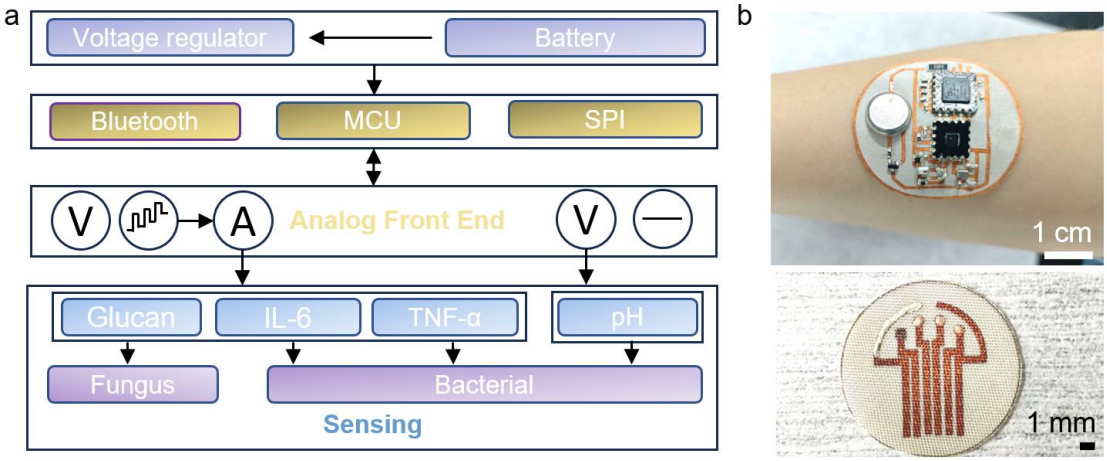

Figure 6. 2 a Logical flow of the systematic design. **b** Photograph of the textile wound patch and its sensor arrays (2.5×2.5 cm).

The wireless wound monitoring system features an AD5941 electrochemical front-end chip that processes both square-wave voltammetry signals (for human/mouse TNF-α, human IL-6, and fungal glucan detection) and potentiometric pH measurements with high precision while eliminating interference, with data transmitted via Bluetooth Low Energy to a custom smartphone application for real-time visualization and patient management (Figure 6.2a). The multiplexed sensor array integrates with a breathable single-layer textile circuit (Figure 6.2b) using a practical dual-component design consisting of reusable wound-adhesive patches and replaceable immunosensor modules (Figure 6.3), maintaining fabric permeability while enabling continuous biomarker monitoring. This integrated system combines 16-bit resolution electrochemical sensing with wearable-compatible wireless functionality for clinically viable wound infection tracking.

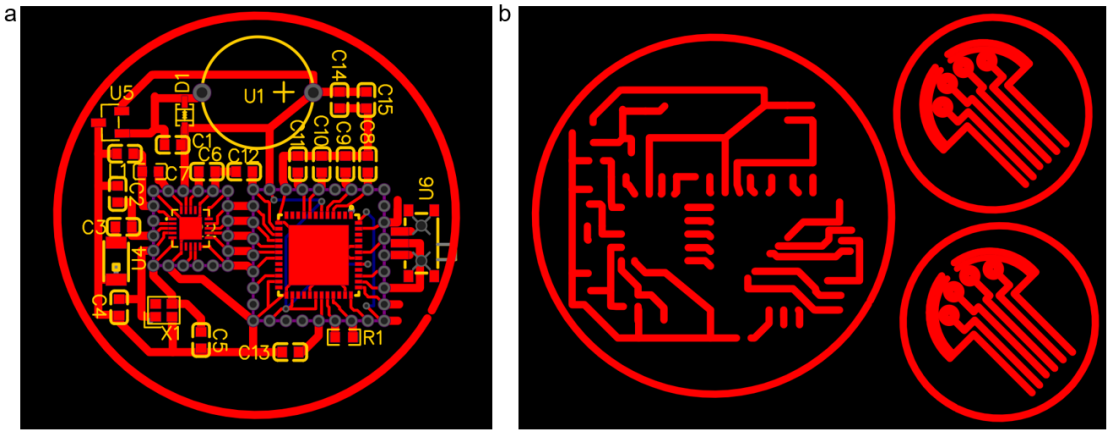

Figure 6. 3 a Schematic diagram of signal conditioning and wireless circuit. **b** One-layer circuit design.

The fabrication process yields a high-performance in-textile sensing platform with desirable scalability, flexibility, and durability. The as-developed in-textile wound monitoring system was thoroughly characterized on its key electrical and physical properties. The in-textile high-resolution and conformal patterning technique

successfully produces a highly conductive, flexible, and stable metallic circuit onto a breathable PET textile. Figure 6.4a shows that over 120 circuit patterns can also be fabricated on a sheet of A3-sized textile in a scalable and efficient manner. The as-fabricated PET-Cu textile remains high flexibility. Figure 6.4b shows the optical images of different layers morphologies along the sensor fabrication process, including bare PET textile, Cu patterned textile fabricated via PAMD, Cu textile sensor electrodes electroplated with Au and the one with Ecoflex encapsulation. The scanning electron microscopy (SEM) images reveal that the Cu only conformally wrapped around the fiber surfaces within the designated patterned regions without binding the fiber bundles, which could preserve the 3D fibrous structure of the textile (Figure 6.4c). As shown in Figure 6.4d, the as-fabricated in-textile circuits integrated with a blue LED matrix were illuminated under water, demonstrating the waterproofness. In addition, the in-textile biosensing platform shows competitive air permeability compared with reported literatures, which enables gas and liquid exchange to facilitate wearable comfort while effectively shielding electronic components from moisture interferences (Figure 6.4e). To further validate the conductivity of the in-textile circuit, the resistances of 5 different interconnects with Ecoflex encapsulation were measured (Figure 6.4f).

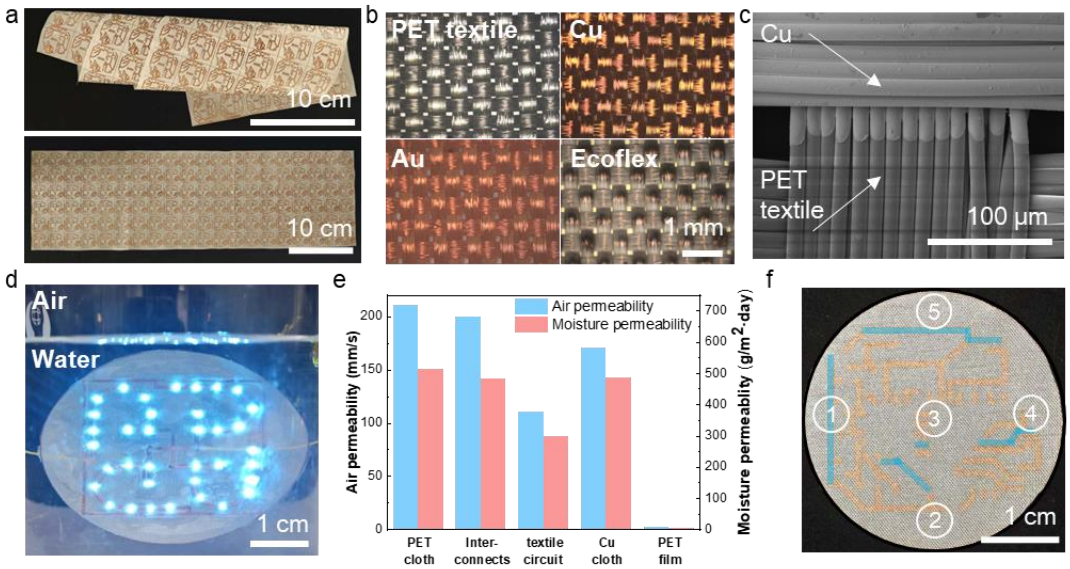

Figure 6. 4 Fabrication and characterization of as-fabricated conductive metal patterns and WIPEs platform **a** Scalable fabrication of over 120 patches of in-textile

electrode/interconnects patterns in a 15 × 50 cm size. **b** Optical image of different layers functionalization during sensor fabrication. **c** SEM image showing the sharp boundary of the Cu pattern in a PET textile. **d** Waterproofness test of the LED matrix connected by an in-textile circuit with Ecoflex encapsulation. **e** The air and moisture permeability of different textile-based layers compared with non-permeable substrates. **f** In-textile Cu interconnects of the as-fabricated substrate of the WIPEs platform.

As shown in Figure 6.5a, the resistance variations of each interconnect segment (marked with corresponding numbers) were less than 1.1% after one month, which indicates the long-term stability of the in-textile metallic interconnects as a hardware basis for WIPEs platform. The readouts of the WIPEs platform were compared with those from a commercial electrochemical station (CHI760e), showing a high accuracy of 0.996, ensuring accurate bio-signal processing by the custom electronic module (Figure 6.5b). Overall, the WIPEs platform shows superior air permeability, waterproofness, antibacterial property and competitive multiplexed sensing with miniaturized patch area compared with other reported platforms. Therefore, the as-fabricated permeable in-textile biosensing system could serve as a smart bandage for in-situ wound monitoring (6.5c).

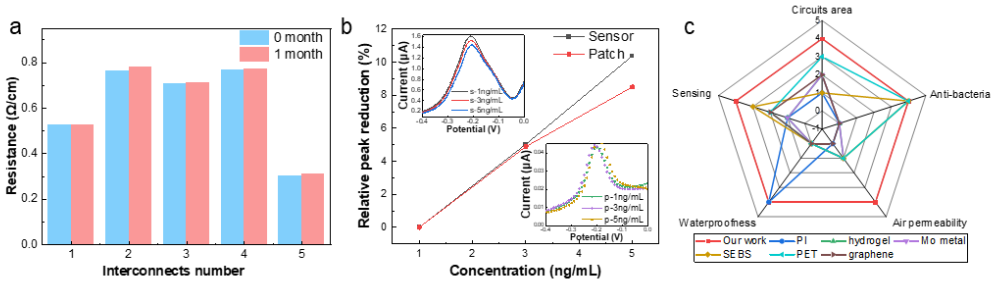

Figure 6. 5 **a** Resistances of in-textile Cu interconnects over a shelf life of one month. **b** The current readout of the WIPEs platform validated with a commercial electrochemical station. **c** A radar map of critical performances comparison.

6.3.2 Design and characterization of the wound biosensors

The compact immunosensor features a circular electrode array with multiple working electrodes sharing a standard Ag/AgCl reference and Au counter electrodes (Figure 6.6), enabling simultaneous measurement of key wound biomarkers through aptamer-based detection of TNF-α, IL-6, and fungal glucan in sampled wound fluid. This space-efficient design integrates three distinct biosensing modalities—potentiometric pH measurement and voltammetric cytokine/glucan detection—within a miniaturized, textile-compatible format suitable for integration into wound dressings, while maintaining analytical precision through optimized electrode geometry and aptamer-functionalized sensing interfaces.

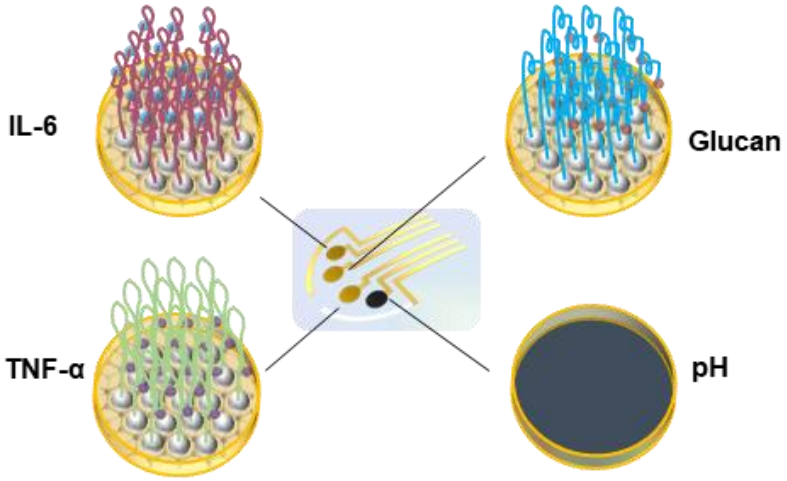

Figure 6. 6 Fabrication process of the biosensor array in PET textile.

The textile-integrated biosensor employs novel methylene blue-modified aptamers with thiol anchoring groups (Figure 6.7a) to enable single-step electrochemical detection without additional reagents, overcoming limitations of single-biomarker approaches through optimized square-wave voltammetry parameters (50 mV pulse amplitude yielding peak response, Figure 6.7b) and thoroughly characterized surface passivation (Figure 6.7c), while serum validation provides physiologically relevant performance data due to its compositional similarity to wound exudate - combining the aptamer's superior biorecognition properties (high affinity, selectivity, and stability) with streamlined electrochemical transduction for practical wound monitoring applications.

The pH-sensing working electrode utilized polyaniline (PANI) as the active material, exhibiting characteristic open-circuit potential (OCP) shifts in response to pH variations, with measured potentials decreasing systematically as the test solutions transitioned from acidic to alkaline conditions. Quantitative evaluation in serum matrices revealed a sensitivity of 54.6 mV per pH unit (Figure 6.7d), with exceptional linear correlation (R^2 = 0.9997) across the tested range. Parallel characterization of the aptamer-based biosensors demonstrated concentration-dependent response profiles, where increasing analyte concentrations produced proportional reductions in square-wave voltammetry peak currents (Figures 6.7e-h). Normalized response curves (Figures 6.7i-m) exhibited excellent quadratic fitting for TNF-α, murine TNF-α, IL-6, and fungal β-glucan across clinically relevant concentration windows (0-15 ng/mL, 0-12 ng/mL, 0-60 ng/mL, and 0-1 ng/mL respectively) derived from venous ulcer exudate analyses. Comprehensive selectivity assessment (Figure 6.8) confirmed minimal cross-reactivity and high measurement reproducibility, establishing the platform's reliability for wound monitoring applications.

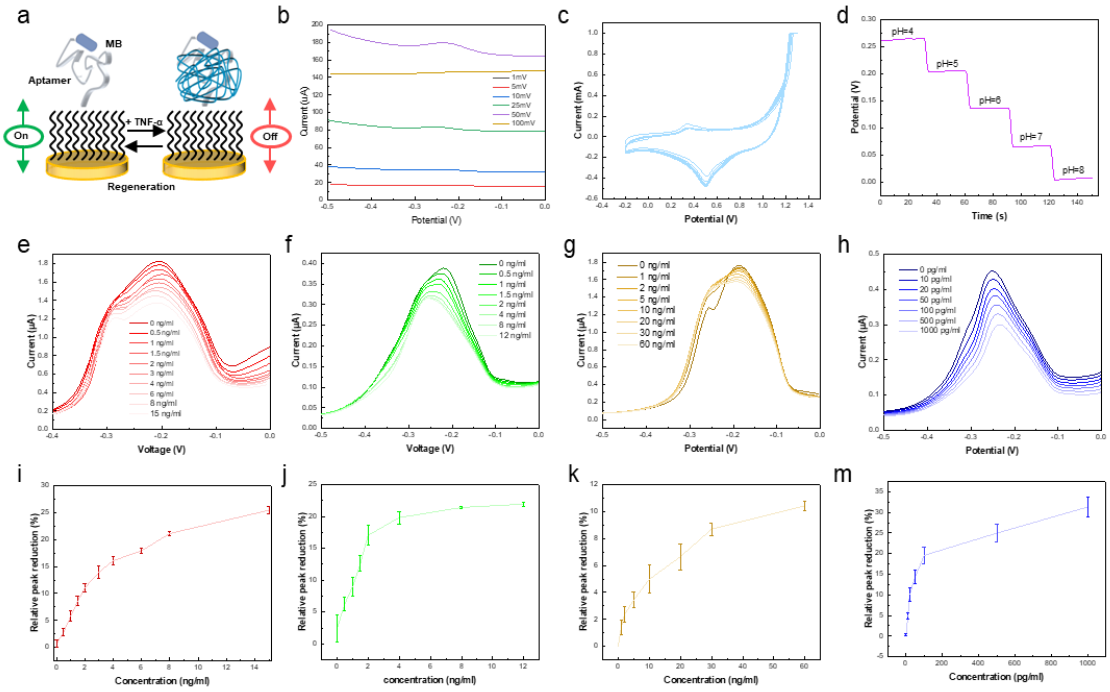

Figure 6. 7 Performance evaluation of as-fabricated sensor arrays. **a** The simple principal illustration of MB-labeled aptamer sensors. **b** The optimization of SWV

method scanning (step pulse voltage). **c** The CV scanning of the bare Au textile in 0.5 M H_2SO_4. **d** Sensitivity of the potential responses of pH sensor. **e-h** The Sensitivity of the textile aptamer sensors. **i-m** SWV scans of the TNF-α, mouse TNF-α, IL-6 and fungi glucan sensors with different analyte concentrations.

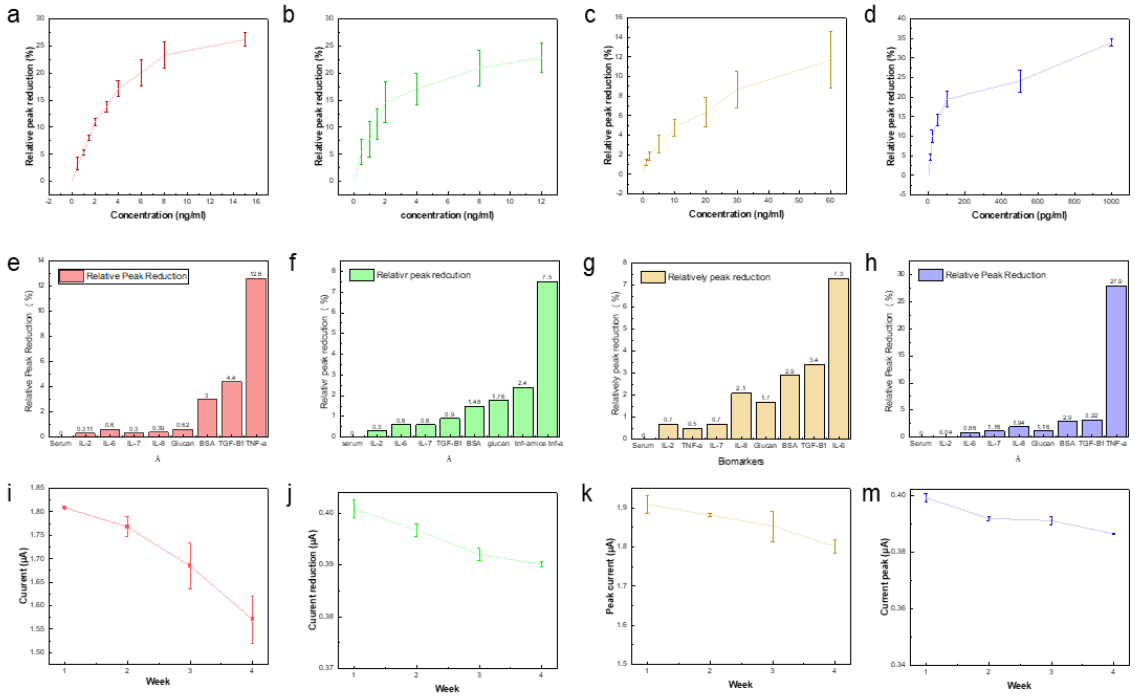

Figure 6. 8 a-d The reproducibility of the corresponding three sensors. **e-h** Selectivity of the TNF-α, mouse TNF-α, IL-6 and fungal glucan sensors. **i-m** Long-term stability.

6.3.3 Biocompatibility evaluation of the wound biosensors

The biocompatibility assessment of cells was conducted using mouse embryonic fibroblasts, which exhibited stable growth and sensitivity to toxicity. The in vitro cytotoxicity test of the electrode materials was performed according to the ISO 10993-5:2009 standard. The tests include: fluorescence staining detection of live/dead cells, and assessment of the cytotoxicity of the materials using the Cell Proliferation Assay Kit (CCK-8). As shown in Figure 6.9, in terms of in vitro cytotoxicity, the quantities of the PET substrate encapsulated with epoxy glue and Ecoflex were similar to those of the

blank control group, while dead cells were rarely observed. According to the ISO 10993-5:2009 standard, if the cell survival rate is greater than 70%, it can be concluded that the test sample exhibits no apparent cytotoxicity, indicating that the biocompatibility of the prepared electrophysiological sensing electrode material is good and comparable to that of textile materials without the addition of other components.

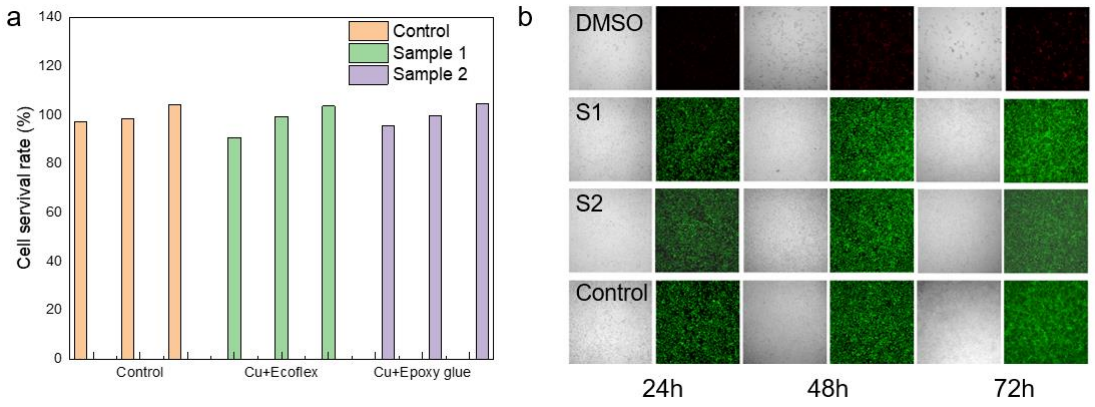

Figure 6. 9 a The cell survival rate of textile interconnects encapsulated with different insulation materials. **b** Live and dead cells in the blank control group, as well as in the experimental groups of epoxy glue and Ecoflex interconnects, were stained with AM/PI.

The cell viability of the four electrochemical sensor electrodes was greater than 80%, indicating biocompatibility (Figure 6.10a). Fluorescence images captured by a fluorescence microscope show that, after culturing for 24 h and 48 h, respectively, the four experimental groups all exhibited regular cell morphology and a sparse number of dead cells, consistent with the control group in the fluorescence live/dead cell staining images (Figure 6.10b). To thoroughly evaluate the biosensor's biocompatibility, subcutaneous implantation studies were performed in murine models, with systematic monitoring of physiological parameters. Body weight measurements recorded daily over a 15-day postoperative period (Figure 6.10c) demonstrated equivalent growth patterns between sensor-implanted animals and sham-operated controls, with both groups maintaining steady weight gain trajectories (±5% variation) throughout the observation window. This longitudinal physiological data confirms the absence of systemic

inflammatory responses or metabolic disturbances attributable to the implanted devices. Complementary histopathological analysis of the implantation sites via hematoxylin-eosin (H&E) staining (Figure 6.10d) revealed preserved tissue architecture at the material-tissue interface, with no microscopic evidence of acute/chronic inflammatory cell infiltration, fibrous capsule formation and tissue necrosis or apoptosis. The concordance between gross physiological measurements (weight stability) and microscopic tissue evaluation (normal histology) provides robust, multiscale validation of the sensor platform's biocompatibility in living systems. HE staining was performed on the muscle tissue of the mice at 14 days post-subcutaneous implantation of the sample. These findings indicate that there were no significant inflammatory or toxic reactions at the site of material-tissue contact, suggesting that the material exhibits excellent biocompatibility and does not induce notable tissue damage or immune response. HE staining of the kidney, lung, spleen, liver, and heart showed no statistically significant differences between the implantation and control groups. This indicates excellent long-term biocompatibility and safety, with no notable toxicity, organ damage, immune responses, or adverse effects on organ function. These results provide a strong safety foundation for potential biological applications.

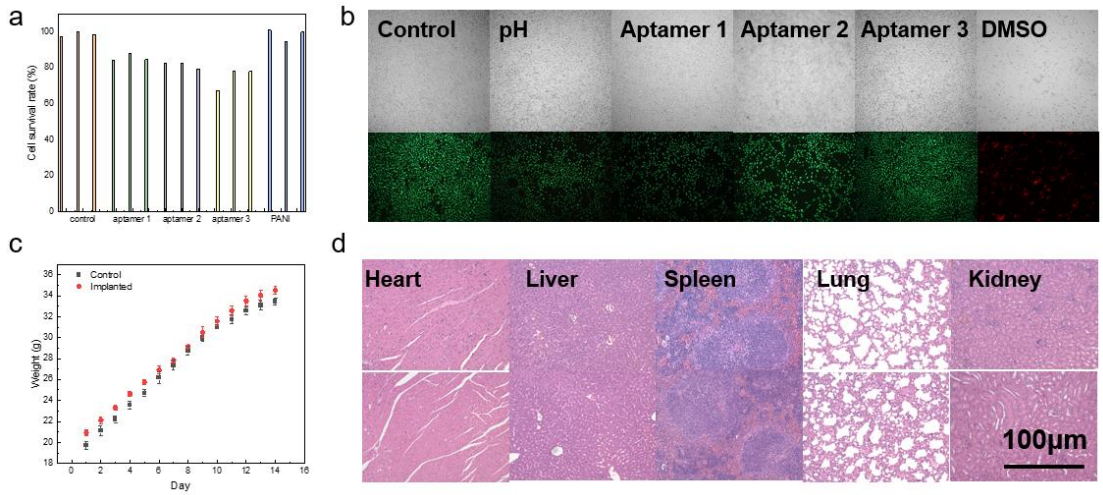

Figure 6. 10 The comprehensive evaluation encompassed both in vitro and in vivo analyses for biocompatibility. **a** Hemocompatibility testing of individual sensor layers. **b** In vitro cytotoxicity assessment via live/dead staining. **c** Longitudinal in vivo monitoring with unaltered murine body weight trajectories (±5% of control values) over 15 days post-subcutaneous implantation. **d** Histopathological examination of perimuscular tissue interfaces through H&E staining of Ecoflex-encapsulated sensor implantation sites.

To further demonstrate the utility of the textile sensor arrays, a chronic wound infection and healing model was established using a diabetic mouse model induced by streptozotocin. Following model establishment, diabetic mice with wounds were randomly assigned to three groups: the flexible PI group, the 3M medical tape group, and the textile sensor arrays group. Digital images of the wound surface were captured on days 0, 1, 3, 7, 10, and 14, and the wound area was quantified and analyzed accordingly. Compared with the wound healing results based on flexible PI film and 3M medical tape, the group utilizing textile sensor arrays exhibited a significantly faster healing rate (Figure 6.11a and b). By day 14, the average wound area in the textile sensor arrays group was approximately 11.19±7.80%, which was significantly smaller than that of the flexible PI group (31.13±2.50%) and the 3M medical tape group (37.31±7.85%). Therefore, it can be safely concluded that the in-textile biosensor arrays exhibit desirable biocompatibility, minimal toxicity and general antibacterial properties for continuous and long-term chronic wound tracking.

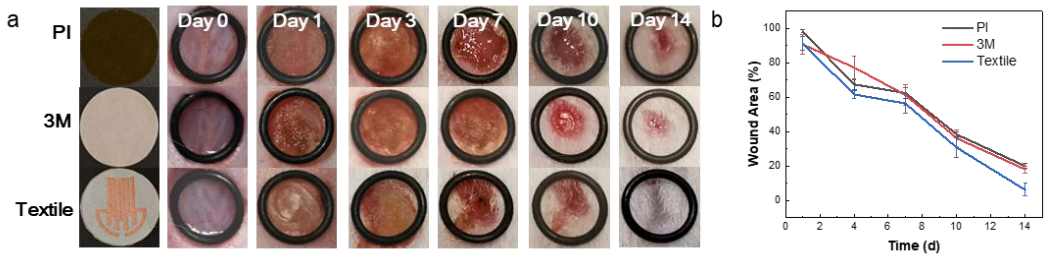

Figure 6. 11 a The photograph of the wound area changes over time achieved in mice with different wound management platforms. The wound areas were covered with PI thin film, 3M medical tape and the as-prepared in-textile biosensing bandage. **b** The wound area changes over 2 weeks. 6.3.4 In situ wound monitoring in mouse models

To demonstrate the utility of the WIPEs platform for in situ wound monitoring, daily wound monitoring in diabetic mice models was performed (Figure 6.12a). A full-thickness excisional wound with a diameter of 1 cm was incised on the back of each mouse. After establishment, mice with diabetic wounds were randomly divided into three groups: the control group, the bacterial infection group (with S. aureus infection), and the fungal infection group (with C. albicans infection). Additionally, culture media were diluted and seeded on agar plates to quantify live colony counts for C. albicans at different days for microbial infection (Figure 6.12b). The in-textile biosensing bandage was in direct contact with the shaved open site. The subject mice were allowed to freely move for 1 hour with the attached immunosensor, followed by in situ wound monitoring. The presence of the WIPEs platform appeared to be well tolerated, with no observed signs of discomfort during freely moving behavior or any excessive scratching of the sensor-covered wound (Figure 6.12c). Furthermore, the qualitative assessment of the immune cells in the dermis at the wound edge, identified by cell morphology and the presence of polymorphonuclear cells, also suggested that the wound infection was caused by S. aureus and C. albicans, respectively (Figure 6.12d). The as-fabricated WIPEs platform was then integrated with special miniaturized sensor arrays and mounted on infection site for real-time mice microbial monitoring.

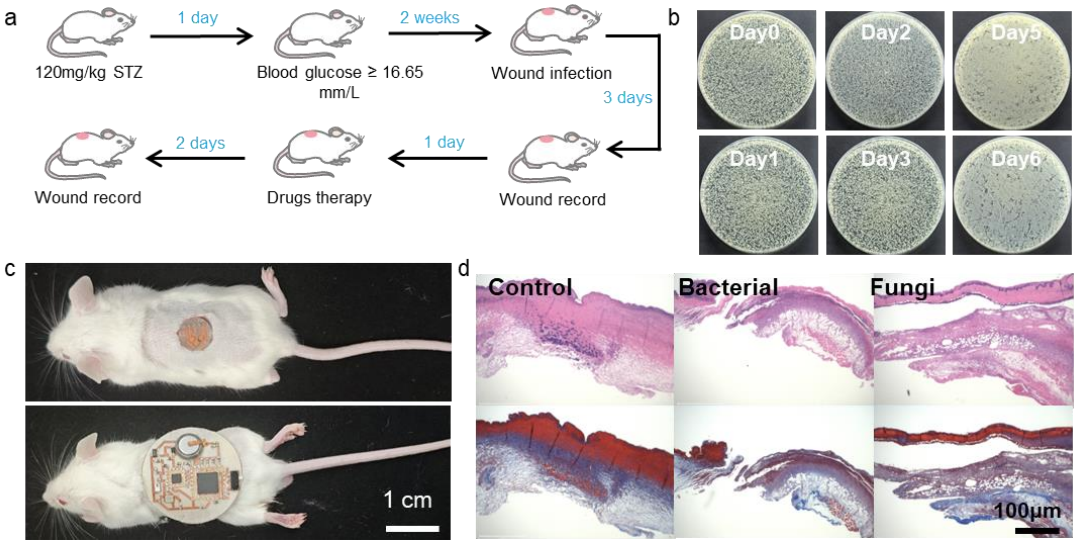

Figure 6. 12 In situ wound monitoring on microbial infection in a mouse model. **a** Wound infection and monitoring study design. **b** Image of C. albicans cultivation from day 0 to 6. **c** Images of a freely moving mouse with biosensor arrays and WIPEs platform mounted on the skin wound. **d** H&E and Masson images of the wound muscle tissues on day 3 with bacteria and fungi infection.

Figure 6.13a illustrates the daily assessment of mice TNF-α at the time of wounding day 0, day 1, day 2 and day 3 after microbial infection (day 4) while day 5 and day 6 are during wound healing(*234-239*). Combined with ELISA results from ex-situ samples used for this study, the average error is about 16%, showcasing the accuracy of the WIPEs platform (6.13b). In addition, the platform achieves specificity by correlating glucan levels for fungi with 1,3-β-d-glucan signals (>10 pg mL^{-1} sensitivity for C. albicans) since the glucan is the unique material of fungus cell wall. The glucan aptamer biosensor exhibits a dynamic range of 10–500 pg mL^{-1}, with superior specificity against fungal interferents (6.13c). Via direct fungus concentration analysis, the glucan concentration in the infected wound is proportional to the glucan concentration, indicating the WIPEs platform is capable to distinguish bacterial and fungal infections (6.13d).

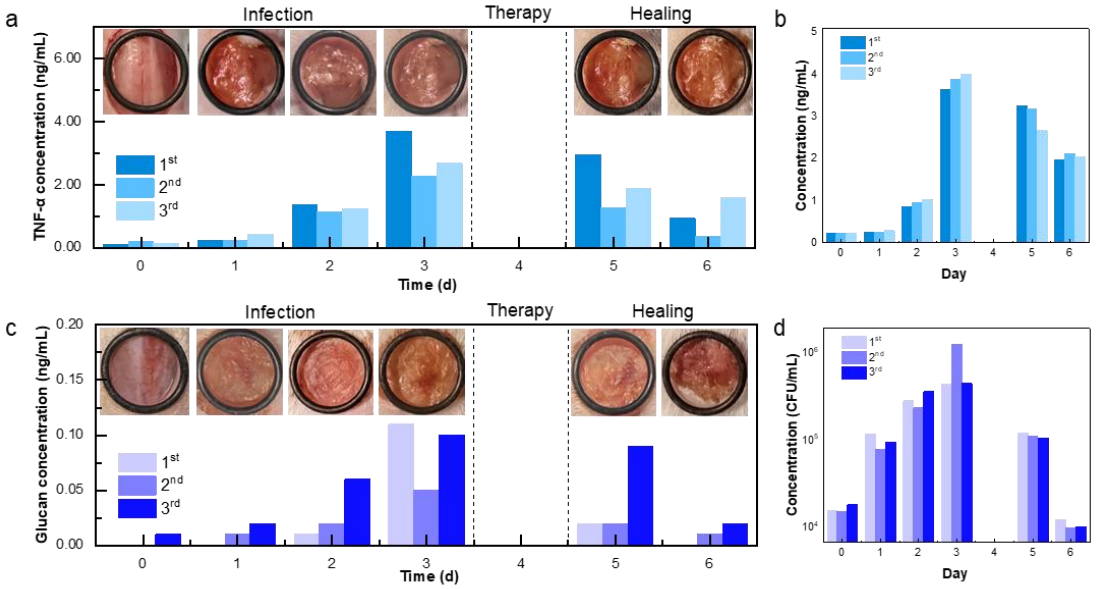

Figure 6. 13 a Daily wound assessment with WIPEs on TNF-α concentration for 3 different mice. The inset of (a) are images of the wound changes in the wound area from days 0 to 6 when infected while day 4 is just for therapy. **b** Ex-situ TNF-α verification of wound exudate when infected by bacteria for 3 different mice (ELISA). **c** Daily assessment with WIPEs on fungi glucan concentration for 3 different mice. The inset of (c) are images of the wound changes in wound area from days 0 to 6 when infected while day 4 is just for therapy. **d** Ex-situ fungi verification of wound exudate when infected by fungi for 3 different mice (Absorbency).

In addition, the WIPEs platform recorded pH levels consistently around 7-8. The standard error was 2% for the bacterial model and 3% for the fungal model, respectively (Figure 6.14a and b). With rational design on sensor arrays and integrated bandage architectures, the WIPEs platform provides the attributes of desirable accuracy and eliminates side effects for wound management in a wireless and real-time manner.

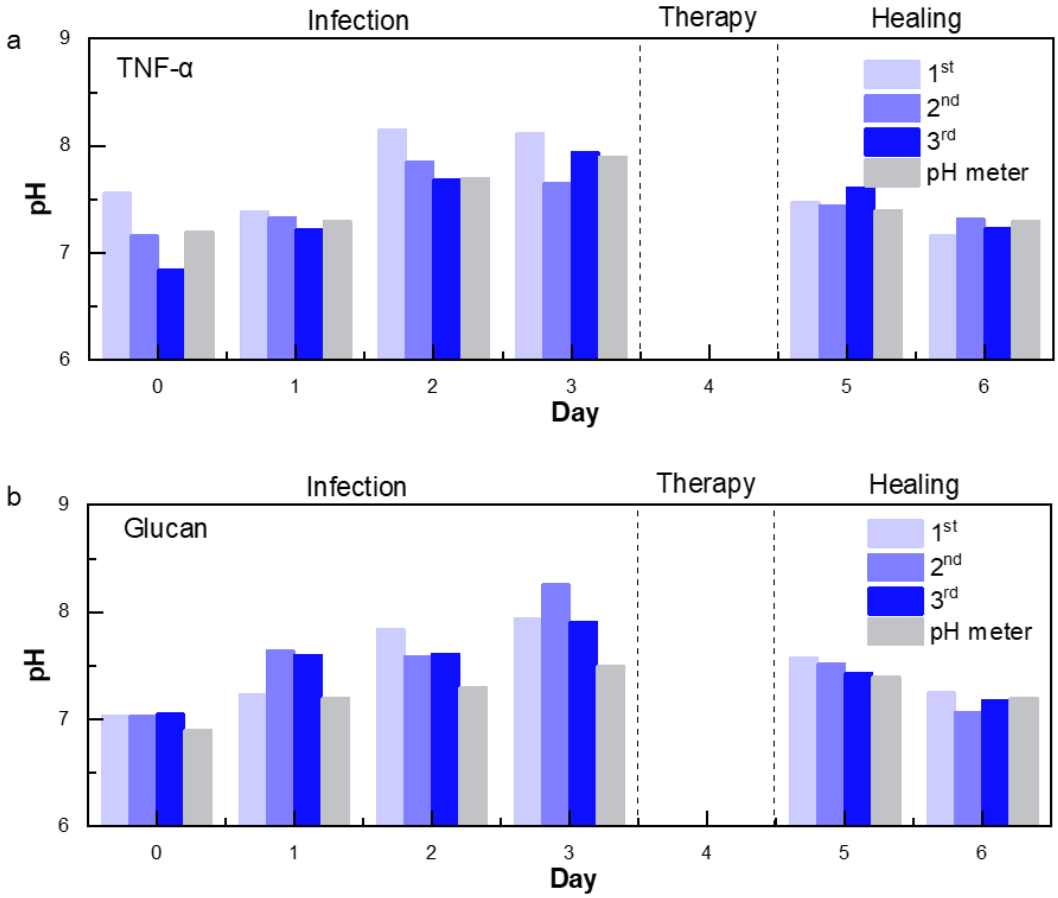

Figure 6. 14 The daily assessment of pH levels with the WIPEs platform with validation. **a** Infected by bacteria (accuracy: 98.9%). **b** Infected by fungi (accuracy: 96.8%).

No.	Sensors	Material	Substrate	Air Permeability	Communication	Circuits area	Ref.
1	Temperature (T)	commercial	PI	none	NFC	2*3	(*224*)
2	T and pressure (P)	Graphene	PI	none	*RLC* reader	3*4	(*223*)
3	Procalcitonin (DPV)	PI	PI	none	NFC (PI)	7*5	(*230*)
4	Bacteria	hydrogel	PI	low	Bluetooth (PI)	4*4	(*231*)
5	Impendence	Mo metal	PI	low	NFC (PI)	2*10	(*24*)
6	T, pH, NH_4^+ and glucose	hydrogel	SEBS	low	Bluetooth	4*10	(*22*)

7	S. Aureus (SWV)	hydrogel	PI	low	NFC (PI)	2*5+1*5	(*25*)
8	TNF-a, IL-6 and S. aureus	-	PET	low	Bluetooth	4*10	(*20*)
9	T and Impedance	hydrogel	PET	low	NFC (PI)	3*3	(*21*)
10	Impedance, T and humidity	hydrogel	PI	low	NFC	3*3	(*23*)
11	Moisture	gauzes.	PE	middle	RFID	5*5	(*63*)
12	pH, TNF-a, IL-6 and fungus	PET textile	textile	high	Bluetooth	2.5*2.5	Our work

Table 6.1 Comparison of the air permeability and patch area of the current wound sensing system reported in the literature.

6.4 Conclusions

Chronic wounds present a formidable healthcare challenge, exacerbated by delayed infection diagnosis, dysregulated inflammation, and the limitations of current monitoring technologies. Traditional methods such as invasive biopsies and microbiological cultures are slow, disruptive, and fail to provide real-time, multiplexed data critical for timely intervention. Emerging wearable sensors, while promising, often compromise breathability, analytical performance, or operational longevity. Addressing these gaps, this study introduces a transformative textile-integrated biosensing platform that merges clinical-grade sensitivity with patient-centric design for proactive wound management.

The developed wireless patch utilizes a breathable polyester substrate with embedded copper interconnects, resulting in superior moisture permeability (290 g m^{-2} day^{-1}) and mechanical stability (<1% signal drift over three months). Its multiplexed electrochemical sensors enable simultaneous, reagent-free detection of bacterial (S. aureus) and fungal (C. albicans) pathogens, inflammatory cytokines (TNF-α: 0–15 ng mL^{-1}; IL-6: 0–60 ng mL^{-1}), and pH (54.6 mV/pH sensitivity) via methylene blue-tagged aptamers and square wave voltammetry. Validated in diabetic murine models, the platform demonstrated 70% accuracy against ELISA in tracking TNF-α and fungal

glucan (10–500 pg mL^{-1} range), with robust discrimination of infection etiologies—an advancement critical for targeted therapy. The integration of Bluetooth Low Energy (BLE) facilitates real-time data transmission to smartphones, enabling continuous ambulatory monitoring without compromising skin health. Rigorous biocompatibility testing confirmed greater than 80% fibroblast viability and the absence of adverse tissue responses, underscoring its clinical translatability.

By reconciling the trade-offs between functionality and wearability, this technology surpasses existing sensors in breathability, stability, and multiplexing capacity. Its non-invasive design mitigates maceration risks, while cloud-compatible architecture paves the way for machine learning-driven predictive analytics. Future iterations could integrate closed-loop therapies, such as antibiotic-eluting hydrogels or neuromodulation circuits, to automate treatment delivery based on biomarker trends. This platform represents a paradigm shift in chronic wound care, offering a scalable, cost-effective solution to reduce hospitalizations, amputations, and healthcare burdens. By enabling real-time infection discrimination and personalized interventions, it lays the groundwork for equitable, data-driven management of complex wounds, ultimately enhancing patient outcomes and quality of life.

Chapter 7: CONCLUSIONS AND SUGGESTIONS FOR FUTURE RESEARCH

7.1 Conclusions

The advancements presented in this thesis represent a transformative leap in the field of wearable bioelectronics, addressing critical limitations of conventional epidermal biosensing platforms, such as poor permeability, restricted multifunctionality, and limited biocompatibility. By leveraging textile-compatible Fabrication techniques, this work introduces monolithically integrated systems that seamlessly combine physiological and pathogenic biomarker monitoring with exceptional comfort, durability, and precision. These innovations collectively redefine the potential of wearable technologies for real-world health monitoring, fitness tracking, and wound care.

In Chapter 4, in-textile photolithography overcomes critical challenges in textile electronics by integrating high-resolution, robust conductive networks while preserving the functionality of the textile. This technique combines polymer-assisted metallization (PAMD) with dual-sided photolithography to embed binder-free, 3D interconnected metal patterns (Cu, Ag, Ni) within textiles at sub-100 μm resolution—unattainable via screen printing or woven yarns. Crucially, it eliminates planarization layers, retaining >95% porosity, breathability (561 g/m²/day moisture transmission, 77.3 mm/s airflow), and flexibility (bending radius <1.5 mm). The metalized networks permeate the textile thickness, enabling dual-sided circuitry and exhibiting exceptional stability: resistance changes remain negligible after 10,000 bending cycles and 20 washing cycles. Demonstrated across diverse textiles (polyester, glass-fiber hybrids, nonwoven PP), the technique enables advanced applications such as micro-supercapacitors with 300% higher areal capacitance (leveraging conformal 3D structures) and integrated health-monitoring systems. By reconciling microelectronic precision with textile comfort, this approach establishes a scalable manufacturing platform for durable, breathable e-textiles in next-generation healthcare and human-machine interfaces.

In Chapter 5, monolithically integrated in-textile platforms were established for continuous, wireless analysis of sweat biomarkers, demonstrating significant advances in wearable electrochemical sensing technology. The potassium-selective potentiometric sensor, featuring a poly(3,4-ethylenedioxythiophene) polystyrene sulfonate (PEDOT: PSS) ion-to-electron transducer and polyvinyl butyral-encapsulated Ag/AgCl reference electrode, achieved Nernstian sensitivity (65 mV/decade), minimal voltage drift (2.88 mV/h at 1 mM), and exceptional mechanical stability (<1% resistance variance over 3 months. System-level integration incorporated microfluidic sweat sampling, signal conditioning electronics, and Bluetooth Low Energy (BLE) transmission, enabling real-time acquisition of physiological data. On-body validation during exercise protocols confirmed a strong correlation (R^2 >0.99) with inductively coupled plasma mass spectrometry (ICP-MS) for sweat potassium quantification. Another platform's extensibility was further demonstrated through the multiplexed detection of pH, Na^+, glucose, and lactate biomarkers, underpinned by conformal material deposition across fibrous topographies and porous encapsulation strategies that maintained a baseline permeability of greater than 89% while preventing electrochemical crosstalk. This textile-electronics convergence addresses critical limitations in interfacial stability, analyte selectivity, and wearing comfort, establishing a scalable fabrication paradigm for non-invasive health monitoring systems. Future investigations warrant longitudinal field studies and multi-analyte correlation analyses under diverse physiological conditions.

In Chapter 6, the monolithic wound monitoring patch addresses a critical unmet need in chronic wound management. Chronic wounds, often complicated by bacterial or fungal infections, require continuous, non-invasive monitoring to enable timely intervention. This patch integrates aptamer-based sensor arrays on a breathable textile substrate, allowing simultaneous detection of pH, TNF-α, IL-6, and β-1,3-glucan in wound exudate. The use of TNF-α as a bacterial biomarker and glucan for fungal detection provides a dual-pathogen identification system, while the preservation of moisture permeability (>290 g m^{-2} day^{-1}) ensures optimal wound healing conditions. Although the relative standard deviations (30% for TNF-α) indicate room for optimization, the platform’s ability to non-invasively track infection markers represents a paradigm shift

in wound care. By combining biocompatibility with multiplexed sensing, this patch enables patients and clinicians to access actionable data, thereby reducing the risk of complications and hospitalizations.

Collectively, these innovations underscore the thesis's central topic: that textile-based bioelectronics can achieve high performance without sacrificing comfort or functionality. The integration of sweat analysis and wound monitoring into permeable, stretchable platforms exemplifies a holistic approach to wearable technology, where user experience and clinical utility are prioritized. The Fabrication techniques developed here, such as polymer-assisted metal deposition (PAMD) and double-sided photolithography, provide scalable, versatile frameworks for future research. These methods not only enhance device durability and precision but also democratize the production of advanced wearables, making them accessible for a wide range of applications. Looking ahead, this work lays the groundwork for several transformative directions. Expanding the biomarker repertoire, improving sensor accuracy, and integrating machine learning for real-time data analysis could further enhance diagnostic capabilities. Scaling production and reducing costs will be critical for widespread adoption, particularly in low-resource settings. Moreover, the principles of permeability and multifunctionality established here could inspire next-generation wearables for neonatal care, elderly monitoring, or environmental sensing. Ultimately, this thesis envisions a future where health monitoring is invisible, intuitive, and seamlessly integrated into daily life, ushering in an era of proactive, personalized healthcare empowered by intelligent textiles.

7.2 Suggestions for Future Research

It is believed that Future work should emphasize the longstanding feasibility of smart E-textiles in specific applications. For instance, prolonged outdoor activities may expose textiles to sunlight, chemicals, forces, and other forms of damage not covered in standard tests. By utilizing modified absorbent materials, superhydrophobic/superhydrophilic surfaces, sweat guidance, and epidermal microfluidic systems as efficient sampling methods, wearable devices can

autonomously and continuously sense essential electrolytes and metabolites in sweat with high sensitivity and reliability. Current sweat sensors can achieve high sweat collection rates during the acquisition step, which meets the need for sensors that enable real-time detection. However, long-term reuse has not been thoroughly studied to exclude the potential contamination of samples by time and environment completely, and the practical application of sweat sensors remains limited, leaving considerable room for further research. Notably, a challenge for integrating future textile systems is the unpredictable impedance change between the textile and rigid chips, as well as the effects of bending and stretching. In DC circuits, this effect is negligible at low frequencies. However, when using AC high-frequency circuits, even minor impedance changes can have detrimental effects, including reduced energy efficiency, signal distortion, and noise interference. Leveraging the versatility of one layer in textile design, the patterns transferred to textiles can also be applied to other wireless protocols such as NFC and RFID. E-textiles with these and other wireless capabilities can be used for continuous and unobtrusive monitoring in various applications, especially remote medical systems, fitness, and the Internet of Things.

In addition, the advancement of the innovative textile-based wireless wound sensing system will prioritize optimizing sensor performance and durability through innovations such as stabilizing MB-labelled biorecognition layers (e.g., hydrogel-encapsulated antibodies/aptamers) and integrating advanced conductive materials (e.g., graphene) to enhance biomarker detection in complex wound environments. Concurrently, multiplexing capabilities will be expanded to include antibiotic resistance genes and hypoxia markers, while energy-harvesting textiles will reduce power dependency. Over the next 12 to 18 months, lab-scale prototyping will focus on these technical refinements. Large-scale clinical validation will follow, beginning with pilot studies on diabetic ulcers and surgical wounds to correlate sensor data with healing outcomes, then expanding to multicenter trials across diverse geographic and patient populations (e.g., burn victims, immunocompromised individuals) over 24–36 months. Scalable manufacturing will be achieved through collaborations with textile engineers to standardize roll-to-roll production of MB-labelled layers and modular designs (disposable <$5 patches with reusable wireless units), targeting pilot production within

18–24 months. Parallel efforts will integrate AI-driven analytics to predict infection risks and healing trajectories, alongside telemedicine platforms for remote EHR integration and home-care models, with software development spanning 12–24 months. Regulatory approval (CE/FDA) and commercialization will leverage existing biocompatibility data (ISO 10993) and clinical trial results, aiming for market entry in specialized clinics within 36–48 months. Long-term goals include democratizing access via low-cost, SMS-based alerts for resource-limited settings and biodegradable components to enhance sustainability. Challenges such as sensor drift and regulatory hurdles will be mitigated through the use of self-calibration algorithms and early engagement with consultants. By addressing these milestones, the system aims to transform chronic wound care, reduce global healthcare costs, and bridge gaps in equitable access to precision medicine.

REFERENCES

1. K. Krawczyk, S. Xue, P. Buchmann, G. Charpin-El-Hamri, P. Saxena, M. D. Hussherr, J. W. Shao, H. F. Ye, M. Q. Xie, M. Fussenegger, Electrogenetic cellular insulin release for real-time glycemic control in type 1 diabetic mice. *Science* **368**, 993-1001 (2020).

2. B. Park, J. H. Shin, J. Ok, S. Park, W. Jung, C. Jeong, S. Choy, Y. J. Jo, T. I. Kim, Cuticular pad-inspired selective frequency damper for nearly dynamic noise-free bioelectronics. *Science* **376**, 624-629 (2022).

3. X. G. Yu, Z. Q. Xie, Y. Yu, J. Lee, A. Vazquez-Guardado, H. W. Luan, J. Ruben, X. Ning, A. Akhtar, D. F. Li, B. W. Ji, Y. M. Liu, R. J. Sun, J. Y. Cao, Q. Z. Huo, Y. S. Zhong, C. Lee, S. Kim, P. Gutruf, C. X. Zhang, Y. G. Xue, Q. L. Guo, A. Chempakasseril, P. L. Tian, W. Lu, J. Jeong, Y. Yu, J. Cornman, C. Tan, B. Kirn, K. Lee, X. Feng, Y. G. Huang, J. A. Rogers, Skin-integrated wireless haptic interfaces for virtual and augmented reality. *Nature* **575**, 473–479 (2019).

4. Y. W. Jiang, Z. T. Zhang, Y. X. Wang, D. L. Li, C. T. Coen, E. Hwaun, G. Chen, H. C. Wu, D. L. Zhong, S. M. Niu, W. C. Wang, A. Saberi, J. C. Lai, Y. L. Wu, Y. Wang, A. A. Trotsyuk, K. Y. Loh, C. C. Shih, W. H. Xu, K. Liang, K. L. Zhang, Y. H. Bai, G. Gurusankar, W. P. Hu, W. Jia, Z. Cheng, R. H. Dauskardt, G. C. Gurtner, J. B. H. Tok, K. Deisseroth, I. Soltesz, Z. N. Bao, Topological supramolecular network enabled high-conductivity, stretchable organic bioelectronics. *Science* **375**, 1411-1417 (2022).

5. M. Q. Wang, Y. R. Yang, J. H. Min, Y. Song, J. B. Tu, D. Mukasa, C. Ye, C. H. Xu, N. Heflin, J. S. McCune, T. K. Hsiai, Z. P. Li, W. Gao, A wearable electrochemical biosensor for the monitoring of metabolites and nutrients. *Nature Biomedical Engineering* **6**, 1225-1235 (2022).

6. M. Bariya, L. Li, R. Ghattamaneni, C. H. Ahn, H. Y. Y. Nyein, L. C. Tai, A. Javey, Glove-based sensors for multimodal monitoring of natural sweat. *Science Advances* **6**, eabb8308 (2020).

7. Y. Song, J. H. Min, Y. Yu, H. B. Wang, Y. R. Yang, H. X. Zhang, W. Gao, Wireless battery-free wearable sweat sensor powered by human motion. *Science Advances* **6**, eaay9842 (2020).

8. Z. Jiang, N. Chen, Z. G. Yi, J. W. Zhong, F. L. Zhang, S. B. Ji, R. Liao, Y. Wang, H. C. Li, Z. H. Liu, Y. Wang, T. Yokota, X. G. Liu, K. Fukuda, X. D. Chen, T. Someya, A 1.3-micrometre-thick elastic conductor for seamless on-skin and implantable sensors. *Nature Electronics* **5**, 784-793 (2022).

9. Y. Luo, M. R. Abidian, J.-H. Ahn, D. Akinwande, A. M. Andrews, M. Antonietti, Z. Bao, M. Berggren, C. A. Berkey, C. J. Bettinger, J. Chen, P. Chen, W. Cheng, X. Cheng, S.-J. Choi, A. Chortos, C. Dagdeviren, R. H. Dauskardt, C.-a. Di, M. D. Dickey, X. Duan, A. Facchetti, Z. Fan, Y. Fang, J. Feng, X. Feng, H. Gao, W. Gao, X. Gong, C. F. Guo, X. Guo, M. C. Hartel, Z. He, J. S. Ho, Y. Hu, Q. Huang, Y. Huang, F. Huo, M. M. Hussain, A. Javey, U. Jeong, C. Jiang, X. Jiang, J. Kang, D. Karnaushenko, A. Khademhosseini, D.-H. Kim, I.-D. Kim, D. Kireev, L. Kong, C. Lee, N.-E. Lee, P. S. Lee, T.-W. Lee, F. Li, J. Li, C. Liang, C. T. Lim, Y. Lin, D. J. Lipomi, J. Liu, K. Liu, N. Liu, R. Liu, Y. Liu, Y. Liu, Z. Liu, Z. Liu, X. J. Loh, N. Lu, Z. Lv, S. Magdassi, G. G. Malliaras, N. Matsuhisa, A. Nathan, S. Niu, J. Pan, C. Pang, Q. Pei, H. Peng, D. Qi, H. Ren, J. A. Rogers, A. Rowe, O. G. Schmidt, T. Sekitani, D.-G. Seo, G. Shen, X. Sheng, Q. Shi, T. Someya, Y. Song, E. Stavrinidou, M. Su, X. Sun, K. Takei, X.-M. Tao, B. C. K. Tee, A. V.-Y. Thean, T. Q. Trung, C. Wan, H. Wang, J. Wang, M. Wang, S. Wang, T. Wang, Z. L. Wang, P. S. Weiss, H. Wen, S. Xu, T. Xu, H. Yan, X. Yan, H. Yang, L. Yang, S. Yang, L. Yin, C. Yu, G. Yu, J. Yu, S.-H. Yu, X. Yu, E. Zamburg, H. Zhang, X. Zhang, X. Zhang, X. Zhang, Y. Zhang, Y. Zhang, S. Zhao, X. Zhao, Y. Zheng, Y.-Q. Zheng, Z. Zheng, T. Zhou, B. Zhu, M.

Zhu, R. Zhu, Y. Zhu, Y. Zhu, G. Zou, X. Chen, Technology roadmap for flexible sensors. *ACS Nano* **17**, 5211-5295 (2023).

10. Y. Yu, J. Nassar, C. Xu, J. Min, Y. Yang, A. Dai, R. Doshi, A. Huang, Y. Song, R. Gehlhar, A. D. Ames, W. Gao, Biofuel-powered soft electronic skin with multiplexed and wireless sensing for human-machine interfaces. *Science Robotics* **5**, eaaz7946 (2020).

11. T. L. Liu, Y. Dong, S. L. Chen, J. Zhou, Z. Q. Ma, J. H. Li, Battery-free, tuning circuit-inspired wireless sensor systems for detection of multiple biomarkers in bodily fluids. *Science Advances* **8**, eabo7049 (2022).

12. H. U. Chung, B. H. Kim, J. Y. Lee, J. Lee, Z. Q. Xie, E. M. Ibler, K. Lee, A. Banks, J. Y. Jeong, J. Kim, C. Ogle, D. Grande, Y. Yu, H. Jang, P. Assem, D. Ryu, J. W. Kwak, M. Namkoong, J. B. Park, Y. Lee, D. H. Kim, A. Ryu, J. Jeong, K. You, B. W. Ji, Z. J. Liu, Q. Z. Huo, X. Feng, Y. J. Deng, Y. S. Xu, K. I. Jang, J. Kim, Y. H. Zhang, R. Ghaffari, C. M. Rand, M. Schau, A. Hamvas, D. E. Weese-Mayer, Y. G. Huang, S. M. Lee, C. H. Lee, N. R. Shanbhag, A. S. Paller, S. Xu, J. A. Rogers, Binodal, wireless epidermal electronic systems with in-sensor analytics for neonatal intensive care. *Science* **363**, eaau0780 (2019).

13. R. Ghaffari, D. Yang, J. Kim, A. Mansour, J. A. Wright, J. B. Model, D. E. Wright, J. A. Rogers, T. R. Ray, State of Sweat: Emerging Wearable Systems for Real-Time, Noninvasive Sweat Sensing and Analytics. *Acs Sensors* **6**, 2787-2801 (2021).

14. H. Y. Y. Nyein, M. Bariya, B. Tran, C. H. Ahn, B. J. Brown, W. B. Ji, N. Davis, A. Javey, A wearable patch for continuous analysis of thermoregulatory sweat at rest. *Nature Communications* **12**, 1823 (2021).

15. U. Mogera, H. Guo, M. Namkoong, M. S. Rahman, T. Nguyen, L. M. Tian, Wearable plasmonic paper-based microfluidics for continuous sweat analysis. *Science Advances* **8**, eabn1736 (2022).

16. L. B. Baker, J. B. Model, K. A. Barnes, M. L. Anderson, S. P. Lee, K. A. Lee, S. D. Brown, A. J. Reimel, T. J. Roberts, R. P. Nuccio, J. L. Bonsignore, C. T. Ungaro, J. M. Carter, W. H. Li, M. S. Seib, J. T. Reeder, A. J. Aranyosi, J. A. Rogers, R. Ghaffari, Skin-interfaced microfluidic system with personalized sweating rate and sweat chloride analytics for sports science applications. *Science Advances* **6**, eabe3929 (2020).

17. X. Ma, Z. Jiang, Y. Lin, Flexible energy storage devices for wearable bioelectronics. *Journal of Semiconductors* **42**, 101602 (2021).

18. X. Ma, R. Peng, W. Mao, Y. Lin, H. Yu, Recent advances in ion-sensitive field-effect transistors for biosensing applications. *Electrochem. Sci. Adv* **1**, e2100163 (2021).

19. R. G. Frykberg, J. Banks, Challenges in the Treatment of Chronic Wounds. *Advances in Wound Care* **4**, 560-582 (2015).

20. Y. J. Gao, D. T. Nguyen, T. Yeo, S. B. Lim, W. X. Tan, L. E. Madden, L. Jin, J. Long, F. A. Aloweni, Y. J. A. Liew, M. L. Tan, S. Y. Ang, S. D. O. Maniya, I. Abdelwahab, K. P. Loh, C. H. Chen, D. L. Becker, D. Leavesley, J. S. Ho, C. T. Lim, A flexible multiplexed immunosensor for point-of-care in situ wound monitoring. *Science Advances* **7**, 15 (2021).

21. Y. W. Jiang, A. A. Trotsyuk, S. M. Niu, D. Henn, K. Chen, C. C. Shih, M. R. Larson, A. M. Mermin-Bunnell, S. Mittal, J. C. Lai, A. Saberi, E. Beard, S. Jing, D. L. Zhong, S. R. Steele, K. F. Sun, T. Jain, E. Zhao, C. R. Neimeth, W. G. Viana, J. Tang, D. Sivaraj, J. Padmanabhan, M. Rodrigues, D. P. Perrault, A. Chattopadhyay, Z. N. Maan, M. C. Leeolou, C. A. Bonham, S. H. Kwon, H. C. Kussie, K. S. Fischer, G. Gurusankar, K. Liang, K. L. Zhang, R. Nag, M. P. Snyder,

M. Januszyk, G. C. Gurtner, Z. N. Bao, Wireless, closed-loop, smart bandage with integrated sensors and stimulators for advanced wound care and accelerated healing. *Nature Biotechnology* **41**, 652 (2023).

22. E. S. Sani, C. H. Xu, C. R. Wang, Y. Song, J. H. Min, J. B. Tu, S. A. Solomon, J. H. Li, J. L. Banks, D. G. Armstrong, W. Gao, A stretchable wireless wearable bioelectronic system for multiplexed monitoring and combination treatment of infected chronic wounds. *Science Advances* **9**, (2023).

23. J. Y. Shi, S. Kim, P. J. Li, F. Y. Dong, C. W. Yang, B. Nam, C. Han, E. Eig, L. L. Shi, S. M. Niu, J. P. Yue, B. Z. Tian, Active biointegrated living electronics for managing inflammation. *Science* **384**, 1023-1030 (2024).

24. J. W. Song, H. Ryu, W. B. Bai, Z. Q. Xie, A. Vazquez-Guardado, K. Nandoliya, R. Avila, G. Lee, Z. Song, J. Kim, M. K. Lee, Y. G. Liu, M. Kim, H. F. Wang, Y. X. Wu, H. J. Yoon, S. S. Kwak, J. Shin, K. Kwon, W. Lu, X. X. Chen, Y. G. Huang, G. A. Ameer, J. A. Rogers, Bioresorbable, wireless, and battery-free system for electrotherapy and impedance sensing at wound sites. *Science Advances* **9**, (2023).

25. Z. Xiong, S. Achavananthadith, S. Lian, L. E. Madden, Z. X. Ong, W. Chua, V. Kalidasan, Z. P. Li, Z. Liu, P. Singh, H. T. Yang, S. P. Heussler, S. M. P. Kalaiselvi, M. B. H. Breese, H. C. Yao, Y. J. Gao, K. Sanmugam, B. C. K. Tee, P. Y. Chen, W. Q. Loke, C. T. Lim, G. S. H. Chiang, B. Y. Tan, H. Li, D. L. Becker, J. S. Ho, A wireless and battery-free wound infection sensor based on DNA hydrogel. *Science Advances* **7**, (2021).

26. X. T. Zheng, Z. J. Yang, L. Sutarlie, M. Thangaveloo, Y. Yu, N. Salleh, J. S. Chin, Z. Xiong, D. L. Becker, X. J. Loh, B. C. K. Tee, X. D. Su, Battery-free and AI-enabled multiplexed sensor patches for wound monitoring. *Science Advances* **9**, (2023).

27. Y. Huang, M. Chen, F. J. Jiang, C. Z. Lu, Q. S. Zhu, Y. Yang, L. Fu, L. M. Li, J. Liu, Z. G. Wang, X. W. Cao, W. Wei, Microfluidic-SERS sensing system based on dual signal amplification and aptamer for gastric cancer detection. *Microchimica Acta* **191**, (2024).

28. F. Khosravi, S. M. Loeian, B. Panchapakesan, Ultrasensitive Label-Free Sensing of IL-6 Based on PASE Functionalized Carbon Nanotube Micro-Arrays with RNA-Aptamers as Molecular Recognition Elements. *Biosensors-Basel* **7**, (2017).

29. L. S. S. Kumar, X. Wang, J. Hagen, R. Naik, I. Papautsky, J. Heikenfeld, Label free nano-aptasensor for interleukin-6 in protein-dilute bio fluids such as sweat. *Analytical Methods* **8**, 3440-3444 (2016).

30. K. E. Laliberte, P. Scott, N. I. Khan, M. S. Mahmud, E. D. Song, A wearable graphene transistor-based biosensor for monitoring IL-6 biomarker. *Microelectronic Engineering* **262**, (2022).

31. Y. A. Li, X. Hua, J. J. Wang, B. K. Jin, cMWCNT/CoHCF/AuNPs nanocomposites aptasensor for electrochemical detection of interleukin-6. *Talanta Open* **7**, (2023).

32. Z. Liu, F. Y. Liu, C. F. Wang, H. J. Li, Y. Q. Xu, S. G. Sun, Ratiometric Electrochemical Detection of Interleukin-6 Using Electropolymerized Methylene Blue and a Multi-Walled Carbon-Nanotube-Modified Screen-Printed Carbon Electrode. *Biosensors-Basel* **14**, (2024).

33. M. Muhammad, C. S. Shao, Q. Huang, Aptamer-functionalized Au nanoparticles array as the effective SERS biosensor for label-free detection of interleukin-6 in serum. *Sensors and Actuators B-Chemical* **334**, (2021).

34. N. A. P. Ondevilla, P. W. Liu, W. T. Huang, T. P. Weng, N. Y. Lee, S. C. Ma, J. J. Huang, T. W. Wong, H. C. Chang, A point-of-care electrochemical biosensor for the rapid and sensitive detection of biomarkers in murine models with LPS-induced sepsis. *Biosensors & Bioelectronics* **254**, (2024).

35. M. Tertis, B. Ciui, M. Suciu, R. Sandulescu, C. Cristea, Label-free electrochemical aptasensor based on gold and polypyrrole nanoparticles for interleukin 6 detection. *Electrochimica Acta* **258**, 1208-1218 (2017).

36. H. Derakhshandeh, S. S. Kashaf, F. Aghabaglou, I. O. Ghanavati, A. Tamayol, Smart Bandages: The Future of Wound Care. *Trends in Biotechnology* **36**, 1259-1274 (2018).

37. Y. Q. Wang, M. Z. Guo, B. F. He, B. B. Gao, Intelligent Patches for Wound Management: In Situ Sensing and Treatment. *Analytical Chemistry* **93**, 4687-4696 (2021).

38. B. K. Ashley, M. S. Brown, Y. Park, S. Kuan, A. Koh, Skin-inspired, open mesh electrochemical sensors for lactate and oxygen monitoring. *Biosensors & Bioelectronics* **132**, 343-351 (2019).

39. W. Duan, J. Zhao, Y. Gao, K. Xu, S. Huang, L. Zeng, J.-W. Shen, Y. Zheng, J. Wu, Porous silicon-based sensing and delivery platforms for wound management applications. *Journal of Controlled Release* **371**, 530-554 (2024).

40. S. W. Huang, Y. F. Wu, T. Ahmed, S. C. Pan, C. M. Cheng, Point-of-care detection devices for wound care and monitoring. *Trends in Biotechnology* **42**, 74-90 (2024).

41. A. Levin, S. Gong, W. L. Cheng, Wearable smart bandage-based bio-sensors. *Biosensors-Basel* **13**, (2023).

42. J. Li, Z. P. Li, J. Xiao, C. Y. Nie, Conformable electrochemical devices for closed-loop wound management. *Frontiers In Bioengineering And Biotechnology* **11**, (2023).

43. J. H. Pu, K. T. Ma, Y. H. Luo, S. Y. Tang, T. Y. Liu, J. Liu, M. Leung, J. Yang, R. M. Hui, Y. Xiong, X. M. Tao, Textile electronics for wearable applications. *International Journal Of Extreme Manufacturing* **5**, (2023).

44. A. Pusta, M. Tertis, C. Cristea, S. Mirel, Wearable sensors for the detection of biomarkers for wound infection. *Biosensors-Basel* **12**, (2022).

45. S. L. A. Jeffery, The Management of Combat Wounds: The British Military Experience. *Advances in Wound Care* **5**, 464-473 (2016).

46. M. D. Mayer, R. Y. Lai, Effects of redox label location on the performance of an electrochemical aptamer-based tumor necrosis factor-alpha sensor. *Talanta* **189**, 585-591 (2018).

47. K. Saito, D. Kobayashi, M. Komatsu, T. Yajima, A. Yagihashi, Y. Ishikawa, R. Minami, N. Watanabe, A sensitive assay of tumor necrosis factor α in sera from Duchenne muscular dystrophy patients. *Clinical Chemistry* **46**, 1703-1704 (2000).

48. E. Sánchez-Tirado, C. Salvo, A. González-Cortés, P. Yáñez-Sedeño, F. Langa, J. M. Pingarrón, Electrochemical immunosensor for simultaneous determination of interleukin-1 beta and tumor necrosis factor alpha in serum and saliva using dual screen printed electrodes modified with functionalized double walled carbon nanotubes. *Analytica Chimica Acta* **959**, 66-73 (2017).

49. E. S. Sani, C. R. Wang, W. Gao, A soft bioaffinity sensor array for chronic wound monitoring. *Matter* **4**, 2613-2615 (2021).

50. R. Say, E. B. Özkütük, O. B. Ünlüer, D. Ugurag, A. Ersöz, Nano anti-tumor necrosis factor-alpha based potentiometric sensor for tumor necrosis factor-alpha detection. *Sensors And Actuators B-Chemical* **209**, 864-869 (2015).

51. S. P. Song, L. H. Wang, J. Li, J. L. Zhao, C. H. Fan, Aptamer-based biosensors. *Trac-Trends In Analytical Chemistry* **27**, 108-117 (2008).

52. A. K. Yagati, G. Y. Lee, S. Ha, K. A. Chang, J. C. Pyun, S. Cho, Impedimetric Tumor Necrosis Factor-α Sensor Based on a Reduced Graphene Oxide Nanoparticle-Modified Electrode Array. *Journal Of Nanoscience And Nanotechnology* **16**, 11921-11927 (2016).

53. A. K. Yagati, M. H. Lee, J. Min, Electrochemical immunosensor for highly sensitive and quantitative detection of tumor necrosis factor-α in human serum. *Bioelectrochemistry* **122**, 93-102 (2018).

54. S. Y. Low, J. E. Hill, J. Peccia, DNA aptamers bind specifically and selectively to (1 → 3)-β-D-glucans. *Biochemical And Biophysical Research Communications* **378**, 701-705 (2009).

55. X. Ma, X. Li, W. Zhang, F. Meng, X. Wang, Y. Qin, M. Zhang, Carbon-basednanocomposite smart sensors for the rapid detection of mycotoxins. *Nanomaterials* **11**, (2021).

56. P. D. P. Swetha, A. Nikitha, M. M. Shenoy, Y. B. Shim, K. S. Prasad, Ni/Ni(OH)2-rGO nanocomposites sensor for the detection of long forgotten mycotoxin, xanthomegnin. *Talanta* **253**, (2023).

57. X. L. Tang, Y. Hua, Q. Guan, C. H. Yuan, Improved detection of deeply invasive candidiasis with DNA aptamers specific binding to (1→3)-β-D-glucans from Candida albicans. *European Journal Of Clinical Microbiology & Infectious Diseases* **35**, 587-595 (2016).

58. N. T. Thet, J. Mercer-Chalmers, R. J. Greenwood, A. E. R. Young, K. Coy, S. Booth, A. Sack, A. T. A. Jenkins, SPaCE Swab: Point-of-Care Sensor for Simple and Rapid Detection of Acute Wound Infection. *Acs Sensors* **5**, 2652-2657 (2020).

59. P. F. Zuo, F. Gong, Y. X. Yang, X. H. Ji, Z. K. He, In situ fluorescence imaging of fungi via (1,3)-β-D-glucan aptamer and tyramide signal amplification technology. *Chinese Chemical Letters* **34**, (2023).

60. Y. ElSaboni, J. A. Hunt, J. Stanley, C. Moffatt, Y. Wei, Development of a textile based protein sensor for monitoring the healing progress of a wound. *Scientific Reports* **12**, (2022).

61. S. Hasanpour, L. Karperien, T. Walsh, M. Jahanshahi, Z. Hadisi, K. J. Neale, B. R. Christie, N. Djilali, M. Akbari, A hybrid thread-based temperature and humidity sensor for continuous wound monitoring. *Sensors And Actuators B-Chemical* **370**, (2022).

62. A. N. Pereira, T. Noushin, S. Tabassum, Ieee, paper presented at the 2021 Ieee Sensors, 2021.

63. M. Tessarolo, L. Possanzini, I. Gualandi, F. Mariani, L. D. Torchia, D. Arcangeli, F. Melandri, E. Scavetta, B. Fraboni, Wireless textile moisture sensor for wound care. *Frontiers In Physics* **9**, (2021).

64. X. Q. Chen, H. Wan, R. Guo, X. P. Wang, Y. Wang, C. C. Jiao, K. Sun, L. Hu, A double-layered liquid metal-based electrochemical sensing system on fabric as a wearable detector for glucose in sweat. *Microsystems & Nanoengineering* **8**, 48 (2022).

65. B. H. Wang, A. Facchetti, Mechanically flexible conductors for stretchable and wearable E-skin and E-textile devices. *Adv. Mater.* **31**, 1901408 (2019).

66. J. D. Shi, S. Liu, L. S. Zhang, B. Yang, L. Shu, Y. Yang, M. Ren, Y. Wang, J. W. Chen, W. Chen, Y. Choi, X. M. Tao, Smart textile-integrated microelectronic systems for wearable applications. *Adv. Mater.* **32**, 1901958 (2020).

67. R. Z. Lin, H. J. Kim, S. Achavananthadith, Z. Xiong, J. K. W. Lee, Y. L. Kong, J. S. Ho, Digitally-embroidered liquid metal electronic textiles for wearable wireless systems. *Nature Communications* **13**, 2190 (2022).

68. S. Qureshi, G. M. Stojanovic, M. Simic, V. Jeoti, N. Lashari, F. Sher, Silver conductive threads-based embroidered electrodes on textiles as moisture sensors for fluid detection in biomedical applications. *Materials* **14**, 7813 (2021).

69. Q. Y. Huang, D. R. Wang, H. Hu, J. Shang, J. Chang, C. Xie, Y. Yang, X. Lepro, R. H. Baughman, Z. J. Zheng, Additive functionalization and embroidery for manufacturing wearable and washable textile supercapacitors. *Adv. Funct. Mater.* **30**, 1910541 (2020).

70. E. Ismar, X. Y. Tao, F. Rault, F. Dassonville, C. Cochrane, Towards embroidered circuit board from conductive yarns for E-textiles. *Ieee Access* **8**, 155329-155336 (2020).

71. M. Parrilla, M. Cuartero, G. A. Crespo, Wearable potentiometric ion sensors. *Trac-Trends in Analytical Chemistry* **110**, 303-320 (2019).

72. T. Tat, G. R. Chen, X. Zhao, Y. H. Zhou, J. Xu, J. Chen, Smart Textiles for Healthcare and Sustainability. *Acs Nano* **16**, 13301-13313 (2022).

73. H. C. Ates, P. Q. Nguyen, L. Gonzalez-Macia, E. Morales-Narvaz, F. Guder, J. J. Collins, C. Dincer, End-to-end design of wearable sensors. *Nature Reviews Materials* **7**, 887-907 (2022).

74. P. F. Yang, G. F. Wei, A. Liu, F. W. Huo, Z. N. Zhang, A review of sampling, energy supply and intelligent monitoring for long-term sweat sensors. *Npj Flexible Electronics* **6**, (2022).

75. W. Gao, S. Emaminejad, H. Y. Y. Nyein, S. Challa, K. V. Chen, A. Peck, H. M. Fahad, H. Ota, H. Shiraki, D. Kiriya, D. H. Lien, G. A. Brooks, R. W. Davis, A. Javey, Fully integrated wearable sensor arrays for multiplexed in situ perspiration analysis. *Nature* **529**, 509-+ (2016).

76. L. Yin, M. Z. Cao, K. N. Kim, M. Y. Lin, J. M. Moon, J. R. Sempionatto, J. L. Yu, R. X. Liu, C. Wicker, A. Trifonov, F. Y. Zhang, H. J. Hu, J. R. Moreto, J. Go, S. Xu, J. S. Wang, A stretchable epidermal sweat sensing platform with an integrated printed battery and electrochromic display. *Nature Electronics* **5**, 694-705 (2022).

77. A. Libanori, G. R. Chen, X. Zhao, Y. H. Zhou, J. Chen, Smart textiles for personalized healthcare. *Nature Electronics* **5**, 142-156 (2022).

78. J. Xu, Y. S. Fang, J. Chen, Wearable Biosensors for Non-Invasive Sweat Diagnostics. *Biosensors-Basel* **11**, (2021).

79. B. W. Zhong, K. Jiang, L. L. Wang, G. Z. Shen, Wearable Sweat Loss Measuring Devices: From the Role of Sweat Loss to Advanced Mechanisms and Designs. *Advanced Science* **9**, (2022).

80. P. Pirovano, M. Dorrian, A. Shinde, A. Donohoe, A. J. Brady, N. M. Moyna, G. Wallace, D. Diamond, M. McCaul, A wearable sensor for the detection of sodium and potassium in human sweat during exercise. *Talanta* **219**, (2020).

81. A. K. Oktavius, Q. Gu, N. Wihardjo, O. Winata, S. W. Sunanto, J. Li, P. Gao, Fully-Conformable Porous Polyethylene Nanofilm Sweat Sensor for Sports Fatigue. *Ieee Sensors Journal* **21**, 8861-8867 (2021).

82. G. Bergamini, G. Tridello, E. Calcaterra, S. Ceri, M. Tagliasacchi, F. Bianchi, F. Monti, A. Masciadri, E. Laudanna, D. Peserico, E. Sorio, V. Esposito, T. Leal, B. M. Assael, C. Sorio, P. Melotti, Ratiometric sweat secretion optical test in cystic fibrosis, carriers and healthy subjects. *Journal of Cystic Fibrosis* **17**, 186-189 (2018).

83. W. Gao, G. A. Brooks, D. C. Klonoff, Wearable physiological systems and technologies for metabolic monitoring. *Journal of Applied Physiology* **124**, 548-556 (2018).

84. M. Bariya, L. Li, R. Ghattamaneni, C. H. Ahn, H. Y. Y. Nyein, L. C. Tai, A. Javey, Glove-based sensors for multimodal monitoring of natural sweat. *Science Advances* **6**, (2020).

85. S. B. Kim, Y. Zhang, S. M. Won, A. J. Bandodkar, Y. Sekine, Y. G. Xue, J. Koo, S. W. Harshman, J. A. Martin, J. M. Park, T. R. Ray, K. E. Crawford, K. T. Lee, J. Choi, R. L. Pitsch, C. C. Grigsby, A. J. Strang, Y. Y. Chen, S. Xu, J. Kim, A. Koh, J. S. Ha, Y. G. Huang, S. W. Kim, J. A. Rogers, Super-Absorbent Polymer Valves and Colorimetric Chemistries for Time-Sequenced Discrete Sampling and Chloride Analysis of Sweat via Skin-Mounted Soft Microfluidics. *Small* **14**, (2018).

86. Y. M. Liu, X. C. Huang, J. K. Zhou, C. K. Yiu, Z. Song, W. Huang, S. K. Nejad, H. Li, T. H. Wong, K. M. Yao, L. Zhao, W. Yoo, W. Park, J. Y. Li, Y. Huang, H. R. Lam, E. M. Song, X. Guo, Y. W. Wang, Z. X. Dai, L. Q. Chang, W. J. Li, Z. Q. Xie, X. G. Yu, Stretchable Sweat-Activated Battery in Skin-Integrated Electronics for Continuous Wireless Sweat Monitoring. *Advanced Science* **9**, (2022).

87. C. H. Liu, T. L. Xu, D. D. Wang, X. J. Zhang, The role of sampling in wearable sweat sensors. *Talanta* **212**, (2020).

88. D. Vairo, L. Bruzzese, M. Marlinge, L. Fuster, N. Adjriou, N. Kipson, P. Brunet, J. Cautela, Y. Jammes, G. Mottola, S. Burtey, J. Ruf, R. Guieu, E. Fenouillet, Towards Addressing the Body Electrolyte Environment via Sweat Analysis:Pilocarpine Iontophoresis Supports Assessment of Plasma Potassium Concentration. *Scientific Reports* **7**, (2017).

89. M. R. Prausnitz, The effects of electric current applied to skin: A review for transdermal drug delivery. *Advanced Drug Delivery Reviews* **18**, 395-425 (1996).

90. M. C. Desax, R. A. Ammann, J. Hammer, M. H. Schoeni, J. Barben, G. Swiss Paediat Resp Res, Nanoduct (R) sweat testing for rapid diagnosis in newborns, infants and children with cystic fibrosis. *European Journal of Pediatrics* **167**, 299-304 (2008).

91. L. B. Baker, J. R. Stofan, A. A. Hamilton, C. A. Horswill, Comparison of regional patch collection vs. whole body washdown for measuring sweat sodium and potassium loss during exercise. *Journal of Applied Physiology* **107**, 887-895 (2009).

92. G. Matzeu, C. Fay, A. Vaillant, S. Coyle, D. Diamond, A Wearable Device for Monitoring Sweat Rates via Image Analysis. *Ieee Transactions on Biomedical Engineering* **63**, 1672-1680 (2016).

93. Y. R. Yang, W. Gao, Wearable and flexible electronics for continuous molecular monitoring. *Chemical Society Reviews* **48**, 1465-1491 (2019).

94. J. D. Shi, S. Liu, L. S. Zhang, B. Yang, L. Shu, Y. Yang, M. Ren, Y. Wang, J. W. Chen, W. Chen, Y. Choi, X. M. Tao, Smart Textile-Integrated Microelectronic Systems for Wearable Applications. *Advanced Materials* **32**, (2020).

95. M. C. Brothers, M. DeBrosse, C. C. Grigsby, R. R. Naik, S. M. Hussain, J. Heikenfeld, S. S. Kim, Achievements and Challenges for Real-Time Sensing of Analytes in Sweat within Wearable Platforms. *Accounts of Chemical Research* **52**, 297-306 (2019).

96. K. Jarbrink, G. Ni, H. Sonnergren, A. Schmidtchen, C. Pang, R. Bajpai, J. Car, The humanistic and economic burden of chronic wounds: a protocol for a systematic review. *Systematic Reviews* **6**, (2017).

97. C. K. Sen, Human wounds and its burden: an updated compendium of estimates. *Advances in Wound Care* **8**, 39-48 (2019).

98. X. Y. Sun, Y. C. Zhang, C. Y. Ma, Q. C. Yuan, X. Y. Wang, H. Wan, P. Wang, A Review of Recent Advances in Flexible Wearable Sensors for Wound Detection Based on Optical and Electrical Sensing. *Biosensors-Basel* **12**, (2022).

99. C. R. Wang, E. S. Sani, W. Gao, Wearable bioelectronics for chronic woundmanagement. *Advanced Functional Materials* **32**, (2022).

100. X. F. Wang, B. W. Zhong, Z. Lou, W. Han, L. L. Wang, The advancement of intelligent dressings for monitoring chronic wound infections. *Chemical Engineering Journal* **484**, (2024).

101. C. D. Yang, C. Yang, Y. Y. Chen, J. Y. Liu, Z. Q. Liu, H. J. Chen, The trends in wound management: Sensing, therapeutic treatment, and "theranostics". *Journal of Science-Advanced Materials and Devices* **8**, (2023).

102. K. Youssef, A. Ullah, P. Rezai, A. Hasan, A. Amirfazli, Recent advances in biosensors for real time monitoring of pH, temperature, and oxygen in chronic wounds. *Materials Today Bio* **22**, (2023).

103. Q. Zeng, G. Shi, M. Zhang, Real-time monitoring of wound states via rationally engineered biosensors. *Advanced Sensor Research* **3**, 2200018 (2024).

104. J. Zhu, H. L. Zhou, E. M. Gerhard, S. H. Zhang, F. I. P. Rodríguez, T. S. Pan, H. B. Yang, Y. Lin, J. Yang, H. Y. Cheng, Smart bioadhesives for wound healing and closure. *Bioactive Materials* **19**, 360-375 (2023).

105. P. Salvo, V. Dini, A. Kirchhain, A. Janowska, T. Oranges, A. Chiricozzi, T. Lomonaco, F. Di Francesco, M. Romanelli, Sensors and Biosensors for C-Reactive Protein, Temperature and pH, and Their Applications for Monitoring Wound Healing: A Review. *Sensors* **17**, (2017).

106. Z. Q. Liu, J. Q. Liu, T. C. Sun, D. K. Zeng, C. D. Yang, H. Wang, C. Yang, J. Guo, Q. N. Wu, H. J. Chen, X. Xie, Integrated Multiplex Sensing Bandage for In Situ Monitoring of Early Infected Wounds. *Acs Sensors* **6**, 3112-3124 (2021).

107. Y. J. Gao, D. T. Nguyen, T. Yeo, S. B. Lim, W. X. Tan, L. E. Madden, L. Jin, J. Long, F. A. Aloweni, Y. J. A. Liew, M. L. Tan, S. Y. Ang, S. D. O. Maniya, I. Abdelwahab, K. P. Loh, C. H. Chen, D. L. Becker, D. Leavesley, J. S. Ho, C. T. Lim, A flexible multiplexed immunosensor for point-of-care in situ wound monitoring. *Science Advances* **7**, (2021).

108. G. Xu, Y. L. Lu, C. Cheng, X. Li, J. Xu, Z. Y. Liu, J. L. Liu, G. Liu, Z. H. Shi, Z. T. Chen, F. N. Zhang, Y. X. Jia, D. F. Xu, W. Yuan, Z. Cui, S. S. Low, Q. J. Liu, Battery-Free and Wireless Smart Wound Dressing for Wound Infection Monitoring and Electrically Controlled On-Demand Drug Delivery. *Advanced Functional Materials* **31**, (2021).

109. K. K. Yeung, T. Huang, Y. Z. Hua, K. Zhang, M. M. F. Yuen, Z. L. Gao, Recent Advances in Electrochemical Sensors for Wearable Sweat Monitoring: A Review. *Ieee Sensors Journal* **21**, 14522-14539 (2021).

110. T. Guinovart, M. Parrilla, G. A. Crespo, F. X. Rius, F. J. Andrade, Potentiometric sensors using cotton yarns, carbon nanotubes and polymeric membranes. *Analyst* **138**, 5208-5215 (2013).

111. M. Parrilla, J. Ferre, T. Guinovart, F. J. Andrade, Wearable potentiometric sensors based on commercial carbon fibres for monitoring sodium in sweat. *Electroanalysis* **28**, 1267-1275 (2016).

112. R. Wang, Q. F. Zhai, T. C. An, S. Gong, W. L. Cheng, Stretchable gold fiber-based wearable textile electrochemical biosensor for lactate monitoring in sweat. *Talanta* **222**, 121484 (2021).

113. W. Y. He, C. Y. Wang, H. M. Wang, M. Q. Jian, W. D. Lu, X. P. Liang, X. Zhang, F. C. Yang, Y. Y. Zhang, Integrated textile sensor patch for real-time and multiplex sweat analysis. *Science Advances* **5**, eaax0649 (2019).

114. M. Parrilla, R. Canovas, I. Jeerapan, F. J. Andrade, J. Wang, A textile-based stretchable multi-ion potentiometric sensor. *Advanced Healthcare Materials* **5**, 996-1001 (2016).

115. L. Possanzini, F. Decataldo, F. Mariani, I. Gualandi, M. Tessarolo, E. Scavetta, B. Fraboni, Textile sensors platform for the selective and simultaneous detection of chloride ion and pH in sweat. *Scientific Reports* **10**, (2020).

116. T. Terse-Thakoor, M. Punjiya, Z. Matharu, B. Y. Lyu, M. Ahmad, G. E. Giles, R. Owyeung, F. Alaimo, M. S. Baghini, T. T. Brunye, S. Sonkusale, Thread-based multiplexed sensor patch for real-time sweat monitoring. *Npj Flexible Electronics* **4**, 18 (2020).

117. H. Filik, A. A. Avan, Electrochemical immunosensors for the detection of cytokine tumor necrosis factor alpha: A review. *Talanta* **211**, (2020).

118. U. Eletxigerra, J. Martinez-Perdiguero, S. Merino, R. Villalonga, J. M. Pingarron, S. Campuzano, Amperometric magnetoimmunoassay for the direct detection of tumor necrosis factor alpha biomarker in human serum. *Analytica Chimica Acta* **838**, 37-44 (2014).

119. M. Bahri, A. Baraket, N. Zine, M. Ben Ali, J. Bausells, A. Errachid, Capacitance electrochemical biosensor based on silicon nitride transducer for TNF-α cytokine detection in artificial human saliva: Heart failure (HF). *Talanta* **209**, (2020).

120. L. Barhoumi, A. Baraket, F. G. Bellagambi, G. S. Karanasiou, M. Ben Ali, D. I. Fotiadis, J. Bausells, N. Zine, M. Sigaud, A. Errachid, A novel chronoamperometric immunosensor for rapid detection of TNF-α in human saliva. *Sensors And Actuators B-Chemical* **266**, 477-484 (2018).

121. L. Barhoumi, F. G. Bellagambi, F. M. Vivaldi, A. Baraket, Y. Clément, N. Zine, M. Ben Ali, A. Elaissari, A. Errachid, Ultrasensitive Immunosensor Array for TNF-α Detection in Artificial Saliva using Polymer-Coated Magnetic Microparticles onto Screen-Printed Gold Electrode. *Sensors* **19**, (2019).

122. C. Diacci, B. Burtscher, M. Berto, T. P. Ruoko, S. Lienemann, P. Greco, M. Berggren, M. Borsari, D. T. Simon, C. A. Bortolotti, F. Biscarini, Organic Electrochemical Transistor Aptasensor for Interleukin-6 Detection. *Acs Applied Materials & Interfaces* **16**, 61467-61474 (2023).

123. U. Eletxigerra, J. Martinez-Perdiguero, S. Merino, R. Villalonga, J. M. Pingarrón, S. Campuzano, Amperometric magnetoimmunoassay for the direct detection of tumor necrosis factor alpha biomarker in human serum. *Analytica Chimica Acta* **838**, 37-44 (2014).

124. C. Jiang, M. T. Alam, S. M. Silva, S. Taufik, S. J. Fan, J. J. Gooding, Unique Sensing Interface That Allows the Development of an Electrochemical Immunosensor for the Detection of Tumor Necrosis Factor α in Whole Blood. *acs sensors* **1**, 1432-1438 (2016).

125. R. Y. Lai, B. Walker, K. Stormberg, A. J. Zaitouna, W. W. Yang, Electrochemical techniques for characterization of stem-loop probe and linear probe-based DNA sensors. *Methods* **64**, 267-275 (2013).

126. Y. Liu, Q. Zhou, A. Revzin, An aptasensor for electrochemical detection of tumor necrosis factor in human blood. *Analyst* **138**, 4321-4326 (2013).

127. C. M. Cao, F. Y. Zhang, E. M. Goldys, F. Gao, G. Z. Liu, Advances in structure-switching aptasensing towards real time detection of cytokines. *Trac-Trends in Analytical Chemistry* **102**, 379-396 (2018).

128. C. H. Fan, K. W. Plaxco, A. J. Heeger, Electrochemical interrogation of conformational changes as a reagentless method for the sequence-specific detection of DNA. *Proceedings Of The National Academy Of Sciences Of The United States Of America* **100**, 9134-9137 (2003).

129. D. Kadadou, L. Tizani, V. S. Wadi, F. Banat, H. Alsafar, A. F. Yousef, S. W. Hasan, Detection of SARS-CoV-2 in clinical and environmental samples using highly sensitive reduced graphene oxide (rGO)-based biosensor. *Chemical Engineering Journal* **453**, (2023).

130. M. W. Löffler, H. Schuster, S. Bühler, S. Beckert, Wound Fluid in Diabetic Foot Ulceration: More Than Just an Undefined Soup? *International Journal Of Lower Extremity Wounds* **12**, 113-129 (2013).

131. Y. Xiao, A. A. Lubin, A. J. Heeger, K. W. Plaxco, Label-free electronic detection of thrombin in blood serum by using an aptamer-based sensor. *Angewandte Chemie-International Edition* **44**, 5456-5459 (2005).

132. M. X. Yu, X. Y. Shang, M. Wang, Y. L. Liu, T. T. Ye, Exploiting Embroidered UHF RFID Antennas as Deformation Sensors. *Ieee Journal of Radio Frequency Identification* **4**, 406-413 (2020).

133. H. J. Kim, Y. X. Jin, S. Achavananthadith, R. Z. Lin, J. S. Ho, A wireless optoelectronic skin patch for light delivery and thermal monitoring. *Iscience* **24**, (2021).

134. S. M. Ali, C. Sovuthy, S. Noghanian, T. Saeidi, M. F. Majeed, A. Hussain, F. Masood, S. M. Khan, S. A. Shah, Q. H. Abbasi, Design and evaluation of a button sensor antenna for on-body monitoring activity in healthcare applications. *Micromachines* **13**, 475 (2022).

135. K. Kwon, H. L. Wang, J. Lim, K. S. Chun, H. Jang, I. Yoo, D. Wu, A. J. Chen, C. G. Gu, L. Lipschultz, J. U. Kim, J. Kim, H. Jeong, H. W. Luan, Y. Park, C. J. Su, Y. Ishida, S. R. Madhvapathy, A. Ikoma, J. W. Kwak, D. S. Yang, A. Banks, S. Xu, Y. G. Huang, J. K. Chang, J. A. Rogers, Wireless, soft electronics for rapid, multisensor measurements of hydration levels in healthy and diseased skin. *Proceedings of the National Academy of Sciences of the United States of America* **118**, e2020398118 (2021).

136. N. A. Choudhry, L. Arnold, A. Rasheed, I. A. Khan, L. J. Wang, Textronics-A Review of Textile-Based Wearable Electronics. *Advanced Engineering Materials* **23**, (2021).

137. Z. H. Shi, C. B. Dai, P. X. Deng, X. Li, Y. Wu, J. J. Lv, C. H. Xiong, Y. F. Shuai, F. N. Zhang, D. Wang, H. Liang, Y. He, Q. M. Chen, Y. L. Lu, Q. J. Liu, Wearable battery-free smart bandage with peptide functionalized biosensors based on MXene for bacterial wound infection detection. *Sensors and Actuators B-Chemical* **383**, 10 (2023).

138. R. Z. Lin, H. J. Kim, S. Achavananthadith, S. A. Kurt, S. C. C. Tan, H. C. Yao, B. C. K. Tee, J. K. W. Lee, J. S. Ho, Wireless battery-free body sensor networks using near-field-enabled clothing. *Nature Communications* **11**, (2020).

139. S. Hwang, M. Kang, A. Lee, S. Bae, S. K. Lee, S. H. Lee, T. Lee, G. Wang, T. W. Kim, Integration of multiple electronic components on a microfibre towards an emerging electronic textile platform. *Nature Communications* **13**, (2022).

140. X. C. Huang, Y. M. Liu, J. K. Zhou, S. K. Nejad, T. H. Wong, Y. Huang, H. Li, C. K. Yiu, W. Park, J. Li, J. Y. Su, L. Zhao, K. M. Yao, M. G. Wu, Z. Gao, D. F. Li, J. Y. Li, R. Shi, X. G. Yu, Garment embedded sweat-activated batteries in wearable electronics for continuous sweat monitoring. *Npj Flexible Electronics* **6**, (2022).

141. X. Q. Chen, H. Wan, R. Guo, X. P. Wang, Y. Wang, C. C. Jiao, K. Sun, L. Hu, A double-layered liquid metal-based electrochemical sensing system on fabric as a wearable detector for glucose in sweat. *Microsystems & Nanoengineering* **8**, (2022).

142. R. Z. Lin, J. S. Ho, A DIY approach to wearable sensor networks. *Nature Electronics* **4**, 771-772 (2021).

143. L. Yin, K. N. Kim, J. Lv, F. Tehrani, M. Y. Lin, Z. Z. Lin, J. M. Moon, J. Ma, J. L. Yu, S. Xu, J. Wang, A self-sustainable wearable multi-modular E-textile bioenergy microgrid system. *Nature Communications* **12**, (2021).

144. J. Stanley, J. A. Hunt, P. Kunovski, Y. Wei, A review of connectors and joining technologies for electronic textiles. *Engineering Reports* **4**, e12491 (2022).

145. Y. Xiao, Q. Li, C. K. Zhang, W. Zhang, W. B. Yun, L. P. Yang, Fabrication of silver electrical circuits on textile substrates by reactive inkjet printing. *IEEE Sensors Journal* **22**, 11056-11064 (2022).

146. M. S. Sadi, E. Kumpikaite, Advances in the robustness of wearable electronic textiles: strategies, stability, washability and perspective. *Nanomaterials* **12**, 2039 (2022).

147. P. Li, Y. K. Zhang, Z. J. Zheng, Polymer-Assisted Metal Deposition (PAMD) for Flexible and Wearable Electronics: Principle, Materials, Printing, and Devices. *Advanced Materials* **31**, (2019).

148. P. Li, Y. K. Zhang, Z. J. Zheng, Polymer-assisted metal deposition (PAMD) for flexible and wearable electronics: principle, materials, printing, and devices. *Adv. Mater.* **31**, 1902987 (2019).

149. D. H. Kim, J. A. Rogers, Stretchable electronics: materials strategies and devices. *Adv. Mater.* **20**, 4887-4892 (2008).

150. S. Q. Liang, Y. Y. Li, T. J. Zhou, J. B. Yang, X. H. Zhou, T. P. Zhu, J. Q. Huang, J. L. Zhu, D. Y. Zhu, Y. Z. Liu, C. X. He, J. M. Zhang, X. C. Zhou, Microfluidic Patterning of Metal Structures for Flexible Conductors by In Situ Polymer-Assisted Electroless Deposition. *Advanced Science* **4**, (2017).

151. A. Garcia, N. Hanifi, B. Jousselme, P. Jegou, S. Palacin, P. Viel, T. Berthelot, Polymer Grafting by Inkjet Printing: A Direct Chemical Writing Toolset. *Advanced Functional Materials* **23**, 3668-3674 (2013).

152. R. S. Guo, Y. Yu, Z. Xie, X. Q. Liu, X. C. Zhou, Y. F. Gao, Z. L. Liu, F. Zhou, Y. Yang, Z. J. Zheng, Matrix-Assisted Catalytic Printing for the Fabrication of Multiscale, Flexible, Foldable, and Stretchable Metal Conductors. *Advanced Materials* **25**, 3343-3350 (2013).

153. C. Y. Huang, W. T. Hsiao, K. C. Huang, K. S. Chang, H. Y. Chou, C. P. Chou, Fabrication of a double-sided micro-lens array by a glass molding technique. *Journal of Micromechanics and Microengineering* **21**, (2011).

154. E. del Barrio, C. Sanchez-Somolinos, Light to Shape the Future: From Photolithography to 4D Printing. *Advanced Optical Materials* **7**, (2019).

155. H. Hu, X. Y. Guo, Y. K. Zhang, Z. J. Chen, L. Wang, Y. Gao, Z. R. Wang, Y. Q. Zhang, W. S. Wang, M. M. Rong, G. Q. Liu, Q. Y. Huang, Y. Zhu, Z. J. Zheng, Elasto-plastic design of ultrathin interlayer for enhancing strain tolerance of flexible electronics. *Acs Nano* **17**, 3921–3930 (2023).

156. Y. Yang, Q. Y. Huang, L. Y. Niu, D. R. Wang, C. Yan, Y. Y. She, Z. J. Zheng, Waterproof, Ultrahigh Areal-Capacitance, Wearable Supercapacitor Fabrics. *Advanced Materials* **29**, (2017).

157. F. Chen, Q. N. Zhuang, Y. C. Ding, C. Zhang, X. Song, Z. J. Chen, Y. K. Zhang, Q. J. Mei, X. Zhao, Q. Y. Huang, Z. J. Zheng, Wet-Adaptive Electronic Skin. *Advanced Materials* **35**, (2023).

158. M. T. Chorsi, T. T. Le, F. Lin, T. Vinikoor, R. Das, J. F. Stevens, C. Mundrane, J. Park, K. T. M. Tran, Y. Liu, J. Pfund, R. Thompson, W. He, M. Jain, M. D. Morales-Acosta, O. R. Bilal, K. Kazerounian, H. Ilies, T. D. Nguyen, Highly piezoelectric, biodegradable, and flexible amino acid nanofibers for medical applications. *Science Advances* **9**, (2023).

159. S. M. Niu, N. Matsuhisa, L. Beker, J. X. Li, S. H. Wang, J. C. Wang, Y. W. Jiang, X. Z. Yan, Y. J. Yun, W. Burnetts, A. S. Y. Poon, J. B. H. Tok, X. D. Chen, Z. N. Bao, A wireless body area sensor network based on stretchable passive tags. *Nature Electronics* **2**, 361-368 (2019).

160. Y. D. Xu, G. G. Zhao, L. Zhu, Q. H. Fei, Z. Zhang, Z. Y. Chen, F. F. An, Y. Y. Chen, Y. Ling, P. J. Guo, S. H. Ding, G. L. Huang, P. Y. Chen, Q. Cao, Z. Yan, Pencil-paper on-skin electronics. *Proceedings Of The National Academy Of Sciences Of The United States Of America* **117**, 18292-18301 (2020).

161. Z. H. Zhou, K. Chen, X. S. Li, S. L. Zhang, Y. F. Wu, Y. H. Zhou, K. Y. Meng, C. C. Sun, Q. He, W. J. Fan, E. D. Fan, Z. W. Lin, X. L. Tan, W. L. Deng, J. Yang, J. Chen, Sign-to-speech translation using machine-learning-assisted stretchable sensor arrays. *Nature Electronics* **3**, 571-578 (2020).

162. H. Jin, N. Matsuhisa, S. Lee, M. Abbas, T. Yokota, T. Someya, Enhancing the Performance of Stretchable Conductors for E-Textiles by Controlled Ink Permeation. *Advanced Materials* **29**, (2017).

163. D. Kim, Z. Y. Yang, J. W. Cho, D. Park, D. H. Kim, J. K. Lee, S. Ryu, S. W. Kim, M. Kim, High-performance piezoelectric yarns for artificial intelligence-enabled wearable sensing and classification. *Ecomat* **5**, (2023).

164. I. J. Kim, M. K. Kim, J. S. Lee, Highly-scaled and fully-integrated 3-dimensional ferroelectric transistor array for hardware implementation of neural networks. *Nature Communications* **13**, (2023).

165. Y. R. Yang, Y. Song, X. J. Bo, J. H. Min, O. S. Pak, L. L. Zhu, M. Q. Wang, J. B. Tu, A. Kogan, H. X. Zhang, T. K. Hsiai, Z. P. Li, W. Gao, A laser-engraved wearable sensor for sensitive detection of uric acid and tyrosine in sweat. *Nature Biotechnology* **38**, 217-+ (2020).

166. J. Kim, A. S. Campbell, B. E. F. de Avila, J. Wang, Wearable biosensors for healthcare monitoring. *Nature Biotechnology* **37**, 389-406 (2019).

167. T. Carey, S. Cacovich, G. Divitini, J. S. Ren, A. Mansouri, J. M. Kim, C. X. Wang, C. Ducati, R. Sordan, F. Torrisi, Fully inkjet-printed two-dimensional material field-effect heterojunctions for wearable and textile electronics. *Nature Communications* **8**, (2017).

168. F. Chen, Q. Y. Huang, Z. J. Zheng, Permeable Conductors for Wearable and On-Skin Electronics. *Small Structures* **3**, (2022).

169. Q. Y. Huang, Z. J. Zheng, Pathway to Developing Permeable Electronics. *Acs Nano* **16**, 15537-15544 (2022).

170. Z. J. Ma, Q. Y. Huang, N. J. Zhou, Q. A. Zhuang, S. W. Ng, Z. J. Zheng, Stretchable and conductive fibers fabricated by a continuous method for wearable devices. *Cell Reports Physical Science* **4**, (2023).

171. Q. N. Zhuang, K. M. Yao, M. G. Wu, Z. G. Lei, F. Chen, J. Y. Li, Q. J. Mei, Y. Y. Zhou, Q. Y. Huang, X. Zhao, Y. Li, X. E. Yu, Z. J. Zheng, Wafer-patterned, permeable, and stretchable liquid metal microelectrodes for implantable bioelectronics with chronic biocompatibility. *Science Advances* **9**, (2023).

172. S. Liu, K. M. Ma, B. Yang, H. Li, X. M. Tao, Textile Electronics for VR/AR Applications. *Advanced Functional Materials* **31**, (2021).

173. Y. Y. Luo, Y. Z. Li, P. Sharma, W. Shou, K. Wu, M. Foshey, B. C. Li, T. Palacios, A. Torralba, W. Matusik, Learning human-environment interactions using conformal tactile textiles. *Nature Electronics* **4**, 193-+ (2021).

174. Z. J. Ma, Q. Y. Huang, Q. Xu, Q. N. Zhuang, X. Zhao, Y. H. Yang, H. Qiu, Z. L. Yang, C. Wang, Y. Chai, Z. J. Zheng, Permeable superelastic liquid-metal fibre mat enables biocompatible and monolithic stretchable electronics. *Nature Materials* **20**, 859-+ (2021).

175. V. Sanchez, C. J. Walsh, R. J. Wood, Textile Technology for Soft Robotic and Autonomous Garments. *Advanced Functional Materials* **31**, (2021).

176. X. Shi, Y. Zuo, P. Zhai, J. H. Shen, Y. Y. W. Yang, Z. Gao, M. Liao, J. X. Wu, J. W. Wang, X. J. Xu, Q. Tong, B. Zhang, B. J. Wang, X. M. Sun, L. H. Zhang, Q. B. Pei, D. Y. Jin, P. N. Chen,

H. S. Peng, Large-area display textiles integrated with functional systems. *Nature* **591**, 240-+ (2021).

177. V. Gaubert, X. Boddaert, T. Djenizian, R. Delattre, Textile Electronic Circuits from Laser-Patterned Conductive Fabric. *Advanced Engineering Materials* **25**, (2023).

178. R. A. Shveda, A. Rajappan, T. F. Yap, Z. Liu, M. D. Bell, B. Jumet, V. Sanchez, D. J. Preston, A wearable textile-based pneumatic energy harvesting system for assistive robotics. *Science Advances* **8**, (2022).

179. X. Tian, P. M. Lee, Y. J. Tan, T. L. Y. Wu, H. C. Yao, M. Y. Zhang, Z. P. Li, K. A. Ng, B. C. K. Tee, J. S. Ho, Wireless body sensor networks based on metamaterial textiles. *Nature Electronics* **2**, 243-+ (2019).

180. W. Weng, P. N. Chen, S. S. He, X. M. Sun, H. S. Peng, Smart Electronic Textiles. *Angewandte Chemie-International Edition* **55**, 6140-6169 (2016).

181. W. Yan, G. Noel, G. Loke, E. Meiklejohn, T. Khudiyev, J. Marion, G. C. Rui, J. N. Lin, J. Cherston, A. Sahasrabudhe, J. Wilbert, I. Wicaksono, R. W. Hoyt, A. Missakian, L. Zhu, C. Ma, J. Joannopoulos, Y. Fink, Single fibre enables acoustic fabrics via nanometre-scale vibrations. *Nature* **603**, 616-+ (2022).

182. W. F. Yang, W. Gong, C. Y. Hou, Y. Su, Y. B. Guo, W. Zhang, Y. G. Li, Q. H. Zhang, H. Z. Wang, All-fiber tribo-ferroelectric synergistic electronics with high thermal-moisture stability and comfortability. *Nature Communications* **10**, (2019).

183. Y. X. Yang, X. F. Wei, N. N. Zhang, J. J. Zheng, X. Chen, Q. Wen, X. X. Luo, C. Y. Lee, X. H. Liu, X. C. Zhang, J. Chen, C. Y. Tao, W. Zhang, X. Fan, A non-printed integrated-circuit textile for wireless theranostics. *Nature Communications* **12**, (2021).

184. K. Dong, Y. C. Wang, J. N. Deng, Y. J. Dai, S. L. Zhang, H. Y. Zou, B. H. Gu, B. Z. Sun, Z. L. Wang, A Highly Stretchable and Washable All-Yarn-Based Self-Charging Knitting Power Textile Composed of Fiber Triboelectric Nanogenerators and Supercapacitors. *Acs Nano* **11**, 9490-9499 (2017).

185. K. Jost, D. P. Durkin, L. M. Haverhals, E. K. Brown, M. Langenstein, H. C. De Long, P. C. Trulove, Y. Gogotsi, G. Dion, Natural Fiber Welded Electrode Yarns for Knittable Textile Supercapacitors. *Advanced Energy Materials* **5**, (2015).

186. A. Kiourti, C. Lee, J. L. Volakis, Fabrication of Textile Antennas and Circuits With 0.1 mm Precision. *Ieee Antennas And Wireless Propagation Letters* **15**, 151-153 (2016).

187. L. W. Taylor, S. M. Williams, J. S. Yan, O. S. Dewey, F. Vitale, M. Pasquali, Washable, Sewable, All-Carbon Electrodes and Signal Wires for Electronic Clothing. *Nano Letters* **21**, 7093-7099 (2021).

188. J. F. Wen, B. G. Xu, J. Y. Zhou, Toward Flexible and Wearable Embroidered Supercapacitors from Cobalt Phosphides-Decorated Conductive Fibers. *Nano-Micro Letters* **11**, (2019).

189. J. D. Ryan, D. A. Mengistie, R. Gabrielsson, A. Lund, C. Müller, Machine-Washable PEDOT:PSS Dyed Silk Yarns for Electronic Textiles. *Acs Applied Materials & Interfaces* **9**, 9045-9050 (2017).

190. R. Sliz, O. H. Huttunen, E. Jansson, J. Kemppainen, J. Schroderus, M. Kurkinen, T. Fabritius, Reliability of R2R-printed, flexible electrodes for e-clothing applications. *Npj Flexible Electronics* **4**, (2020).

191. M. C. Zhang, M. Y. Zhao, M. Q. Jian, C. Y. Wang, A. F. Yu, Z. Yin, X. P. Liang, H. M. Wang, K. L. Xia, X. Liang, J. Y. Zhai, Y. Y. Zhang, Printable Smart Pattern for Multifunctional Energy-Management E-Textile. *Matter* **1**, 168-179 (2019).

192. I. Kim, H. Shahariar, W. F. Ingram, Y. Zhou, J. S. Jur, Inkjet Process for Conductive Patterning on Textiles: Maintaining Inherent Stretchability and Breathability in Knit Structures. *Advanced Functional Materials* **29**, (2019).

193. J. Ko, Z. J. Zhao, S. H. Hwang, H. J. Kang, J. Ahn, S. Jeon, M. Bok, Y. Jeong, K. Kang, I. Cho, J. H. Jeong, I. Park, Nanotransfer Printing on Textile Substrate with Water-Soluble Polymer Nanotemplate. *Acs Nano* **14**, 2191-2201 (2020).

194. C. S. Luo, B. Tian, Q. Liu, Y. Feng, W. Wu, One-Step-Printed, Highly Sensitive, Textile-Based, Tunable Performance Strain Sensors for Human Motion Detection. *Advanced Materials Technologies* **5**, (2020).

195. H. Shahariar, I. Kim, H. Soewardiman, J. S. Jur, Inkjet Printing of Reactive Silver Ink on Textiles. *Acs Applied Materials & Interfaces* **11**, 6208-6216 (2019).

196. M. Takakuwa, K. Fukuda, T. Yokota, D. Inoue, D. Hashizume, S. Umezu, T. Someya, Direct gold bonding for flexible integrated electronics. *Science Advances* **7**, eabl6228 (2021).

197. F. C. Walsh, Electrode-reactions in metal-finishing. *Transactions of the Institute of Metal Finishing* **69**, 107-110 (1991).

198. D. P. Langley, M. Lagrange, G. Giusti, C. Jiménez, Y. Bréchet, N. D. Nguyen, D. Bellet, Metallic nanowire networks: effects of thermal annealing on electrical resistance. *Nanoscale* **6**, 13535-13543 (2014).

199. Z. Yin, M. Q. Jian, C. Y. Wang, K. L. Xia, Z. H. Liu, Q. Wang, M. C. Zhang, H. M. Wang, X. P. Liang, X. Liang, Y. W. Long, X. H. Yu, Y. Y. Zhang, Splash-Resistant and Light-Weight Silk-Sheathed Wires for Textile Electronics. *Nano Letters* **18**, 7085-7091 (2018).

200. M. A. Yokus, R. Foote, J. S. Jur, Printed Stretchable Interconnects for Smart Garments: Design, Fabrication, and Characterization. *Ieee Sensors Journal* **16**, 7967-7976 (2016).

201. K. A. Wills, K. Krzyzak, J. Bush, R. Ashayer-Soltani, J. E. Graves, C. Hunt, A. J. Cobley, Additive process for patterned metallized conductive tracks on cotton with applications in smart textiles. *Journal Of The Textile Institute* **109**, 268-277 (2018).

202. J. Suikkola, T. Björninen, M. Mosallaei, T. Kankkunen, P. Iso-Ketola, L. Ukkonen, J. Vanhala, M. Mäntysalo, Screen-Printing Fabrication and Characterization of Stretchable Electronics. *Scientific Reports* **6**, (2016).

203. S. S. Yao, J. Yang, F. R. Poblete, X. G. Hu, Y. Zhu, Multifunctional Electronic Textiles Using Silver Nanowire Composites. *Acs Applied Materials & Interfaces* **11**, 31028-31037 (2019).

204. J. R. Sempionatto, J. A. Lasalde-Ramirez, K. Mahato, J. Wang, W. Gao, Wearable chemical sensors for biomarker discovery in the omics era. *Nature Reviews Chemistry* **6**, 899-915 (2022).

205. L. B. Baker, A. S. Wolfe, Physiological mechanisms determining eccrine sweat composition. *European Journal of Applied Physiology* **120**, 719-752 (2020).

206. L. Klous, C. J. de Ruiter, S. Scherrer, N. Gerrett, H. A. M. Daanen, The (in)dependency of blood and sweat sodium, chloride, potassium, ammonia, lactate and glucose concentrations during submaximal exercise. *European Journal of Applied Physiology* **121**, 803-816 (2021).

207. M. I. Lindinger, S. P. Cairns, Regulation of muscle potassium: exercise performance, fatigue and health implications. *European Journal of Applied Physiology* **121**, 721-748 (2021).

208. X. C. He, S. J. Yang, Q. B. Pei, Y. C. Song, C. H. Liu, T. L. Xu, X. J. Zhang, Integrated smart janus textile bands for self-pumping sweat sampling and analysis. *Acs Sensors* **5**, 1548-1554 (2020).

209. Z. Sonner, E. Wilder, J. Heikenfeld, G. Kasting, F. Beyette, D. Swaile, F. Sherman, J. Joyce, J. Hagen, N. Kelley-Loughnane, R. Naik, The microfluidics of the eccrine sweat gland, including biomarker partitioning, transport, and biosensing implications. *Biomicrofluidics* **9**, 031301 (2015).

210. S. D. Wang, M. Li, J. Wu, D. H. Kim, N. S. Lu, Y. W. Su, Z. Kang, Y. G. Huang, J. A. Rogers, Mechanics of epidermal electronics. *Journal of Applied Mechanics-Transactions of the Asme* **79**, 031022 (2012).

211. J. Choi, D. Kang, S. Han, S. B. Kim, J. A. Rogers, Thin, soft, skin-mounted microfluidic networks with capillary bursting valves for chrono-sampling of sweat. *Advanced Healthcare Materials* **6**, 1601355 (2017).

212. Y. Shi, Z. Zhang, Q. Huang, Y. Lin, Z. Zheng, Wearable sweat biosensors on textiles for health monitoring. *Journal of Semiconductors* **44**, 021601 (2023).

213. M. A. Yokus, T. Agcayazi, M. Traenkle, A. Bozkurt, M. A. Daniele, Ieee, paper presented at the 2020 Ieee Sensors, 2020.

214. J. B. Hu, A. Stein, P. Buhlmann, Rational design of all-solid-state ion-selective electrodes and reference electrodes. *Trac-Trends in Analytical Chemistry* **76**, 102-114 (2016).

215. M. Pandiaraj, A. R. Benjamin, T. Madasamy, K. Vairamani, A. Arya, N. K. Sethy, K. Bhargava, C. Karunakaran, A cost-effective volume miniaturized and microcontroller based cytochrome c assay. *Sensors And Actuators A-Physical* **220**, 290-297 (2014).

216. Y. Shi, H. F. Dou, A. H. Zhou, Y. Q. Chen, Design and fabrication of a miniaturized electrochemical instrument and its preliminary evaluation. *Sensors And Actuators B-Chemical* **131**, 516-524 (2008).

217. J. B. Tu, J. H. Min, Y. Song, C. H. Xu, J. H. Li, J. Moore, J. Hanson, E. Hu, T. Parimon, T. Y. Wang, E. Davoodi, T. F. Chou, P. Chen, J. J. Hsu, H. B. Rossiter, W. Gao, A wireless patch for the monitoring of C-reactive protein in sweat. *Nature Biomedical Engineering* **7**, 1293-1306 (2023).

218. C. Ye, M. Q. Wang, J. H. Min, R. Y. Tay, H. Lukas, J. R. Sempionatto, J. H. Li, C. H. Xu, W. Gao, A wearable aptamer nanobiosensor for non-invasive female hormone monitoring. *Nature Nanotechnology* **19**, (2024).

219. Q. Pang, D. Lou, S. J. Li, G. M. Wang, B. B. Qiao, S. R. Dong, L. Ma, C. Y. Gao, Z. H. Wu, Smart Flexible Electronics-Integrated Wound Dressing for Real-Time Monitoring and On-Demand Treatment of Infected Wounds. *Advanced Science* **7**, (2020).

220. L. S. Sun, Z. W. Wang, H. F. Kang, P. Y. Luo, J. W. Su, W. Y. Wei, P. Q. Zhou, A. X. Yu, H. L. Dai, A flexibility self-powered Band-Aid for diabetes wound healing and skin bioelectronics. *Chemical Engineering Journal* **481**, (2024).

221. L. L. Tian, T. S. Liu, Y. X. Jiang, B. Y. He, H. Hao, Multifunctional hydrogel sensor with Tough, self-healing capabilities and highly sensitive for motion monitoring and wound healing. *Chemical Engineering Journal* **497**, (2024).

222. J. Wang, Z. Y. Liu, Y. Zhou, S. L. Zhu, C. Gao, X. Z. Yan, K. Wei, Q. Gao, C. B. Ding, T. T. Luo, R. H. Yang, A multifunctional sensor for real-time monitoring and pro-healing of frostbite wounds. *Acta Biomaterialia* **172**, 330-342 (2023).

223. Z. L. Ye, M. Y. Yang, M. Farhat, M. M. C. Cheng, P. Y. Chen, Multimodal wireless wound sensors via higher-order parity-time symmetry. *IEEE Sensors Journal* **24**, 741-749 (2024).

224. M. X. Yu, C. Yi, S. H. Lin, H. T. Ye, J. C. Xue, J. L. Yin, R. F. Zhong, H. Y. Yao, H. B. Liao, Y. Z. Zhang, J. Yang, Y. X. Guo, X. J. Song, T. T. Ye, E-bandage: exploiting smartphone as a therapeutic device for cutaneous wound treatment. *Advanced Intelligent Systems* **6**, (2024).

225. Y. H. Zhang, Y. B. Hu, Y. Montelongo, M. T. Hsu, J. Blyth, N. Jiang, A. K. Yetisen, A Conformable Holographic Sensing Bandage for Wound Monitoring. *Advanced Functional Materials* **34**, (2024).

226. N. T. Garland, J. W. Song, T. F. Ma, Y. J. Kim, A. Vázquez-Guardado, A. B. Hashkavayi, S. K. Ganeshan, N. Sharma, H. Ryu, M. K. Lee, B. Sumpio, M. A. Jakus, V. Forsberg, R. Kaveti, S. K. Sia, A. Veves, J. A. Rogers, G. A. Ameer, A. J. Bandodkar, A miniaturized, battery-free, wireless wound monitor that predicts wound closure rate early. *Advanced Healthcare Materials* **12**, (2023).

227. J. Henricson, J. Sandh, F. Iredahl, Moisture sensor for exudative wounds - A pilot study. *Skin Research And Technology* **27**, 918-924 (2021).

228. X. Huang, S. N. Cheng, F. Gong, X. Y. Yang, Z. F. Pei, X. L. Cui, G. H. Hou, N. L. Yang, Z. H. Han, Y. D. Chen, Y. Cheng, L. Cheng, A closed-loop patch based on bioinspired infection sensor for wound management. *Nano Today* **57**, (2024).

229. M. Jose, A. Bronckaers, R. S. N. Kumar, D. Reenaers, T. Vandenryt, R. Thoelen, W. Deferme, Stretchable printed device for the simultaneous sensing of temperature and strain validated in a mouse wound healing model. *Scientific Reports* **12**, (2022).

230. J. Y. Li, X. C. Huang, Y. W. Yang, J. K. Zhou, K. M. Yao, J. Li, Y. Y. Zhou, M. X. Li, T. H. Wong, X. E. Yu, Wearable and battery-free wound dressing system for wireless and early sepsis diagnosis. *Bioengineering Translational Medicine* **8**, (2023).

231. Z. J. Liu, H. Song, G. M. Lin, W. C. Zhong, Y. Zhang, A. Q. Yang, Y. X. Liu, J. H. Duan, Y. J. Zhou, K. J. Jiao, D. H. Ding, Y. W. Feng, J. Yue, W. J. Zhao, X. D. Lin, Wireless intelligent patch for closed-loop in situ wound management. *Advanced Science* **11**, (2024).

232. B. Mirani, Z. Hadisi, E. Pagan, S. M. H. Dabiri, A. van Rijt, L. Almutairi, I. Noshadi, D. G. Armstrong, M. Akbari, Smart dual-sensor wound dressing for monitoring cutaneous wounds. *Advanced Healthcare Materials* **12**, (2023).

233. T. Noushin, N. I. Hossain, S. Tabassum, IoT-Enabled Integrated Smart Wound Sensor for Multiplexed Monitoring of Inflammatory Biomarkers at the Wound Site. *Frontiers In Nanotechnology* **4**, (2022).

234. A. Alanio, M. Gits-Muselli, N. Guigue, B. Denis, A. Bergeron, S. Touratier, S. Hamane, S. Bretagne, Prospective comparison of (1,3)-beta-D-glucan detection using colorimetric and turbidimetric assays for diagnosing invasive fungal disease. *Medical Mycology* **59**, 882-889 (2021).

235. S. Darvishi, S. Tavakoli, M. Kharaziha, H. H. Girault, C. F. Kaminski, I. Mela, Advances in the sensing and treatment of wound biofilms. *Angewandte Chemie-International Edition* **61**, (2022).

236. P. Dutta, Y. J. Lu, H. Y. Hsieh, T. Y. Lee, Y. T. Lee, C. M. Cheng, Y. J. Fan, Detection of Candida albicans Using a Manufactured Electrochemical Sensor. *Micromachines* **12**, (2021).

237. X. D. Guo, F. Wen, N. Zheng, M. Saive, M. L. Fauconnier, J. Q. Wang, Aptamer-Based Biosensor for Detection of Mycotoxins. *Frontiers In Chemistry* **8**, (2020).

238. Y. Hua, F. Hu, X. Ren, Y. L. Xiong, J. Hu, F. Su, X. L. Tang, Y. F. Wen, A novel aptamer-G-quadruplex/hemin self-assembling color system: rapid visual diagnosis of invasive fungal infections. *Annals of Clinical Microbiology and Antimicrobials* **22**, (2023).

239. C. M. D. Lacerda, I. M. Ferreira, S. R. dos Santos, A. L. B. de Barros, S. O. Fernandes, V. N. Cardoso, A. S. R. de Andrade, (1 → 3)-β-D-glucan aptamers labeled with technetium-99 m: Biodistribution and imaging in experimental models of bacterial and fungal infection. *Nuclear Medicine And Biology* **46**, 19-24 (2017).